Seismic wave attenuation in scattering media : insights from numerical simulations and estimates from seismic ambient noise

Malcon Humberto Celorio Murillo

THÈSE

Pour obtenir le grade de

DOCTEUR DE L'UNIVERSITÉ GRENOBLE ALPES

École doctorale : STEP - Sciences de la Terre de l'Environnement et des Planètes
Spécialité : Sciences de la Terre et de l'Environnement
Unité de recherche : Institut des Sciences de la Terre

Attenuation des ondes sismiques dans les milieux diffusifs: apports de la simulation numérique et estimations à partir du bruit sismique ambiant

Seismic wave attenuation in scattering media: insights from numerical simulations and estimates from seismic ambient noise

Présentée par :

Malcon CELORIO MURILLO

Direction de thèse :

Emmanuel CHALJUB PHYSICIEN, Université Grenoble Alpes	Directeur de thèse
Laurent STEHLY PHYSICIEN ADJOINT, Université Grenoble Alpes	Co-encadrant de thèse

Rapporteurs :

Germán Andrés Prieto Gómez
PROFESSEUR ASSOCIÉ, Universidad Nacional de Colombia
Luis Fabian Bonilla Hidalgo
DIRECTEUR DE RECHERCHE, Université Gustave Eiffel

Thèse soutenue publiquement le 19 janvier 2024, devant le jury composé de :

Emmanuel CHALJUB PHYSICIEN, Université Grenoble Alpes	Directeur de thèse
Laurent Stehly PHYSICIEN ADJOINT, Université Grenoble Alpes	Co-directeur de thèse
Germán Andrés Prieto Gómez PROFESSEUR ASSOCIÉ, Universidad Nacional de Colombia	Rapporteur
Luis Fabian Bonilla Hidalgo DIRECTEUR DE RECHERCHE, Université Gustave Eiffel	Rapporteur
Marie Calvet PHYSICIENNE, IRAP	Examinatrice
Céline Gélis INGENIEURE CHERCHEURE, IRSN	Examinatrice
Florent Brenguier PHYSICIEN, Université Grenoble Alpes	Examinateur
Cécile Cornou DIRECTRICE DE RECHERCHE, ISTerre, IRD	Présidente

Seismic wave attenuation in scattering media: insights from numerical simulations and estimates from seismic ambient noise

Abstract

Among the physical processes that control the characteristics of seismic waves, attenuation is probably the least understood and the most poorly estimated factor. Globally, seismic attenuation is controlled by two mechanisms: scattering, which is the energy redistribution due to small-scale heterogeneities; and absorption, which is the dissipation of energy due to the presence of fluids or internal friction. Estimating these properties is crucial for the appropriate prediction of the earthquake ground motions, as well as to characterize the small-scale structures of the earth. Despite its relevance has been widely recognized, the estimation of attenuation properties and their effects on the predicted ground motion remains, in some extent, unclear for interpretation. Here we present a comprehensive study on the attenuation of seismic waves in highly heterogeneous media, in which we make use of numerical simulations, theoretical models and real data from seismic ambient noise.

The first part of our work consists in the analysis of the SH wave propagation in 2D random media. By a set of comparisons between results from numerical simulations of the full-wavefield with those from theoretical models such as the mean field and the radiative transfer theories, we propose a verification procedure that aims to shed some light on the understanding of the scattering effects in the ground motion simulations. Additionally, we study the transition between different propagation regimes, from ballistic to diffusive behaviors by exploiting the energy envelopes of our synthetic full-waveforms. We focus on the distance dependence of the peak energy envelope, which is a key parameter for the seismic hazard assessment. Thus, by analyzing the decay with distance and the statistical fluctuations of the peak energy, we show a clear distinction on the roles of the scattering and the transport mean free paths.

The final goal of this work is to propose a technique to characterize separately absorption and scattering properties at a local scale. To this end, we use continuous data of seismic ambient noise over four years at the Piton de la Fournaise volcano for frequencies between 0.5 and 4 Hz. Our technique consists in profiting the advantages that different ranges of propagation distances can exhibit. In this way, attenuation measurements are performed in two stages: (i) we first constrain absorption by using short propagation distances as the corresponding energy envelopes show coda durations long enough to measure a robust decay with time; and secondly (ii) scattering attenuation is measured from long propagation distances since the effects of small-scale inhomogeneities become more pronounced and easily distinguished when distance increases. The proposed technique (referred as ball-diff ratio) evidence a reduction of the effect of noise sources directivity on scattering attenuation measurements. Finally, our results are successfully validated by comparisons with estimates from earthquake data.

Résumé

Parmi les processus physiques qui contrôlent les caractéristiques des ondes sismiques, l'atténuation est probablement le facteur le moins compris et le plus mal estimé. Globalement, l'atténuation sismique est contrôlée par deux mécanismes: la diffusion, qui est la redistribution d'énergie due aux hétérogénéités à petite échelle; et l'absorption, qui est la dissipation d'énergie due à la présence de fluides ou à la friction interne. Estimer ces propriétés est crucial pour la prédiction appropriée des mouvements sismiques du sol lors d'un tremblement de terre, ainsi que pour caractériser les structures à petite échelle de la Terre. Malgré la grose reconnaissance de sa pertinence, l'estimation des propriétés d'atténuation et de leurs effets sur la prédiction des mouvements du sol demeure, dans une certaine mesure, sujette à des interprétations incertaines. Nous présentons une étude complète sur l'atténuation des ondes sismiques dans des milieux hautement hétérogènes, dans laquelle nous utilisons des simulations numériques, des modèles théoriques et des données réelles provenant du bruit sismique ambiant.

La première partie de notre travail consiste en l'analyse de la propagation des ondes SH dans des milieux aléatoires 2D. À l'aide d'un ensemble de comparaisons entre résultats de simulations numériques du champ d'ondes complet et ceux de modèles théoriques tels que le champ moyen et le transport radiatif, nous proposons une procédure de vérification qui vise à éclairer la compréhension des effets de diffusion dans les simulations des mouvements du sol. De plus, nous étudions la transition entre différents régimes de propagation, passant des comportements balistiques aux comportements diffusifs à partir de l'exploitation des enveloppes d'énergie des sismogrammes synthétiques. Nous nous concentrons sur la dépendance avec la distance du pic d'énergie des enveloppes, qui est un paramètre clé pour l'évaluation du risque sismique. Ainsi, en analysant la décroissance avec la distance et les fluctuations statistiques du pic l'énergie, nous mettons en évidence une distinction claire entre les rôles des libre parcours moyens scattering et transport.

Le but final de ce travail est de proposer une technique permettant de caractériser séparément les propriétés d'absorption et de diffusion des ondes sismiques à l'échelle locale. À cette fin, nous utilisons des données continues de bruit sismique ambiant sur une période de quatre ans au volcan Piton de la Fournaise, pour des fréquences comprises entre 0,5 et 4 Hz. Notre technique consiste à profiter des avantages que différentes gammes de distances de propagation peuvent offrir. De cette manière, les mesures d'atténuation sont effectuées en deux étapes : (i) nous caractérisons d'abord l'absorption en utilisant de courtes distances de propagation, car les enveloppes d'énergie correspondantes présentent des durées de coda suffisamment longues pour mesurer une décroissance robuste dans le temps; et après (ii) l'atténuation due à la diffusion est mesurée à partir de distances de propagation longues, car les effets des inhomogénéités à petite échelle deviennent plus prononcés et facilement distinguables lorsque la distance augmente.

Acknowledgments

Aux ancêtres, au peuple noir qui résiste et ré-existe,
Aux victimes du conflit en Colombie, et en général,
À tous *Les Damnés de la Terre.*

The work presented in this document is, in some way, the result of a long journey, starting from my bachelor days in Colombia to my last weeks as a PhD student in France. I want to thank every little interaction I had with many people which tremendously enriched my life as scientist but also as a human.

First of all, merci **Manu**! Merci de m'avoir donné l'opportunité de travailler sur un sujet aussi incroyable, d'être ouvert à construire cette idée de thèse ensemble selon nos intérêts communs. Merci pour ta motivation, ta grande flexibilité et générosité. Je garderai toujours en mémoire ce très bon souvenir de notre tout premier échange à Paris au début de 2019 pour choisir un sujet de thèse et pour explorer les possibilités de financement que nous avions à l'époque. Sur le plan financier, le chemin n'a pas été facile mais tu as fait de ton mieux pour que je puisse travailler dans des conditions dignes. Merci pour les longues discussions sur la propagation des ondes et sur les manières de faire une science "robuste" et transparente.

La façon de regarder la sismologie change radicalement quand on travaille avec le bruit de fond. Cette "nouvelle" sismologie, que je trouve comme l'une des choses les plus élégantes dans la physique des ondes, m'a beaucoup impressionné. Merci à **Laurent** de m'avoir introduit au monde du bruit sismique, mais surtout pour les interactions agréables et calmes. Merci pour ta patience et pour prendre le temps de discuter sur les détails les plus techniques. Tes mots, toujours justes, m'ont donné beaucoup d'espoir et de tranquillité aux moments où tout semblait être bloqué.

Je tiens aussi à remercier **Bérénice Froment** et **Ludovic Margerin** pour avoir fait partie de mon comité de thèse. Ces interactions nous ont énormément aidés à bien diriger nos travaux, et ont aussi donné lieu à de fortes collaborations. Merci beaucoup Ludovic pour toutes les bonnes explications sur la Théorie du Transport Radiatif et pour m'encourager d'aller toujours au fond sur le phénomène du 'scattering'.

Thanks to my jury members, **Cécile Cornou, Florent Brenguier, Céline Gelis** and **Marie Calvet** for their interest in our work. I also want to thank **Fábian Bonilla** and **Germán Prieto** who served as reviewers. [Gracias, particularmente a Fabián por guiarme durante mi pasantía en el **IPGP** y mostrarme por primera vez el mundo de la propagación de ondas en medios aleatorios. Aquellos cuatro meses de investigación fueron intensos, pero también de tremendo aprendizaje y de muy buenos intercambios].

I gratefully acknowledge the financial support provided by **Minciencias** through "la convocatoria 860 de doctorados en el exterior". Also want to thank Colfuturo for the funding in the first six months of my PhD. The complementary funding was provided by the Risk Geophysics

team (equipe **GRE**) of **ISTerre**, which I tremendously acknowledge.

I am also thankful to the **Ecos-Nord project** between **UGA** and **Universidad Nacional de Colombia (UNAL)** for the fruitful discussions and mobility. Thanks particularly to **Carlos Vargas, Germán Prieto, Manu Chaljub, Philippe Gueguen, Ana Maria Tobon and Andrés Hernandez**. Exchanging and bringing our ideas into the colombian context was always super motivating.

Science was the reason to come to Grenoble, but these colleagues became the main reason to come everyday to the lab. I want to mention some of them: **Lara, Leoncio, Anette, René, Ana Maria, Hugo, Hester, Laura, Dilruba, Gino, Camila, Giuseppe (il maestro), Veleda, Destin, Emmanuel Caballero, David** and **Andrés Hernandez**. Mi gente, I really appreciate all those interesting conversations, as well as those long nights of dancing. It seems that regular doses of Salsa, Bachata and Merengue became good medicines for many of us.

Mis sinceros y cálidos agradecimientos a mi mentor académico y amigo **Hugo Monsalve Jaramillo**. Gracias por creer en mí y abrirme las puertas de la investigación en sismología. El curso de sismología para voluntarios y el semillero sobre la mesa vibratoria despertaron en mí muchas motivaciones y preguntas que han moldeado esta temprana carrera como científico. Gracias siempre, don Hugo, por apostarle a todos los que tuvimos el deseo de hacer algo distinto. De igual forma, agradezco a **William Valencia** y **Mario Marmolejo** por indicarme el camino hacia la formación de más alta calidad.

Las primeras líneas de esta sección indicaban que el trabajo presentado en este documento es, de alguna forma, el resultado de un largo viaje: desde mis días como estudiante universitario en Colombia, hasta mis últimas semanas de doctorado en Francia. En el sentido más estricto del mensaje, tendría que decir que todo arranca en el 92, ¿y los responsables? **Joanne** y **Humberto** (Mamá y Papá). No me alcanzarían mil páginas para agradecerles por todo el amor y apoyo que siempre me han brindado. Gracias por transmitirme el amor a la vida, el respeto a las diferencias, el autorreconocimiento como persona negra, el autoestima y a creer en la educación como mecanismo importante para vivir con dignidad y lucidez. **Mamá** y **Papá**, mil gracias por motivarme a ir a un mundo mas allá del que que las posibilidades sugerían para nosotros. Agradezco también a mis otros pilares, y ejemplos de lucha, mis hermanos **Winnie** y **Kwamen**, mi mamá **Segunda** y mi abuela **Eufemia** (Q.E.P.D). Gracias a todos mis otros familiares, especialmente a las tias **Yudy**, **Cristina** y **Amanda**.

Gracias a **Stephany** por todo su apoyo y amor durante el tiempo compartido. Por siempre animarme en los momentos más difíciles y recordarme siempre lo valioso que fue todo este camino. Quiero finalmente mencionar a algunos mis amigos de toda la vida, quienes siempre estuvieron muy atentos y presentes durante esta particular etapa: **Laura Ante, Jeison, Gustavo** y **César**.

Contents

Chapter 1

General introduction

Understanding the physical processes controlling the characteristics of the ground motion is relevant to investigate the inner structure of the earth, but also to properly evaluate the seismic hazard. Seismic records exhibit some signatures that might often allow to study either the origin of the observed ground motion or the physical properties of the propagation media. Some of these signatures can directly be observed from the arrival time, the wave amplitudes, the duration and the frequency content of the seismic signal. For instance, interpreting the travel time of the recorded ground motions represents the basic principles of the classical seismic tomography. In this case, when the location of the source is known, it is possible to estimate the propagation velocity, which is an elastic parameter related to the material composition. Indeed, this kind of approach have helped to provide interesting insights on the large scale structures of the earth. However, the complexity of geological processes give origin to some short-scale heterogeneities that can not be resolved by classical tomography. The interaction of direct waves with these small-scale heterogeneities is known as scattering and it is partially the responsible of the amplitude decay of seismic waves. Another source of such decay is related to the energy absorption due to mechanisms of internal friction or fluid viscosity. Thus, estimating the attenuation of seismic waves can provide significant knowledge on the small-scale structures composing the earth.

From the perspective of seismic hazard, quantifying the attenuation of seismic waves is essential for the accurate prediction of the earthquake ground motions. On the one hand, absorption can control how fast the ground motion decays with time. On the other hand, scattering plays an important role in the duration, amplitude decay of the direct wave energy and the spatial variability of the ground motion. These effects become more significant at the high frequency ($f > 1$Hz), due to the stronger interaction between the short wavelengths and the small-scale inhomogeneities.

The different natures of these two attenuation mechanisms, as well as their distinctive signatures on the ground motion, make necessary to characterize absorption and scattering attenuation separately. For this task, several works have made use of the radiative transfer theory (RTT) (Wu (1985); Margerin et al. (1998)), which can simulate the spatio-temporal evolution of seismic energy in highly heterogeneous and absorbing media, and it neglects the phase information. This means that the exact location of the scatterers is not known but a random distribution of them is assumed. Despite such simplification, these type of approaches can globally simulate the attenuation of direct energy and the emergence of coda waves. The basic idea for the estimation procedure of absorption and scattering properties consists in fitting the simulated RTT energy envelopes to those from the observed seismic records. It is worth mentioning that robust estimations of attenuation properties require the identification of propagation regimes where each mechanism is more prompt to be dominant.

While at the crustal scale diverse techniques have been proposed to estimate attenuation properties separately (e.g. Fehler et al. (1992); Carcole and Sato (2010)), at the local level (e.g. sedimentary basins scale), which is the interest of engineering seismology, the estimations of seismic wave attenuation remain difficult to interpret. First, because seismic attenuation is often obtained as an apparent energy decay, in which the mechanisms participating are not distinguished. And secondly, because of the use of earthquake records, whose sensitivity might exceed the size of typical sedimentary basins. The lack of a systematic procedure to estimate absorption and scattering attenuation at a local scale increases considerably the mismatch between the observed and numerically simulated earthquake ground motions, and more particularly in terms of duration and spatial variability (see Fig. 1.1).

However, retrieving attenuation properties at the scale of a sedimentary basin is a challenging task first, because localized measurements would require the use of small and local earthquakes, which are very rare in a basin context. In this case, an interesting alternative would be the use of reconstructed ballistic and coda waves from cross-correlation functions of seismic noise. Furthermore, this potential approach would allow to map attenuation properties sensitive to the area of interest, for which the receiver couples can be located strategically. A second difficulty in the separation of attenuation properties concerns the identification of diverse propagation regimes at which one attenuation mechanism is expected to be more dominant than the other (see the MLTWA in chapters 2 and 5). This last point makes necessary to study comprehensively the seismic scattering phenomenon with the aid of observations and phenomenological models. Another possibility is the use of numerical simulations of the full-wavefield in highly heterogeneous media, which offer the capability to exploit a broad variety of random media and scattering regimes, as much as the computational resources allow it.

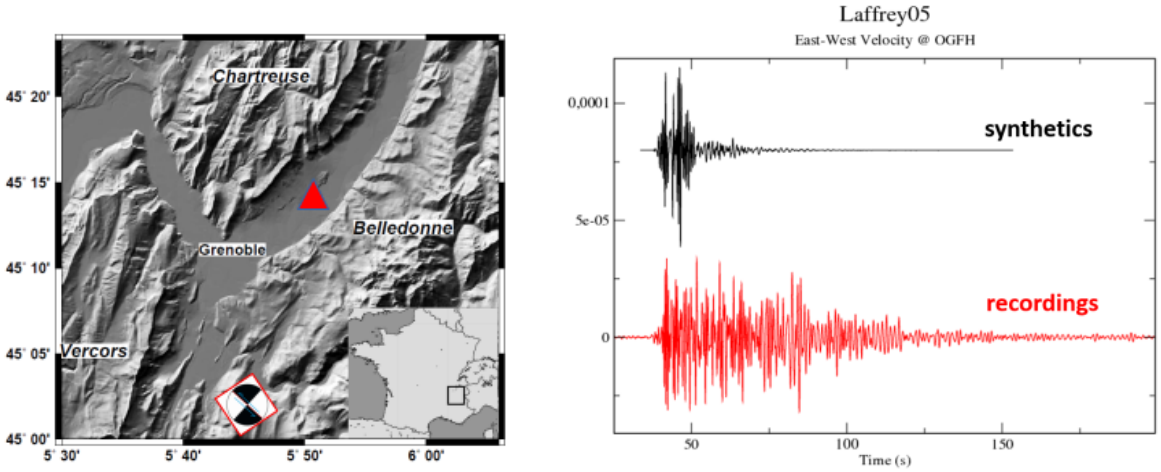

Figure 1.1: Example of ground motion simulation of the $M2.8$ Laffrey earthquake (2005) in the Grenoble valley (Left). And comparison between the observed (red) and simulated (black) ground motion. The lack of robust velocity and attenuation models makes difficult to reproduce the observed duration of the ground motion. Taken from Chaljub et al. (2021).

The objective of this PhD is to propose a methodology to quantify absorption and scattering properties separately at a local scale. To this end, we first perform a comprehensive study on the propagation of seismic waves in scattering media from numerical simulations of the full wavefield. The analyses of these synthetics provide some insights on the emergence of different scattering regimes and the physical parameters controlling it. In a second part of our work, we develop a technique to separate absorption and scattering attenuation from seismic ambient noise at a local

scale. As an application case, we perform our investigation at the area surrounding the Piton de la Fournaise volcano, whose length scale is comparable to that of a sedimentary basin (tens of kilometers). It is worth mentioning that the extremely high level of heterogeneities and the presence of fluids make convenient to develop our technique in such context.

The present document aims to summarize the results and analyses of a work carried out in the last four years. This document is organized in the following way: chapter 2 presents a review on the diverse approaches and techniques to constrain seismic attenuation at different length scales; In chapter 3 we present the results of numerical simulations of SH waves in 2D random media which aims to be a verification procedure when studying the effects of small-scale inhomogeneities in ground motion simulations. We focus on the attenuation and dispersion properties of the coherent wave; The same synthetic data set is then exploited in chapter 4 to study the transport of seismic energy in 2D scattering media. We pay particular attention on the space-time evolution of the peak intensity and the scattering quantities controlling its behavior. In chapter 5 we present a methodology to estimate, separately, absorption and scattering attenuation from seismic ambient noise at a local scale. As an application case, we chose the Piton de la Fournaise volcano. Finally, some conclusions and perspectives are presented in chapter 6.

The work presented in this dissertation has led to the following production:

- **Celorio, M.**, Stehly, L., and Chaljub, E. (2024). Separation of absorption and scattering attenuation from seismic ambient noise at the Piton de la Fournaise volcano (in preparation).

- **Celorio, M.**, Chaljub, E., Margerin, L., and Stehly, L. (2022). Propagation of 2-D SH waves in random media: Insights from ab-initio numerical simulations and transport theory. Frontiers in Earth Science, 10.

- Chaljub, E., **Celorio, M.**, Cornou, C., De Martin, F., El Haber, E., Margerin, L., Marti, J., and Zentner, I. (2021). Numerical simulation of wave propagation in heterogeneous and random media for site effects assessment in the grenoble valley. (Conference paper).

Chapter 2

State of the art: The seismic wave attenuation at different length-scales

2.1 Ground motion prediction and attenuation estimates

Earthquakes generate waves that propagate in multiple directions. The recorded motion at the surface is controlled by several physical processes such as the earthquake source, the path effects in the crust, the site amplification caused by the local geology, and the seismic wave attenuation. Fig. 2.1 illustrates globally the sequence from the earthquake source to the recorded ground motion.

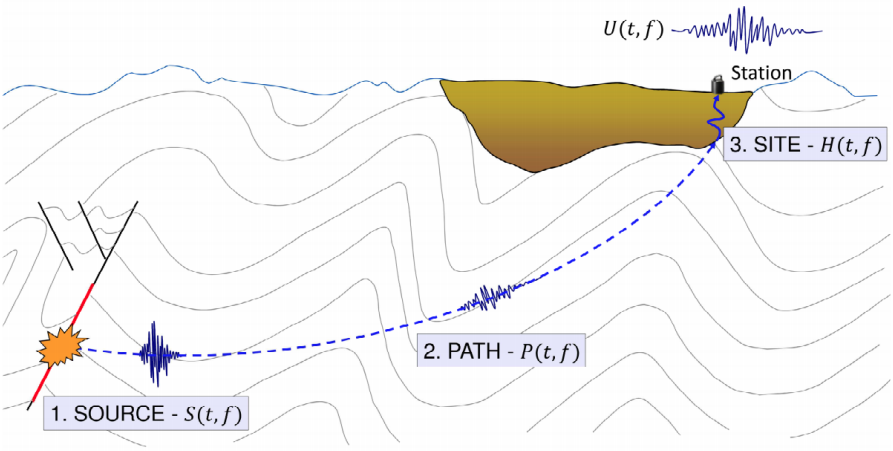

Figure 2.1: Illustration of the different terms in the earthquake ground motion: from the earthquake source to the site response. The grey lines represent the layers composing the propagation medium and the blue solid line indicates the free surface topography (Taken from Perron, 2017).

In the context of risk management, quantifying these effects is crucial for the evaluation of seismic hazard. Mathematically, the recorded motion U can be expressed as the convolution of the physical processes above mentioned.

$$u(t,f) = S(t,f) * P(t,f) * H(t,f) * I(t,f) \tag{2.1}$$

where S is the earthquake source, P represents the path effects, H corresponds to the site effects due to the local geology and I is the instrument response, which in order to appropriately

interpret the physical sequence must be removed. Depending on the propagation regimes, the contribution of these ingredients might have some signature on the recorded waveforms. On one hand, at short propagation distances, source signatures might clearly be distinguished. This would allow the appropriate characterization of the earthquake source in terms of its duration and focal mechanism. On the other hand, as travel distance increases, the interaction of primary waves with some geological structures in the path from the source to the site, might strongly shape the recorded ground motion and mask the source signatures. Additionally, the local geology can modify the incoming wavefield due to the strong impedance changes. This is known as site effects and one of the most representative examples is the strong shaking observed in the México valley for the Michoacan earthquake in 1985 (Anderson et al. (1986)). The most striking signature of local conditions is the amplification of seismic waves, as well as an increase of the duration due to the trapping effects inside sedimentary basins. These local amplifications have been studied by simulating the full-wavefield in sedimentary basins (Bard and Bouchon (1985); Chaljub et al. (2010); Cruz-Atienza et al. (2016)) or from real data processing (Cornou et al. (2003); Prieto and Beroza (2008); Denolle et al. (2014)). An active field of research on the site effects simulation concerns the nonlinear soil behavior when the input ground motion exceeds certain level of strain (Bonilla et al. (2005); Gélis and Bonilla (2012)). This type of behavior can severely complicate the interpretation of the recorded ground motion and might often require numerical and laboratory approaches to be addressed.

As an opposite effect to local amplification, seismic waves can experience an amplitude decay with time and distance. This apparent loss of energy is known as seismic attenuation and there are basically, two mechanisms contributing to it: (i) absorption, which is the dissipation of the energy due to the internal friction between the particles that compose the propagation medium or the presence of fluids; And (ii) scattering, which is the interaction of primary waves with small-scale inhomogeneities. Such interaction would generate a redistribution of the energy, in which a fraction of the direct energy is the multiply diffracted and converted into the so-known coda waves. Fig. 2.2(left) shows a scheme of intrinsic properties of the medium that can generate scattering and absorption attenuation: on one hand the random small-scale inhomogeneities due, either to the fluctuations elastic parameters or to the existence of small structures such as cracks; on the other hand the presence of fluids as mechanism to absorb energy.

The total attenuation is often expressed as $Q^{-1} = Q_i^{-1} + Q_{sc}^{-1}$, where Q is the so-known quality factor and it is defined as the ratio of stored and lost energies per oscillation cycle. Q_i and Q_{sc} represent the absorption and scattering attenuation mechanisms, respectively.

In the field of seismology, the separation of scattering and absorption mechanisms has been possible thanks to the use of phenomenological models such as the radiative transfer theory (RTT) (Wu (1985); Margerin et al. (1998)) and the diffusion approximation (Wegler and Lühr (2001); Dainty et al. (1974)). These two approaches rely on the energy transport in media with random inhomogeneities and neglect the phase information. An important key for the separation of attenuation mechanisms is the fact that they can produce different signatures on the shape of seismogram energy envelopes. On one hand scattering attenuation is the responsible of the decrease of direct energy with distance. On the other hand, the level of absorption can be appreciated from how fast amplitudes decay with time, regardless of the propagation distance. These signatures are illustrated in Fig.2.2(right). In section 2.2.2 we will show in more detail the physical meaning and applications of radiative transfer and diffusion models.

Whereas the seismic quality factor Q (Knopoff (1964)) is the parameter most widely used in the practice of seismology to characterize the intrinsic attenuation of seismic waves, in the contexts of engineering seismology and geotechnical earthquake engineering, parameters kappa (κ) (Anderson and Hough (1984)) and damping ratio (ξ) are more common. The κ parameter

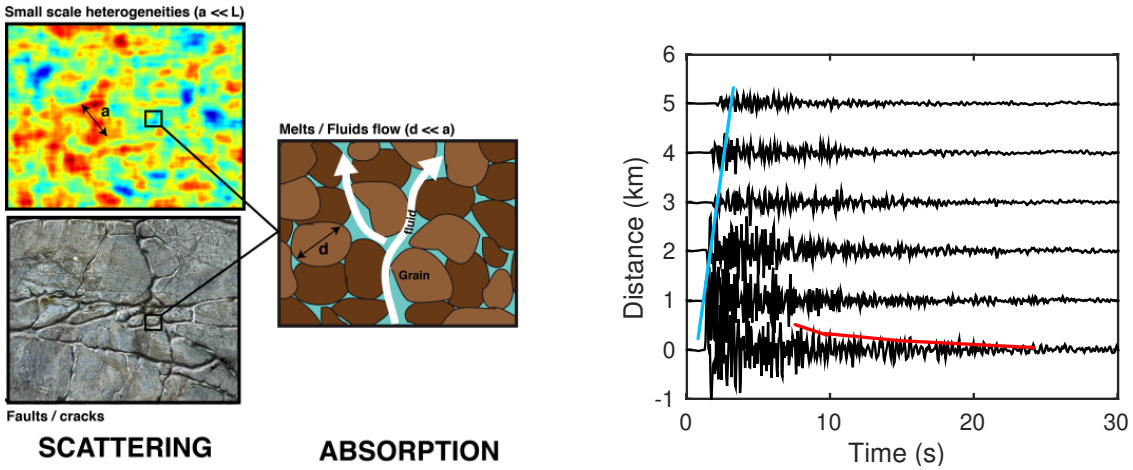

Figure 2.2: (left) Schematic view of the processes and spatial scales involved in seismic wave attenuation. Scattering is caused by small-scale elastic fluctuations or mechanical discontinuities. Absorption is caused by anelastic processes, such as viscous dissipation, fluid flow between fractures, or at the pore scale. Taken from Margerin et al. (2022); (right) Illustration of amplitude decay of direct waves with distance (blue line) due to scattering (besides geometrical spreading) and the amplitude decrease with time due to absorption (red line).

was first introduced by Anderson and Hough (1984) as a spectral decay factor to describe the attenuation at high frequency. These authors measured κ directly from the Fourier amplitude spectra of several records. They found that above a certain frequency, the amplitude follows an exponential decay of the form $e^{-\pi\kappa f}$. Furthermore, their results showed that κ is dependent on the site and distance, it increases gradually at long epicentral distances, but it becomes smaller at sites on rocks than at those on alluvial sediments. A further correction was implemented in order to eliminate the distance dependence of κ and the resultant κ_0 parameter was interpreted as a site property related to the 'anelastic' attenuation.

In further works, estimates of κ_0 have been extensively used for the prediction of ground motions, either using point-source or finite-fault stochastic simulations. In these cases κ_0 is used as low-pass filter to reproduce the effects of high frequencies on the peak ground motion or in the shape of amplitude spectra (Boore (1986); Boore (2003); Graves and Pitarka (2010)).

The physical interpretation of parameter κ have been addressed by diverse authors (Ktenidou et al. (2015); Parolai et al. (2015); Cabas et al. (2017)). For instance, Parolai et al. (2015) studied the role of 'intrinsic' and scattering attenuation on κ estimations. By using 1D numerical simulations from the propagator matrix approach, their results evidenced the joint contribution of both attenuation mechanisms on κ parameter. Furthermore, they showed that the measurements of κ, generally based on the direct pulses, might not be appropriate when forward scattering is strong because energy is redistributed at different spectral ordinates due to the effect of inhomogeneities. In such cases, the spectral decay parameter κ might be underestimated, specially if the 'intrinsic' attenuation is weak. A review on the different techniques to estimate κ can be found in Ktenidou et al. (2014).

The damping ratio ξ, which is so often used in the fields of geotechnical and structural engineering, is expressed as inversely proportional to the Q quality factor and it is assumed to be independent on frequency. ξ is generally measured from laboratory cyclic tests of stress-strain, which characterizes directly the energy dissipation. However, these tests can only capture the intrinsic material attenuation, excluding some other sources of the amplitude decay of seismic

waves, such as scattering or geometrical spreading. The disability of laboratory-based damping to include the other attenuation mechanisms often seen in the field has been shown in previous works (Elgamal et al. (2001); Yee et al. (2013); Zalachoris and Rathje (2015)). Cabas et al. (2017) compared field estimates of seismic attenuation at the site (given by κ_0) with those from laboratory tests of ξ. They proposed a damping model for a site, which takes into account the contribution of shallow layers to the total damping, being more consistent with κ_0 parameter.
In physics-based simulations of earthquake ground motions, the effect of attenuation is generally incorporated by using a visco-elastic model, due to its mathematical convenience. In most of these cases, absorption (expected to be given by the visco-elastic mechanism) is chosen to be independent on frequency and inversely proportional to the shear wave velocity. These common practices put in evidence the lack of a systematic constrain of intrinsic attenuation that can be used as an input for the ground motion simulations. Furthermore scattering attenuation is often neglected. To properly estimate the physics-based ground motion at high frequencies, scattering effects must be taken into account through the incorporation of small-scale inhomogeneities. In the next section we will show some concepts and existing works in literature about the propagation of seismic waves in highly heterogeneous media, whose inhomogeneities are so far considered as random. The ensemble of cases we show make use either of numerical simulations of the full-wave field or phenomenological models based on the transport of energy.

2.2 Wave propagation in random media

The complex structure of the earth is heterogeneous, and propagating elastic waves often face it. On the one hand, large scale structures influence the travel time of body waves and can efficiently be resolved by classical techniques of seismic tomography (Aki et al. (1976); Aki et al. (1977); Cerveny (1987); Fei et al. (1995)). On the other hand, small-scale inhomogeneities are so far considered as random and stochastic approaches are necessary to investigate them (e.g. mean field theory, RTT and diffusion approximation). When the size of these random inhomogeneities is comparable to the propagating wavelengths, perturbations on the wavefield become more important (Sato et al., 2012). This interaction is known as scattering and it is the responsible for energy redistribution and apparent attenuation. In this way, different representations of the wavefield, such as seismograms, Fourier spectra and energy envelopes, can exhibit several signatures that correspond to diverse propagation regimes. A first regime is known as ballistic, which is expected to contain the direct energy traveling from the source to the receiver; a second regime corresponds to the waves that have interacted once with the small scale inhomogeneities and it is known as single scattering; And finally, the third regime describes the waves that have interacted multiply with the small-scale inhomogeneities and it is known as multiple diffusion. The multiply diffused components of the full-wavefield is contained in the portion of a seismogram known as coda waves. In this section we present some basic models broadly used for the description of propagating waves in media with random heterogeneities.

A first description on the wave propagation in random media focuses on the mayor evidence of scattering, the coda waves. These type of waves were initially studied by Aki (1969) who defined them as the result of the interaction of primary waves with random inhomogeneities in the crust. In a later publication, Aki and Chouet (1975) proposed the use of two extreme models to describe the energy evolution of coda waves: single scattering and multiple diffusion. They demonstrated that at long lapse times t, the observed energy in the coda $E(t, f)$ decreases exponentially with

time as:

$$E(t,\omega) = S(\omega)\frac{1}{t^n}e^{-\omega t/Q_c(\omega)} \tag{2.2}$$

Where ω is the angular frequency, $S(\omega)$ is the source factor, Q_c is the coda quality factor, n is a parameter that depends on the type of wave (body or surface) and the propagation regime. For instance, at short lapse times, right after the ballistic regime, coda waves are composed mainly by waves that have been scattered just once. In this case n is chosen as 2. At long lapse times, coda waves enter in the regime of multiple diffusion, then n is chosen as 3/2. It is worth mentioning that depending on the propagation regime, Q_c might be affected by both, scattering and absorption parameters (Q_{sc} and Q_i). Thus, estimations of Q_c can be interpreted in diverse ways. From measurements of seismic attenuation in Japan, Carcole and Sato (2010) found good agreement between Q_c and Q_i from the diffusion model. Calvet and Margerin (2013) demonstrated that this agreement occur only if scattering is not too strongly anisotropic and at sufficiently long lapse times.

2.2.1 Description of a random medium

It is possible to investigate small-scale inhomogeneities either from the estimation of scattering properties observed on seismic records or from borehole petrophysical logs (Dolan et al. (1998)). From the seismological point of view, the physical properties that interest the most, as evidences of material heterogeneity, are the wave velocity and the density, which are the parameters characterizing the propagating media. In this way, the spatial variations of a given physical property of a medium with random heterogeneities can be expressed as the sum of the background property plus some random perturbations. For instance, in the case of the wave velocity, this can be written as:

$$v(\mathbf{x}) = v_0(1 + \xi(\mathbf{x})) \tag{2.3}$$

Where $v(\mathbf{x})$ is the space dependent wave velocity, v_0 is the background velocity and $\xi(\mathbf{x})$ is the function representing the random fluctuations around v_0. Heterogeneous media can be characterized by auto-correlation functions (ACF) of the velocity (or density) fluctuations ($R(\mathbf{x})$). Where the level of perturbation is defined by the mean square fluctuation ε^2 and the spatial variations (roughly related to the size of the scatterers) is controlled by the correlation distance a. Thus, ε and a are the key factors controlling the statistical properties of random media. The explanation about the properties of a random media will be extended in chapter 3.

Klimeš (2002) proposed some cases auto-correlation functions which are convenient for seismological applications. Some of these are the Gaussian, exponential and von Kármán ACF. The most manageable auto-correlation function is the Gaussian type, which is given by the following expression:

$$R(\mathbf{r}) = \varepsilon^2 e^{-r^2/a^2} \tag{2.4}$$

Where r is the lag distance, which for the 2D case is expressed as $r = \sqrt{x^2 + y^2}$. This type of ACF is poor in small-scale components. However, due to its mathematical tractability, a lot of theoretical work have been developed by using this type of ACF. To represent a medium richer small-scale components, the von Kármán type has been the most widely accepted ACF

in seismology. Equations 2.5 and 2.6 correspond to the exponential and von Kármán ACFs, respectively.

$$R(\mathbf{r}) = \varepsilon^2 e^{-r/a} \tag{2.5}$$

$$R(\mathbf{r}) = \frac{\varepsilon^2}{2^{H-1}\Gamma(H)} \left(\frac{r}{a}\right)^H K_H\left(\frac{r}{a}\right), \tag{2.6}$$

In chapter 3 it will be shown that the incorporation of these ACF is conveniently performed in the wavenumber domain. In this section, as a general explanation of the characteristics of random media we simply show it's representation on space domain. In Eq. 2.6, H is the Hurst exponent, $\Gamma(H)$ is the Gamma function and K_H is the modified Bessel Function of order H. It is worth mentioning that parameter H controls content of small-scale components in a von Kármán medium. Indeed, the exponential ACF is a special case of von Kármán type when $H = 0.5$. In Fig. 2.3(left) we illustrate the 2D representation of the previously mentioned ACFs. The correlation length a and the perturbation level ε are the same for the four cases of ACF: 5 km and 0.05, respectively. Note that, except for the Gaussian ACF, the plots shown in Fig. 2.3(left) represent von Kármán types with different Hurst exponents (the exponential type is a von Kármán medium with $H = 0.5$). It can be observed that the small-scale components increase as H decreases.

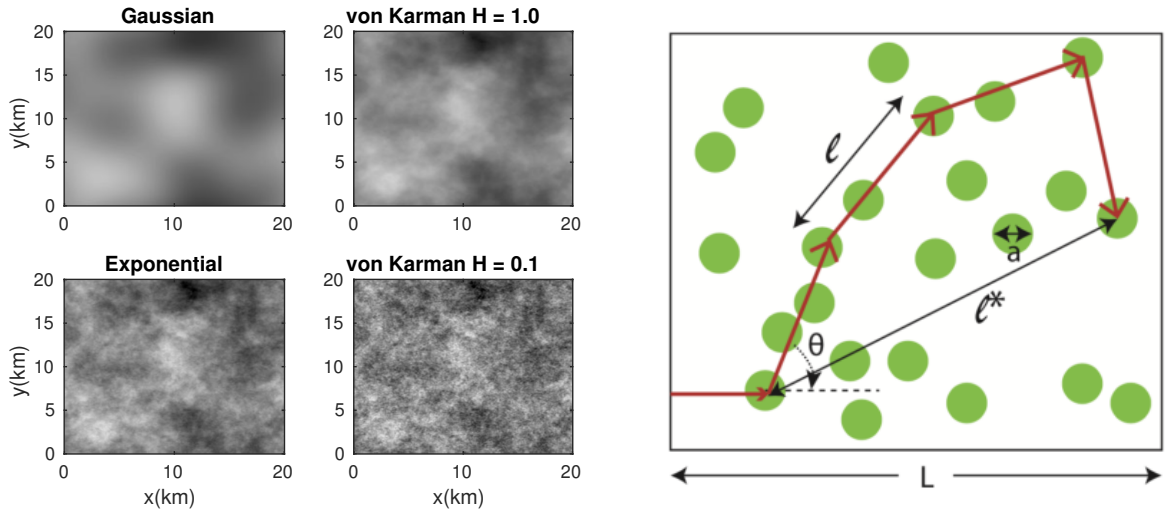

Figure 2.3: (Left) Examples of auto-correlation functions. Parameters a and ε are the same for all the cases: $a = 5$ km and $\varepsilon = 0.05$. (Right) Illustration of the length scales in a medium with random inhomogeneities. The scattering mean free path (ℓ), transport mean free path (ℓ^*) and the correlation length (a) or size of the scatterer. Taken from Sato et al. (2012).

As mentioned previously, our investigation on media with small-scale inhomogeneities is performed from a seismological perspective. In that case, most of the techniques to estimate the properties of the random media, such as RTT or diffusion approximation, do not allow to invert directly for the statistical parameters (a, ε or H), but they would rather allow to obtain scattering properties, which are given by the two length scales: the scattering mean free path ℓ and the transport mean free path ℓ^*. The scattering mean free path is defined as the average distance between two scattering events. This parameter also controls the attenuation of the

coherent wavefield, which is the wave that keeps the memory of the original propagation direction. From the theoretical point of view, the coherent wave can be retrieved as the ensemble average of the wavefield over several realizations of the random medium. The ergodicity hypothesis states that this ensemble average is equivalent to perform a spatial average of records whose stations have common distances to the source in one single realization. This last point is crucial for the estimation of the coherent wave attenuation (ℓ^{-1}) since, from the numerical point of view, just one single realization would be enough to retrieve the mean wavefield. This would considerably reduce the computational cost of the numerical simulations of seismic waves in random media. The second length scale ℓ^*, represents the typical distance after which the multiple diffusion regime emerges. This means, that at propagation distances longer than ℓ^*, the angular dependence of the energy density tends to be uniformized. Thus, the appropriate processing and inversion of the observed energy being transported in a medium with small-scale inhomogeneities would lead to the estimation of these two parameters. The role of ℓ and ℓ^* on the seismic scattering phenomenon will be discussed in chapters 3 and 4. Fig. 2.3(right) shows these two length scales in a medium with random inhomogeneities, where the difractors are represented by green circles. The use of realistic models (e.g. anisotropic scattering in RTT) would then allow to relate scattering length scales with statistical parameters a and ε (Gaebler et al. (2015)).

2.2.2 Radiative transfer theory

The recorded ground motion on a medium with random inhomogeneities can exhibit diverse scattering signatures such as the attenuation of direct waves, peak delay, peak broadening and the emergence of coda waves. Due to the random nature of these inhomogeneities, stochastic approaches become necessary for the appropriate description of these features. This makes convenient the use of energy envelopes rather than the full-waveforms because phases are random.

To describe the transport of energy in scattering media, diverse approaches have been proposed. Some of them are the Markov approximation (Sato (1989)), the radiative transfer theory (RTT) (Wu (1985); Margerin et al. (1998)) and the diffusion approximation (Dainty et al. (1974); Wegler and Lühr (2001)). RTT and Markov approximation can well reproduce behaviors occurring at early lapse times. A limitation of Markov approximation is that the wavelengths must be much smaller than the correlation length of the random medium ($\lambda < a$). As a consequence, Markov approximation can well describe the forward scattering regime and the peak delay, but it can not explain the existence of coda waves.

Radiative transfer was initially developed in the field of astrophysics by Chandrasekhar (1960) to describe the transport of light energy in the atmosphere. Wu (1985) introduced RTT in the field of seismology to model the transport of seismic energy in highly heterogeneous and absorbing media for the modelling of seismic energy. This author proposed some numerical examples which consisted in the simulation of energy distribution in space for a point source in the frequency domain. Two scenarios were considered, isotropic and forward scattering. The former assumes that the scattered waves do not have a preferred direction and the latter considers that waves follow predominantly the forward direction after interacting with the inhomogeneity. Based on the effect of the seismic albedo $B_0 = \eta_s/(\eta_s + \eta_a)$ in the shape of the energy-distance curves, this author was able to propose the possibility to separate the two attenuation mechanisms (η_s and η_a are the scattering and absorption coefficients). Fig. 2.4 illustrates the different ingredients being simulated by RTT through an incident flux of energy transporting horizontally. This flux can be reduced due to the scattering into other directions (A) or to the absorption (B). A gain of the flux might be the result of a random walk (C) that was deflected into the same direction of the direct energy or to external sources (D).

Wu and Aki (1988) applied the theory proposed by Wu (1985) for the separation of absorption and scattering properties at the Hindu Kush region. They used 54 earthquake events of small magnitudes with depths up to 350 km. The authors discussed the validity of the exponential decay as a model to describe the apparent attenuation, which can be done only in two cases: either when absorption is dominant or after the emergence of the multiple diffusion regime. Their estimates on the Hindu Kush region suggest that scattering is not the dominant parameter controlling attenuation at the 2-20 Hz frequency range. Above 20Hz, they found the possible existence of a strong scattering surface layer in the crust.

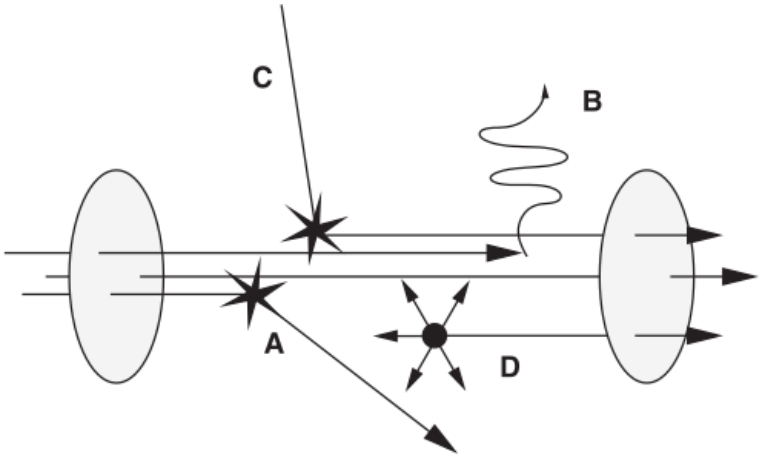

Figure 2.4: Illustration of the different terms represented by the radiative transfer theory in a medium with scattering and absorption properties of an incident flux of energy. Stars represent the scattering events (A and B). Whereas absorption and external sources are given by B and D (Sens-Schönfelder et al. (2009)).

Although its clear applicability in the seismic wave propagation problem, RTT has the reputation of being difficult to solve. Indeed few analytical solutions exist in literature (e.g. Sato (1993); Paasschens (1997)). For instance Paasschens (1997) developed some solutions under the assumption of isotropic scattering for the 2D and 3D cases. Each of them have been extensively implemented for the separation of absorption and scattering properties from real data. An additional assumption in these cases is the dominance either of surface or body waves. With the advent of computational facilities, numerical approximations have allowed to incorporate more complicated conditions on the solution of RTT. Monte Carlo simulations offer the possibility to include the anisotropic scattering as well as the body-to-surface wave conversion. In Monte Carlo simulations, the wave propagation phenomenon is modelled as random walks of particles (or seismic phonons) that are shot from a source. Each particle propagates with the background velocity v_0 and carries a unit energy. The propagation time is statistically controlled by the mean free time τ (ℓ/v_0). Monte Carlo solutions were first introduced by Gusev and Abubakirov (1987). In their pioneering work, these authors were able to reproduce the emergence of coda waves, the amplitude of direct waves, as well as the envelope broadening. A further implementation of the Monte Carlo simulations was carried out by Margerin et al. (1998). They addressed the problem of coda waves in layered media for the contrast between the crust and the mantle, considering two scenarios. The first one, defining the two layers with the same scattering strength and the second one, having a higher scattering strength in the crust than in the mantle. Results evidenced amplification for the first case due to the wave trapping in the crust, and a more significant decrease in the coda wave for the second case, due to the energy leakage between the crust and

the mantle. This simple model of scattering crust overlying a homogeneous mantle was then applied to study the attenuation characteristics of seismic waves in Mexico by Margerin et al. (1999). Their interpretation of the Q_c showed a low contribution of absorption, but the energy decay with time might rather be given by the leakage term. They found that the decay rate of the coda energy is strongly sensitive to the ratio between the mean free path ℓ and the crust thickness H. For example, when ℓ is much larger than H (low scattering) the effect of leakage is small. On the other hand, when ℓ is of the order of the crustal thickness, Q_c is very sensitive to H. The model proposed by Margerin et al. (1998) and Margerin et al. (1999) leads to a different representation of coda Q, which globally is then given by:

$$Q_c^{-1} = Q_{sc}^{-1} + Q_i^{-1} + Q_L^{-1} \tag{2.7}$$

Where Q_L^{-1} represents the loss of energy due to the leakage. At long lapse-times Eq. 2.7 is rewritten as

$$Q_c^{-1} = Q_i^{-1} + Q_L^{-1} \tag{2.8}$$

Same as velocity structures, scattering and absorption properties can also present anomalies in localized regions. Sens-Schönfelder et al. (2009) used Monte-Carlo simulations to investigate the blockage of Lg waves in the Pyrenees. Through 3D numerical modelling in a medium with non-isotropic scattering these authors were able to explain the almost perfect extinction of Lg waves along the Pyrenees. They proposed a model with stronger anomalous scattering and absorption properties in a localized 3D body than in the surrounding crust. Mayor et al. (2014) studied the sensitivity of coda waves to spatial variations of scattering and absorption through a scalar version of the radiative transfer equation. By assuming that the variation of these parameters in space is weak, they adopted a perturbative approach to derive the coda sensitivity kernels to absorption and scattering. These kernels depend on the type of perturbation and the lapse-time in the coda. Additionally, it is necessary to know the angular dependence of the energy. They found that absorption anomalies tend predominantly to modify the decay rate of the coda waves, whereas scattering anomalies would generate either a positive or negative deflection of the energy envelope depending on their location. Those results suggest the possibility to locate scattering and absorption anomalies based on the shape of the envelope of coda waves.

A current frontier in the development of radiative transfer theory consists in the description of the whole wavefield taking into account the conversion from body to surface waves. Such mix of energy might often occur in the late coda, and it has significant relevancy for constraining attenuation properties in a heterogeneous medium. Margerin et al. (2019) formulated a self-consistent theory of RT by considering the propagation of energy in half-space geometry. The coupling of body and surface waves is addressed by representing the Green's function as the sum of these two type of waves. Independent scattering approximations were adopted, from which they defined different scattering mean free paths for surface and body waves. The latter is depth dependent as a result of the body-to-surface coupling. Furthermore, they derived the diffusion approximation from the proposed transport equations and found that diffusivity is also depth dependent and anisotropic.

As it was mentioned at the beginning of this section, the phenomenon of wave propagation in media with small-scale inhomogeneities is characterized by the emergence of different scattering regimes. The multiple diffusion is defined as regime where the angular dependence of the energy density is uniformized and the memory of the initial propagation direction is completely lost. This behavior is often observed at propagation distances larger than the transport mean free path ℓ^* and also at long lapse times where the coda is contained. Due to its mathematical

simplicity, it results convenient to adopt the diffusion approximation (Kourganoff (1969); Weaver (1990)) to simulate the transport of energy in this regime. Sato (1993) demonstrated that in the 1-D and 2-D cases, at long lapse times the radiative transfer solutions converge to the diffusion approximation. This convergence was later demonstrated by Gusev and Abubakirov (1987) for the 3-D cases with Monte Carlo simulations. Fig. 2.5 shows an example of convergence of RTT towards diffusion approximation. This corresponds to the transport of energy in a von Kármán medium with $a = 400$m, $H = 0.25$ and $\varepsilon = 10\%$.

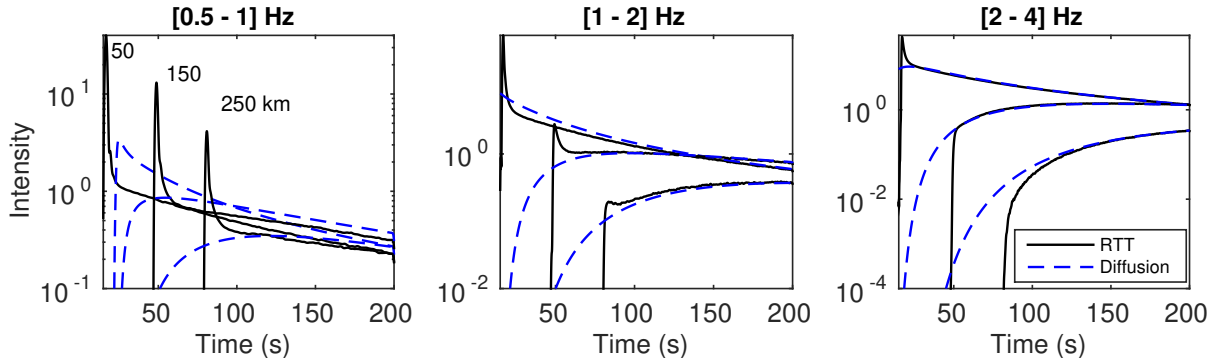

Figure 2.5: Convergence of RTT towards diffusion approximation. Black solid lines represent the Monte Carlo solution of RTT, whereas the blue dashed lines correspond to the diffusion approximation. The example illustrates the behavior at three frequency bands and three propagation distances. The properties of the von Kármán medium are: $a = 400$m, $H = 0.25$ and $\varepsilon = 10\%$.

2.2.3 Full-wave numerical simulations

With the advent of computational power the numerical simulation of the full-wavefield emerges as an alternative way to study the propagation of seismic waves in scattering media (Frankel and Clayton (1986); Imperatori and Mai (2012); Emoto and Sato (2018)). Frankel and Clayton (1986) modelled the seismic wave propagation in random media by using the finite difference method (FD). Their results provided relevant information about the characteristics of short period waves propagating in the heterogeneous earth crust. Three different auto-correlation functions were used, Gaussian, exponential and Self-Similar. Synthetic waveforms suggested that only the latter can explain travel-time anomalies and the presence of coda waves at certain length scales. Shapiro and Kneib (1993) studied the seismic attenuation by scattering considering plane waves propagating in 2-D and 3-D inhomogeneous media. These authors extracted the meanwavefield by performing different types of averaging. First, through the logarithm of the amplitude spectra of the average wave. Secondly, by using the average wave corrected by travel time Sato (1982). Third, averaging the logarithm of the amplitude spectra; and finally by taking the logarithm of the average spectra. They found that significant differences in attenuation estimates can be evidenced between these four approaches and remarked the importance of selecting the appropriate quantity to be averaged.

The so-called coherent wave might experience not only amplitude decay, but also some dispersion associated to frequency dependent travel time fluctuations. By comparing estimates from the Rytov approximation and numerical simulations of the full-wavefield, Shapiro et al. (1996) studied the effect of random inhomogeneities on the phase velocities. They performed FD simulations of plane waves in 2D and 3D random media described by Gaussian and exponential auto-correlation functions. Besides the frequency dependence of the phase velocity, they found that this dispersion is also distance dependent when the propagation distance is much larger than

the size of the scatterer size (a). Furthermore good agreement between numerical and theoretical approaches was found.

In spites of its robustness for the prediction of the transport of energy in media with random heterogeneities, solutions of RTT are based on diverse assumptions regarding the propagation regimes, the scattering strength or the length scales. These approximations might often require to be validated through comparisons with numerical simulations (Przybilla et al. (2006); Wegler et al. (2006); Przybilla and Korn (2008)). Przybilla et al. (2006) proposed an extension of the Monte Carlo solution for the description of the full elastic wavefield, including the P and S components as well as the scattering conversion. These Monte Carlo (MC) solutions were based on the Born single scattering coefficients, which also includes the angular dependence of scattering. The authors validated their method by comparing the MC simulated envelopes with those from FD simulations of the wavefield in 2D random media described by Gaussian and exponential ACFs. Remarkable agreement was found at short and long lapse times, being able to reproduce scattering signatures at forward scattering regime and for a wide range of scattering parameters. Wegler et al. (2006) performed an ensemble of comparisons between FD numerical simulations and diverse theories for the description of energy transport in random media. Thus, these authors calculated energy envelopes from the Markov approximation, diffusion approximation, isotropic scattering and anisotropic scattering. Although, for most of the cases they found good agreement between anisotropic scattering RTT and the FD simulations at early and long lapse-times, at cases with extremely high level of scattering they found some significant differences between the two approaches.

In the context of ground motion, diverse studies have investigated the effects of small-scale inhomogeneities on the site response (Hartzell et al. (2010), Imperatori and Mai (2012), Imperatori and Mai (2015) Takemura et al. (2015), Savran and Olsen (2019), Scalise et al. (2021), Tchawe et al. (2021), van Driel et al. (2021), Hu et al. (2022)). Imperatori and Mai (2012) studied the effect of crust random heterogeneities on the ground motion simulation. They observed that scattering can highly distort the source radiation pattern even at short distances and also produce significant variations in the peak ground velocity (PGV) (see Fig. 2.6). By simulating the 2D wave propagation in the sedimentary basin of Nice Tchawe et al. (2021) evaluated the effect of soil velocity inhomogeneities on ground motion parameters such as PGV and Transfer Functions (spectral ratios). They found that the fluctuation level of the wave velocity has a more significant effect on the spatial variability of the ground motion than the correlation length. Regarding the spectral ratios they observed a reduction of the amplitudes of the mean spectral ratio with respect to the background medium due to the smoothing effect of the averaging procedure.

Numerical simulations of seismic waves in random media also offer the possibility to quantify the level of fluctuations on the average quantities of the wavefield, and more specifically, the mean square intensities. Such level of fluctuation is generally controlled by the scattering strength and the propagation distance. Besides its usability to quantify the epistemic uncertainty on the ground motion predictions, analyses on the fluctuations of the average wavefield are very helpful to study the transition from ballistic to diffusive behaviors. To understand the spatial variability of the ground motion associated to the complex wave propagation effects,Yoshimoto et al. (2015) performed a comprehensive study which included observations on real data, theory and numerical simulations of the full-wavefield. Their results showed that fluctuations increase with frequency and hypocentral distance. From their theoretical approach, these authors proposed an equation to evaluate the amplitude fluctuations of seismic waves propagating in von Kármán media. Furthermore, they found the log-normal density function can properly describe the distribution of fluctuations on the peak amplitudes. Similarly, Emoto and Sato (2018) used 3D numerical simulations through the FD method to analyze the distribution of intensities and

confirmed the dominance log-normal distribution on the peak intensities. By analyzing the time dependence of the intensity distributions they found that the late coda is governed by exponential density functions. These analyses led to understand the transition on time domain from ballistic to diffusive behavior with the aid of simple statistical distribution.

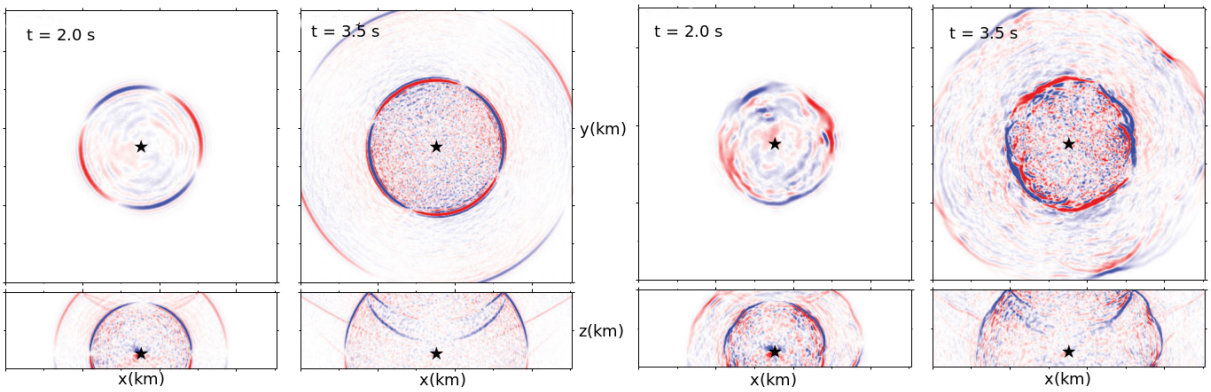

Figure 2.6: Snapshots of wave propagation in random media with (left) 50 m and (right) 5 km of correlation length. The point-source position is indicated by the black star. Both map view and vertical section are shown. The vertical plane is parallel to the x-axis and cuts the y-axis at 16 km. All panels are shown with same amplitude scale. Taken from Imperatori and Mai (2012)

2.3 Scattering and absorption separation

In the previous section we discussed some basic concepts about the wave propagation in scattering media. Different approaches for the description of scattered waves were shown, from the theoretical models for the energy transport to the numerical simulations of the full-wavefield. In all these cases the statistical properties of the medium are assumed to be known. In this section we show how those theoretical models have been used to constrain scattering properties and absorption. To separate these two mechanisms, it is therefore necessary to compare observations of the wavefield, which are given by the energy envelopes of seismic records, with their theoretical counterpart (either from RTT or diffusion approximation). A minimization of the difference between observations and predictions will then lead to a direct estimation of scattering and absorption parameters. Regardless of the inverstion technique, most of the strategies to separate attenuation mechanisms rely on the idea that scattering controls mainly the amplitude decay with distance of the so-called ballistic waves, whereas absorption defines how fast the energy decreases with time (as illustrated in Fig. 2.2).

Most of the existing works for the estimation of scattering and absorption properties make use either of earthquake data (Fehler et al. (1992); Hoshiba (1993); Carcole and Sato (2010); Ugalde et al. (2010); Eulenfeld and Wegler (2016)) or active shots (Prudencio et al. (2013), Wegler and Lühr (2001)). The inversion techniques can globally be divided in two groups: those based on the multiple lapse time window analysis (MLTWA) and the ones exploiting the whole energy envelope as much as the signal-to-noise ratio allows it.

2.3.1 MLTWA

The multiple lapse time window analysis (MLTWA) was first introduce by Fehler (1991) for the separation of scattering and absorption attenuation. This technique is based on the space

evolution of the integrated (or averaged) energy in three time windows representing different propagation regimes. The first one corresponds to the ballistic components of the wavefield plus some recognized contribution of scattered waves. The second and third windows are expected to be dominated by multiply scattered waves. The main assumption of this technique is the treatment of scattering as isotropic, as well as a uniform distribution of scatterers and absorbers. Attenuation mechanisms are measured based on the distance dependence of the integrated energy. Hoshiba (1991) showed that scattering estimates are strongly dependent on the size of the window chosen for the time integration. For example, when the time window is so large, the fitting procedure might lose some sensitivity to scattering. Based on this observation, a further improvement of the method was later implemented by Fehler et al. (1992). They proposed to estimate attenuation mechanisms by using two integrated energy ratios: the first one, corresponds to the energy integrated in the "ballistic" regime observed at a short epicentral distance divided by the "ballistic" energy of a receiver located at a longer distance. The second ratio is calculated by dividing the ballistic energy at a long distance over that in the multiple diffusion regime (late coda window) at the same epicentral distance. Their results showed an improvement in the accuracy of scattering and absorption estimates. The basic steps of the multiple lapse time window analysis can be summarized as:

(i) For a receiver at a given epicentral distance r_1, the energy is integrated in three time windows T_1, T_2 and T_3. The integration is repeated for other receivers with different epicentral distances. For example: r_2, r_3 and r_4 (see Fig. 2.7-left).

(ii) Integrated energies are normalized with respect to a reference window in the late coda regime in order to remove the source and site effects. This is called coda normalization (Aki (1980)).

(iii) Thus, three curves of normalized energies versus distance are built for each time window (see Fig. 2.7-right).

(iv) Scattering and absorption parameters are estimated by choosing the best-fit parameters between observed and RTT distance-dependent energy curves. Where the residual between observations and RTT predictions can be quantified as:

$$SSR = \sum_{i=1}^{3} \sum_{j=1}^{M} [\log(\frac{E_{RTT}(t_i,j)}{E_{obs}(t_i,j)})]^2 \tag{2.9}$$

In Eq. 2.9 E_{RTT} and E_{obs} are the modelled and observed average energy densities in the time window i for a path j. M is the total number of paths, which might or not include in the same minimization algorithm several earthquakes for the region of interest.

Diverse applications of the MLTWA have been carried out on several geological contexts (Ugalde (2002); Carcole and Sato (2010); Ugalde et al. (2010)). At a large scale, Carcole and Sato (2010) obtained high resolution maps of scattering and absorption parameters by using the MLTWA. They used S-wave data at the 1 to 32 Hz band and showed that variations on attenuation properties were closely related to the tectonic and volcanic contexts in Japan. Ugalde (2002) estimated attenuation properties in the central-western region of Colombia at frequencies between 1 and 15 Hz. They found clear frequency dependence of the mechanism dominance. For instance, scattering was found to be dominant at 1 Hz and around 14 Hz, whereas both mechanisms contribute equally to total attenuation for the intermediate frequency bands (from 3 to 10 Hz).

Although the basis of the MLTWA assume that scattering is anisotropic and uniformly

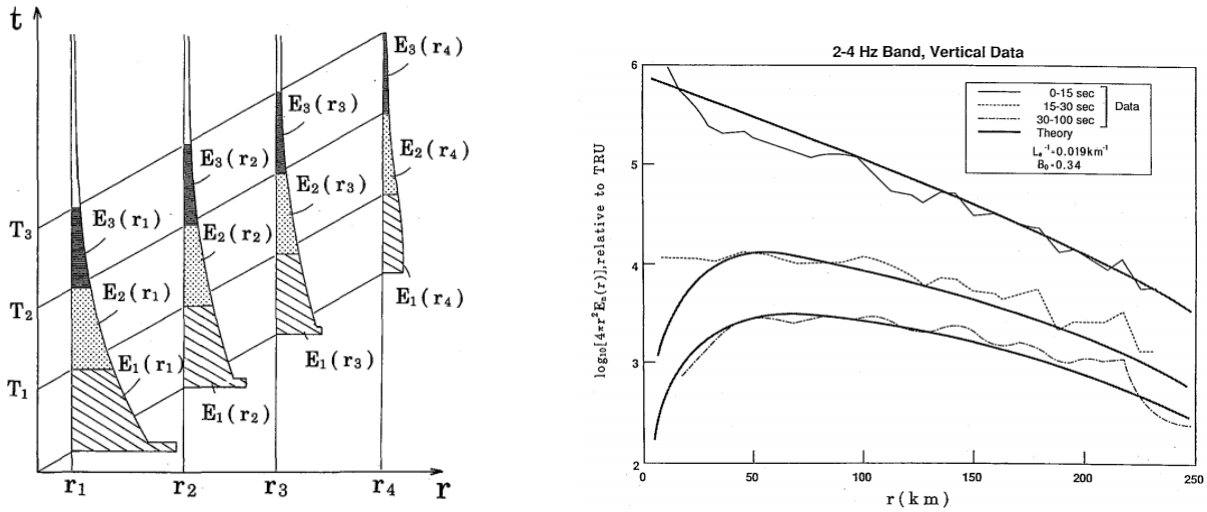

Figure 2.7: (Left) Calculation of integrated energies $E1$, $E2$ and $E3$, in three time windows $T1$, $T2$ and $T3$, for each epicentral distances (from r_1 to r_4). (Right) Fitting scheme of the RTT distance dependent energies to observations. Each curve corresponds to a time window. Taken from Fehler (1991)

distributed, Calvet et al. (2023) estimated attenuation properties in Taiwan by implementing a modified version of the MLTWA technique. They modelled the spatio-temporal evolution of seismic energy by including anisotropic scattering in their Monte Carlo simulations. This allowed them to explain the anomalous attenuation in certain regions of the island with strong backscattering, which they proposed to be related to the large impedance fluctuations induced by the presence of fluids.

2.3.2 Full-envelope based approach

The use of the MLTWA has allowed to understand the propagation properties of diverse geological contexts. However, its application requires a dense array of seismic receivers since the attenuation properties are based on the space energy distribution of a specific region. This requirement becomes even more strict when one is interested in estimating the space variations of attenuation properties because several sub-regions with multiple receivers must be considered (e.g. Carcole and Sato (2010); Calvet et al. (2023)). Additionally, the choice of the duration of the multiple windows is expected to be consistent with the order of the attenuation level to be estimated. This represents a difficulty since one might incur in a mixture of propagation regimes which can affect the sensitivity of integrated energies to certain attenuation mechanism.

Alternative techniques to separate scattering and absorption mechanisms are based on the inversion of the whole energy envelope. These techniques make use either of RTT or the diffusion approximation. Sens-Schönfelder and Wegler (2006b) proposed a joint inversion based on the isotropic assumption of RTT for the estimation of not only the attenuation characteristics but also for the site and source parameters. Thus, the coda normalization technique was not required for the correction of site and source effects. They used 11 earthquakes distributed across the German territory. Their estimations of the seismic moment were more accurate than those from techniques based on empirical relations of local magnitudes. One of the most interesting aspects for the retrieval of scattering and absorption properties is the use of the full S-wave envelope. In this way, instead of comparing three points per energy envelope (as in MLTWA), the authors exploited the ensemble of ordinates of the whole record as much as the signal-to-noise ratio

allowed it. Since RTT can not take into account several effects occurring at the ballistic pulse, such as peak broadening and wandering effects, Sens-Schönfelder and Wegler (2006b) proposed to average the energy contained in a short window around the peak amplitude. This average ballistic energy is the key observable to constrain scattering attenuation, whereas the shape of envelope tail is mainly controlled by absorption.

Eulenfeld and Wegler (2016) implemented some improvements on the method proposed by Sens-Schönfelder and Wegler (2006b), which consisted in the simultaneous inversion of attenuation, source and site effects. This technique is called as Q_{open} and it has been widely used in further works (e.g. Eulenfeld and Wegler (2017); Ranjan and Konstantinou (2020); van Laaten et al. (2021)). To understand the implications of the use of isotropic or anisotropic scattering assumption, Gaebler et al. (2015) compared attenuation estimates from each of these hypotheses. We remind the reader that whereas in the isotropic assumption there is not distinction between the scattering mean free path ℓ and the transport mean free path ℓ^*, in the anisotropic case these two parameters can be obtained separately. Results of (Gaebler et al., 2015) showed that ℓ^* is the only scattering property that can be measured with enough confidence. Their results also suggested that the retrieved attenuation length from the isotropic assumption should be interpreted as ℓ^*. Q_{open} method and the MLTWA are so far the most used inversion techniques to separate scattering and absorption properties. van Laaten et al. (2021) performed a set of comparisons between attenuation properties estimated from these two techniques. They found good agreement in terms of the absolute values of both attenuation mechanisms over their whole range of frequencies. Regarding the error magnitudes they found small discrepancies, which evidenced a higher accuracy for the Q_{open} method. Fig. 2.8 synthesizes the way each inversion technique makes use of the observed energy envelopes. Whereas MLTWA only uses three points representing the energy contained in different time windows, Q_{open} exploits the whole energy envelope.

At extremely heterogeneous media, propagating waves might exhibit records where the wavefield is dominated by multiply scattered waves. In these cases, the use of diffusion approximation might be convenient due to its mathematical simplicity. This is the case of attenuation estimates in some volcanic areas (Wegler and Lühr (2001) ; Wegler (2004); Prudencio et al. (2013); Prudencio et al. (2015)). Since seismic records dominated by multiply scattered waves do not allow to distinguish ballistic portions of the wavefield, it is not possible to separate possible scattering regimes in different time windows as in the MLTWA. This makes necessary the use of a full-envelope inversion technique, based on the diffusion approximation. Wegler and Lühr (2001) used active shots at Merapi volcano (Java)to estimate attenuation properties at the frequency band 4-20 Hz. They used 30 seismometer with propagation distances up to 3 km. Their results showed transport mean free paths of the order of 100 m, which also validated the use of the diffusion model since the estimated ℓ^* was much shorter than their average propagation distance.

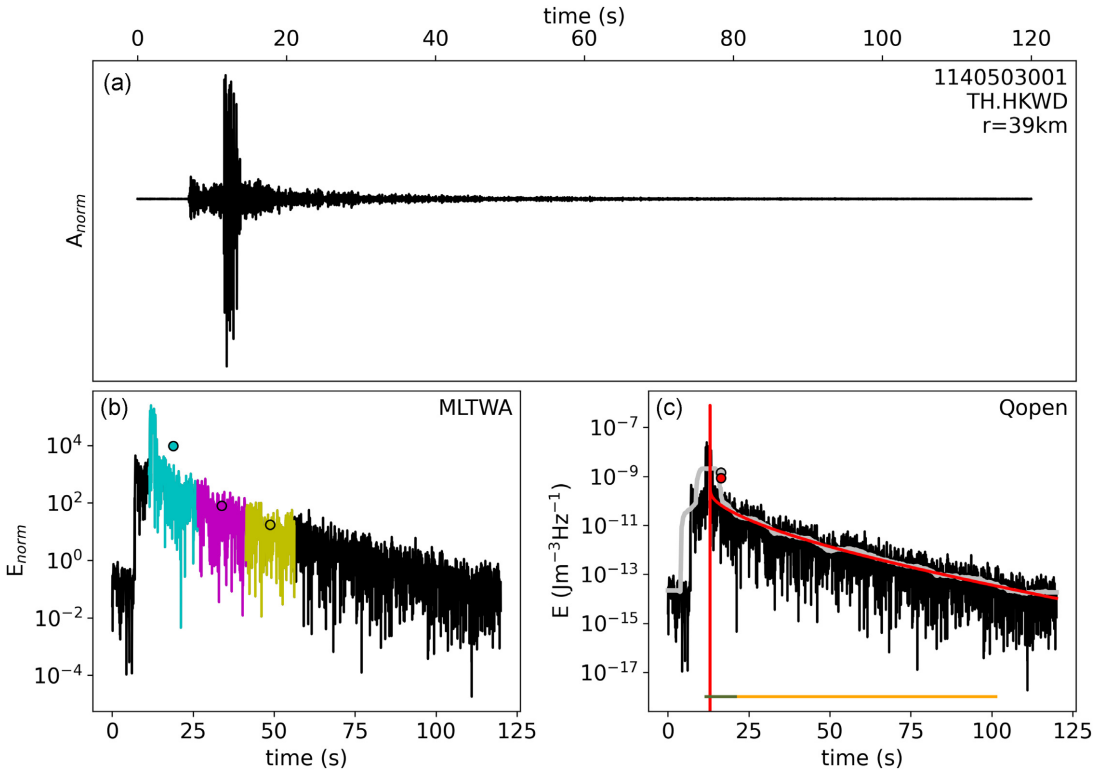

Figure 2.8: (a) Example of recorded seismogram at an epicentral distance of 39 km. The corresponding energy envelope is shown at the bottom. (b) Illustration of MLTWA method with three time windows of 15s duration. (c) Q_{open} method with the smoothed observed envelope over 2 s (grey) and the modelled energy envelope (red line) from the best-fit attenuation parameters. Horizontal lines in orange and olive colors represent the coda and the S-direct wave windows, respectively. The circles correspond to the averaged energy in the direct wave window. Taken from van Laaten et al. (2021).

2.4 The use of seismic noise in attenuation estimates

To investigate the inner structure of the earth, a possibility is to use natural earthquakes or active shots. This has allowed to retrieve wave velocities and attenuation properties which have provided interesting interpretation on the material composition of the earth. However, the use of earthquake sources are limited to regions with high seismicity and that are well instrumented. In the context of small-scale areas, such as sedimentary basins, mapping propagation characteristics becomes also difficult due to the disability to perform measurements with localized sensitivity. Regarding active shots, the required seismic experiments are generally expensive. In the last decades, the use of seismic noise has been extensively used to study the inner structure of the earth (Shapiro and Campillo (2004); Shapiro et al. (2005); Stehly et al. (2008)), as well as to monitor seismic velocity changes (Sens-Schönfelder and Wegler (2006a); Brenguier et al. (2008); Rivet et al. (2014); Mordret et al. (2016)). In a similar way, attenuation properties might be retrieved at small-scale geological contexts by using seismic noise. This has allowed the mapping of physical properties which are sensitive to the area of interest. In this section we present a short review on the use of cross-correlation functions of seismic noise seismic noise to image elastic parameters, from surface wave velocities to scattering and absorption attenuation.

2.4.1 Noise-based imaging

The cross-correlation functions (CCF) of seismic noise are expected to contain information on the earth's subsurface as valuable as that from natural earthquakes or active shots. Thus, in the case where CCFs can properly represent a seismic wavefield, one might be able to retrieve direct (surface or body) and multiply scattered waves.

The main principles of the noise-based imaging state that the cross-correlation between two diffused fields recorded at locations x_1 and x_2 is proportional to the Green's functions between this two points. Where the resultant signal is composed by a causal part, representing the response at point x_2 generated by an impulse source at x_1, and the acausal part is expected to represent the response at x_1 for a source at x_2. The potentially retrieved empirical Green's function can thus be used to estimate propagation velocities and seismic wave attenuation. The appropriate retrieval of empirical Green's function require that the phase of the wavefield is completely random, and that all the vibration modes of the propagation medium are excited with the same level of energy. This is known as the mode equipartition condition. The use of cross-correlated diffused fields to retrieve Green's functions was first introduced in the field of acoustics (Weaver and Lobkis (2001) Lobkis and Weaver (2001)) through laboratory experiments of ultrasonic and thermal noise. Weaver and Lobkis (2001) showed that the auto-correlation of thermal noise recorded at the surface of an aluminum block corresponds to the Green's function for the case where the source and receiver have the same location. The same idea was then demonstrated for the case of cross-correlation by using two receivers with certain separation (Lobkis and Weaver (2001)). However, these first studies were performed under conditions different to those from the solid earth, such as the absence of wave attenuation.

The application of diffused waves correlations in the field of seismology was initially carried out by Campillo and Paul (2003). Previous work on mode equipartition had revealed the diffused character of coda waves (Hennino et al. (2001)). In their pioneering work, Campillo and Paul (2003) performed cross-correlations of late coda records for 101 earthquakes to retrieve empirical Green's functions. The observed polarization characteristics and group velocities of the extracted pulse corresponded to the typical signatures of Rayleigh and Love waves. Those observations evidenced the potential applications of cross-correlated diffused fields in the solid earth to estimate elastic properties. Shapiro and Campillo (2004) demonstrated that similarly to coda waves, the seismic ambient noise (as a diffused field) can also be used to reconstruct direct surface waves. Their observations suggested the possibility to estimate dispersion curves in a broadband of periods (even at short periods of few seconds if the stations are close enough) with some particular advantages with respect to earthquake or active shots-based approaches: (i) the measurements can be performed for any propagation direction; (ii) The sensitivity zone is localized at the region connecting the two receivers. It is worth mentioning that further work have evidenced that the complexity of propagation characteristics in the study area, as well as the noise sources distribution can play a major role for the stable retrieval of empirical Green's functions. From long-term cross-correlation of seismic noise, Stehly et al. (2006) studied the sources of the background noise using stations in North America, western Europe and Tanzania. The azimuthal distribution of the energy evidenced that at the shortest periods (secondary microseism), the noise sources do not have significant seasonal variations. This observation confirmed that at such period band the noise is generated by the interaction of ocean swell with the coast. Long periods (primary microseism) exhibit an opposite behavior, with a clear seasonal dependency that might affect the quality of the reconstructed Green functions.

As mentioned above, the accurate retrieval of empirical Green functions requires that the noise sources are uniformly distributed. In practice, this is not always the case, as noise sources

might have some preferential direction. In contrast, coda waves are expected to be less sensitive to the source anisotropy, however their records are short and rare. In order to profit of the long records of continuous ambient noise and the diffuse character of coda waves, Stehly et al. (2008) proposed the use of the correlation of the coda of the correlation ($C3$). Their analyses showed the possibility to reconstruct the Green's function for which the first other noise correlation is not appropriate. Additionally, the efficiency of their method evidenced that the first other noise cross-correlation can properly retrieve the multiply-scattered components of the Green's function.

Some theoretical work on the retrieval of Green's functions from diffused fields in elastodynamics can be found in Wapenaar (2004), Roux et al. (2005) Sánchez-Sesma and Campillo (2006), Sánchez-Sesma et al. (2006) and Gouédard et al. (2008).

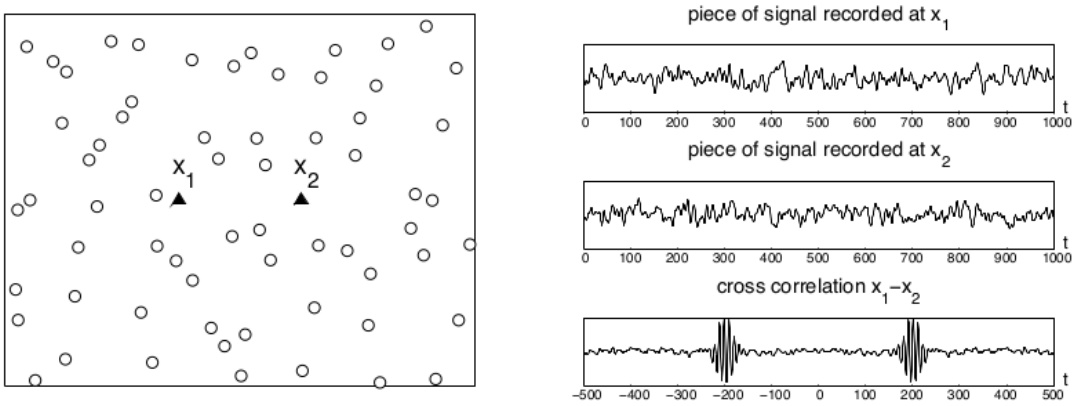

Figure 2.9: Cross-correlation of seismic noise. Stations x_1 and x_2 recording incoherent noise coming from different sources (circles). Left-bottom cross-correlation function between records at x_1 and x_2. Stehly, PhD thesis (2007).

2.4.2 Noise-based attenuation

In most of the works aforementioned, surface wave velocities are the physical quantities extracted from the cross-correlation of seismic noise. Even in cases of monitoring of small changes in solid earth materials, the classical dv/v measured from coda waves, focuses on the velocity shift associated to scattering perturbations (Sens-Schönfelder and Wegler (2006a)). Attenuation properties can also provide with valuable information about the current state of a geological structure. Previous works on the noise-based attenuation measurements have focused on the ballistic components of the reconstructed wavefield (e.g. Prieto et al. (2009); Denolle et al. (2014); Liu et al. (2015); Haendel et al. (2016); Stehly and Boué (2017); Magrini and Boschi (2021)), other works utilize the retrieved coda waves (Soergel et al. (2019)), and recently, for the growing interest in the separation of scattering and absorption mechanisms, some authors make use of the portions of the wavefield comprising the ballistic and coda regimes (Hirose et al. (2019); Hirose et al. (2020); van Dinther et al. (2020); Hirose et al. (2022)).

Interpreting the information carried by the amplitudes of CCFs might be more complicated than that from the travel times. By comparing experimentally the impulse response obtained from an active source with that retrieved from cross-correlation of noise, Larose et al. (2008) demonstrated that the decay rate of direct waves reconstructed from random incoherent waves agrees with the geometrical spreading and the 'anelastic' structure of the material.
At a regional scale, Prieto et al. (2009) developed a technique to estimate seismic attenuation

and phase velocity dispersion by measuring the coherency of seismic noise for several couples of receivers, as a function of frequency and distance. Thus, they were able to obtain attenuation models which exhibited the signatures of major sedimentary basins of California. Soergel et al. (2019) exploited the coda waves of CCFs at different period bands between 2.5-20 s to estimate Q_c in the Alps region. For short inter-station distances they found that there were not significant effect of noise sources directivity. Furthermore, Q_c measurements exhibited stable geographical patterns at period bands between 2.5 and 10 s. This observation was different at longer periods, where the geographical pattern became speculative. The authors also outlined the fact that due to the relatively short coda durations, they were not able to perform the separation of scattering and absorption mechanisms. Overall their results suggested the potential of seismic noise to perform attenuation estimates at frequencies lower than those often analysed from earthquake data.

Hirose et al. (2019) implemented by first time the use of CCFs for the separation of absorption and scattering attenuation at Sakurajima volcano. These authors obtained similar estimates to those from active shots. Their estimates were performed at frequencies ranging from 0.5 to 4 Hz. To invert for absorption and scattering parameters, Hirose et al. (2019) used a technique based on the MLTWA. These measurements were obtained by comparing the observed energy envelopes of the CCFs with those from the 2D solution of RTT for surface waves. As expected for volcanic environments, they found that scattering was the dominant attenuation mechanism at the considered frequency bands. Similarly, van Dinther et al. (2020) used CCFs to study lateral variations of scattering properties in the North Anatolian Fault (NAF) zone through MLTWA. They divided the NAF zone in four sub-regions where attenuation measurements were performed independently. Their results showed well constrained and stronger values of scattering attenuation near the faulted area than in the surrounding crust. Those observation evidenced the potential to monitor the evolution of scattering properties near a faulted environment using seismic ambient noise. Further application of the method developed by Hirose et al. (2019) have been carried out to locate spatial changes of scattering generated by earthquakes (Hirose et al. (2020)) and to quantify attenuation properties of 18 volcanoes in Japan (Hirose et al. (2022)).

2.5 The contribution of this work

We showed a review on the existing works in literature for the separation of scattering and absorption properties, which have been widely used in the field of seismology. Most of them have been performed at continental and regional scales by using earthquake data. At a local scale, which is the interest of engineering seismology, attenuation studies have focused on the estimation of the apparent attenuation characterized either by the so-known κ parameter or by the total quality factor Q. However, a more detailed estimation on the mechanisms that control seismic attenuation would be necessary to better understand the extreme variability of the ground motion, as well as the frequency dependence of the amplitude decay. The conventional earthquake-based approaches would be limited to regions with high seismicity, as well as strongly dependent on the source characterization. Furthermore, the sensitivity of earthquake coda waves is distributed over a much wider area than that of a sedimentary basin. The use of noise-based techniques would allow to perform measurements from observables sensitive to more localized structures. This is due to the possibility to reconstruct propagating waves (from CCFs) traveling in the path of a given couple of stations, which are previously located in the area of interest.

In this work we study the attenuation of seismic waves in highly heterogeneous media by using full-wave numerical simulations, theoretical models of the energy transport, and observations

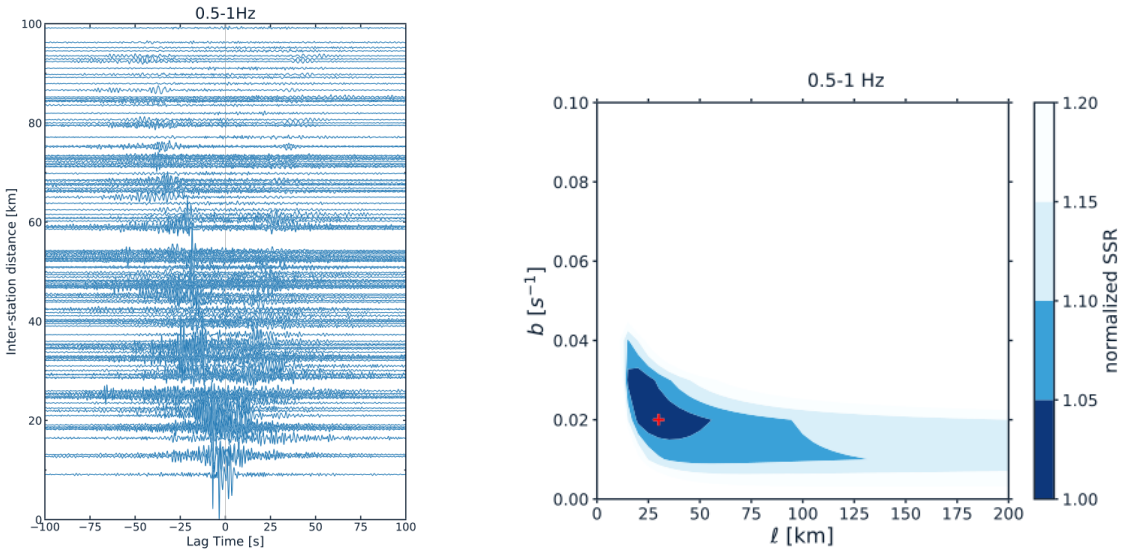

Figure 2.10: (Left) Example of seismic ambient noise CCFs in the [0.5-1]Hz band and inter-station distance ranging from 9 to approximately 100 km. (Right) 2D-grid search for the estimation of scattering (ℓ) and absorption (b), showing the best-fit parameters (red cross) after comparing CCFs energy envelopes with those from RTT. Taken from Hirose et al. (2020)

from seismic ambient noise data. Thus, our work can be globally divided into two components. The first one consists in a comprehensive study of the wave propagation in 2D media with random inhomogeneities, in which we exploit the length scales controlling the behavior of seismic waves. Previous works had made use of numerical simulations of the full-wavefield to understand the effects of random inhomogeneities on the earthquake ground motions (Imperatori and Mai (2012); Hartzell et al. (2010); Tchawe et al. (2021)). However, few of them have evaluated the accuracy of their numerical simulations or controlled the propagation regime they were simulating. By comparing results from simulations of the full-wavefield with those from existing theoretical models such as the mean field and the radiative transfer theories, we propose a verification procedure that we consider necessary to properly understand the behavior of high-frequency ground motions. Furthermore, by analyzing the transport of energy from the envelopes of the full-waveforms, we were able to study the interaction of different scattering regimes, from ballistic to diffusive behaviors. We paid particular attention to the peak energy envelope, which is a key parameter for the seismic hazard assessment but also for the estimation of attenuation properties when using real data. Thus, by studying the decay properties and the statistical fluctuations of the peak energy we shed some light on the role of two scattering length scales, the scattering mean free path and the transport mean free path.

The second component of this work focuses on the estimation of scattering and absorption properties from seismic ambient noise at environments with scales similar to those from volcanic and sedimentary basins contexts (from hundreds of meters to tens of kilometers). We propose a technique to separate the two mechanisms controlling seismic attenuation. Such technique consists in profiting the advantages that different ranges of propagation distances can exhibit. Thus, we perform attenuation measurements in two stages: (i) in the first one we constrain absorption properties by using short propagation distances as energy envelopes have coda long enough to measure a robust decrease with time; and secondly (ii) scattering attenuation is estimated at long propagation distances since the effects of small-scale inhomogeneities become more significant with distance.

Chapter 3

Propagation of SH waves in 2D random media: the coherent wavefield

Estimating the ground motion at high frequency requires to account for small-scale heterogeneities, which can only be described in a stochastic way. Several works have studied the effects of small-scale inhomogeneities on the prediction of the earthquake ground motions, however very few have verified the accuracy of their numerical solutions. In this work we present a verification procedure and some analyses of SH wave propagation in 2D random media which focuses on the properties of the coherent wavefield. The random media consist in correlated density and velocity fluctuations described by a von Kármán auto-correlation function with a Hurst coefficient of 0.25 and a correlation length $a = 500$ m. The Birch correlation coefficient which relates density to velocity fluctuations takes 4 possible values between 0.5 and 1, and the standard deviation of the perturbations is either 5% or 10%. Spectral element simulations of SH wave propagation excited by a plane wave are performed for normalized wavenumbers (ka) up to 5. As parameters of verification we measure the scattering attenuation and phase velocities of the coherent wave. We perform comparisons between our SEM estimates and calculations from the mean field theory. Under the assumption that the random media are ergodic, we perform diverse strategies to average the wavefield. The first one, by using the ensemble average over several realizations. Secondly, we use the horizontal space average over several receivers located at common distances to the source. And the third one, through the ensemble-space average. Thus, by comparing attenuation estimates from these three averaging types, we evaluate the effect of the number of realizations on the accuracy of our results. Our analyses suggest that space and ensemble-space averages allow to predict well the scattering attenuation of the target random media. Excellent agreement is found between the SEM measurements and the meanfield theory when comparing the scattering attenuation. However, the analyses on the phase velocity exhibit some significant mismatch which might require the focus of future works.

Keywords: numerical simulation, random media, scattering, coherent wavefield, attenuation, phase velocity.

3.1 Introduction

Small-scales inhomogeneities can significantly modify the characteristics of propagating waves at different geological environments such as, the earth's crust, volcanoes and sedimentary basins. These heterogeneities are so far considered as random and they are the responsible of the so known seismic scattering. Thus, depending on their contrast with the back ground properties of the medium and the propagation regime, the interaction of direct waves with random inhomogeneities can significantly shape the recorded ground motion. Some of the main signatures of scattering are, the attenuation of direct waves, peak delay, peak broadening and the emergence of coda waves. The challenge of seismologists is to be able to reproduce and identifying these features in order to gain a deeper understanding on the inhomogeneous structure of the earth.

For the description of wave propagation in random media, diverse approaches have been proposed. One of the most popular is the radiative transfer theory (RTT) (Wu, 1985) (Margerin et al., 1998). This phenomenological model can predict the spatio-temporal evolution of seismic energy in absorbing and highly heterogeneous media. It has been widely used for the separation of scattering and absorption effects (Fehler et al. (1992); Hoshiba (1993); Carcole and Sato (2010)). Another approach is the mean field theory, which aims to quantify scattering properties based on the signatures of the coherent wavefield (Sato (1982); Wu (1982); Hudson (1990)). Both approaches are based on average quantities on the wavefield: on one hand, RTT makes use of mean energy densities and it neglects the phase information; on the other hand, the mean field theory utilizes the ensemble average of the full-waveforms. Additionally, depending on the representation of the wavefield, different attenuation parameters can be retrieved. This last point will be part of the discussion in next chapter.

Besides the theories above mentioned, numerical simulations of the full-waveform are also a helpful tool to understand the phenomenon of wave propagation in random media (Frankel and Clayton (1986); Emoto and Sato (2018); Imperatori and Mai (2012)). Frankel and Clayton (1986) modelled the seismic wave propagation in random media through the finite difference method (FDM). Their results provided relevant information about the characteristics of short period waves in the earth's crust. Through those simulations they were able to reproduce travel time anomalies and the emergence of coda waves; By using 2D and 3D numerical simulations of wave propagation in inhomogeneous media, Shapiro and Kneib (1993) studied the seismic attenuation by scattering. These authors found that different types of averaging the wavefield can lead to different estimates of scattering attenuation and remarked the importance of selecting the appropriate quantity to be averaged.

Theoretical approaches often require to be validated by comparisons with numerical simulations of the full-wavefield (Przybilla et al. (2006); Wegler et al. (2006)). Przybilla et al. (2006), compared energy envelopes of the Monte Carlo solution of RTT with those from 2D numerical simulations of the wavefield using FDM. For the Monte Carlo solution they included P-S conversion scattering with angular dependent scattering coefficients, getting significant agreement between the two approaches for short and long lapse times.

The effect of scattering on the ground motion prediction is nowadays an active field of reaserch (Hartzell et al. (2010), Imperatori and Mai (2012), Imperatori and Mai (2015) Takemura et al. (2015), Savran and Olsen (2019), Scalise et al. (2021), Tchawe et al. (2021), van Driel et al. (2021), Hu et al. (2022)). For example Imperatori and Mai (2012) studied the effect of crust random heterogeneities on the ground motion simulation. They observed that scattering can highly distort source radiation pattern even at short distances and also produce significant variations in the peak ground velocity (PGV); By simulating the 2D wave propagation in the sedimentary basin of Nice Tchawe et al. (2021) evaluated the effect of soil velocity inhomogeneities on ground motion

parameters such as PGV and Transfer Functions (spectral ratios). They found that randomized velocities can lead to a significant spatial variability as the coefficient of variation of the velocity increase.

Despite the valuable efforts in considering scattering for the ground motion estimation, the results of most of these works remain difficult to interpret due to the lack of control and verification to guarantee that the targeted random media are properly implemented. In this work we present a verification procedure through a set of comparisons between wave propagation simulations and theoretical solutions. We used the attenuation and dispersion properties of the mean wavefield as the quantities to be analyzed. Verifications of scattering attenuation are carried out by comparing measurements when different averaging procedures for the coherent wavefield are used. This enables us to observe the effect of the number of realizations (or waveforms) on attenuation estimates and its agreement with the Dyson's equation solution. Secondly, we measure the phase velocity dispersion associated to scattering based on the distance dependence of the phase difference. These two sets of comparisons put in evidence the robustness of our numerical simulations and the proposed verification procedure. A third phase of this verification procedure is included in chapter 4, in which we exploit the mean energy envelopes.

The first part of this document contains the theoretical background in which we show some concepts of wave propagation in random media, and we also introduce the mean field theory from which some equations were used to compute scattering attenuation. The numerical settings of the 2D full-wavefield simulations as well as the extraction of the coherent wavefield, are presented in Section. 3.2.3. In section 3.3 we present scattering estimates from both, numerical simulations and the theoretical approach. This includes the analyses on the effects of the number of realizations to retrieve the scattering attenuation. Phase velocity measurements are shown Section. 3.4 with their corresponding comparisons with the Dyson's solution. Finally, some onclusions are presented in Section. 3.5.

3.2 Methods

3.2.1 Wave propagation in random media

The interaction of primary waves with small-scale inhomogeneities can generate the emergence of diverse propagation regimes. The first regimes is known as ballistic, and it is predominantly controlled by primary waves. This regime is expected to keep both, the direction of the wavefront and the source signature. Due to the interaction with the inhomogeneous earth, the ballistic waves can experience attenuation as distance increases. In chapter 4 we will show that the so called "ballistic" waves are not purely composed of direct coherent waves but multiply diffused waves can also contribute to it. This is known as a quasi-ballistic behavior, however in the present chapter we will still refer to the first portion of the wavefield as ballistic waves; A second regime corresponds to the waves that have been scattered once and it is known as single scattering; the last regime corresponds to the energy that has been redistributed and comes to the receiver as late coda waves and its level of fluctuation depends on the scattering strength. In fig 3.1 we show the appearance of ballistic and diffusive regimes for the case of a plane waves propagating upward in a 2D medium with random inhomogeneities. The initial part of the wavefield is controlled by a well pronounced front of ballistic waves and it is then followed by multiply diffused coda waves. Fig 3.1 (right) shows two representations of the wavefield: a seismogram (top) and its energy envelope (down). The vertical green lines bound the possible ballistic wave and the green arrow shows the emergence of the diffused field with time.

Apparent attenuation of ballistic waves with distance is one of the most important evidences

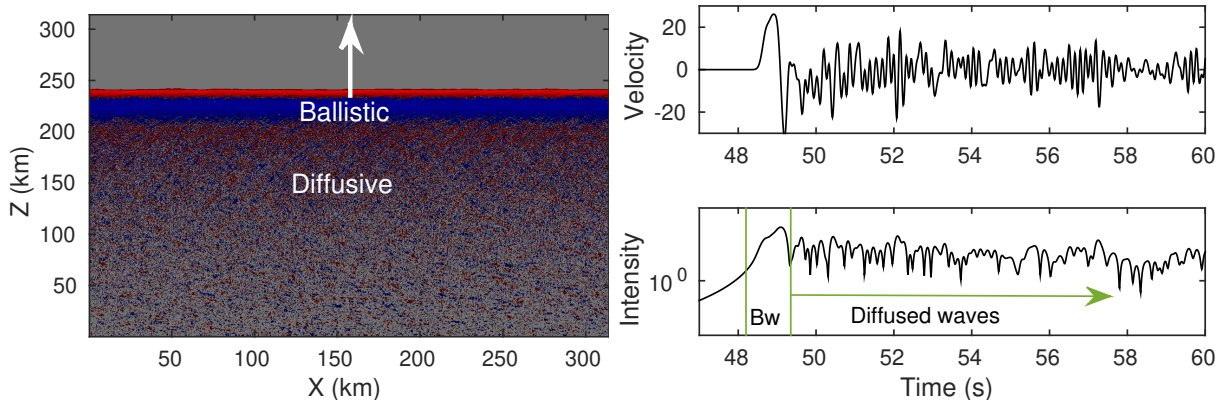

Figure 3.1: Example of ballistic and diffusive portions of the wavefield. Left: plane wave propagating vertically in a medium with random heterogeneities. The upper part represents the direct (ballistic) wave which is then followed by multiply diffused waves. Red/blue colors indicate possitive/negative particle velocity. Right: synthetic seismogram for a receiver located at 150 km from the source (top) and corresponding energy envelope (bottom). Vertical green lines indicate possible limits of the ballistic regime (Bw) and green arros describes the emergence of diffused coda waves with time

of scattering. To illustrate this signature, in Fig. 3.2 we compare the seismic profile of a wave propagating in a random medium (red) with that from an homogeneous medium (black). Waveforms were recorded by receivers spaced every 25 km. The circles indicate the peak amplitude contained in the ballistic regime. Since we do not include absorption, the amplitude of the direct wave in the homogeneous case is expected to be constant. For the heterogeneous case, the amplitude decreases significantly with distance, in contrast to that of the homogeneous case. Additionally, we can see that the emergence of diffused waves become more important with distance.

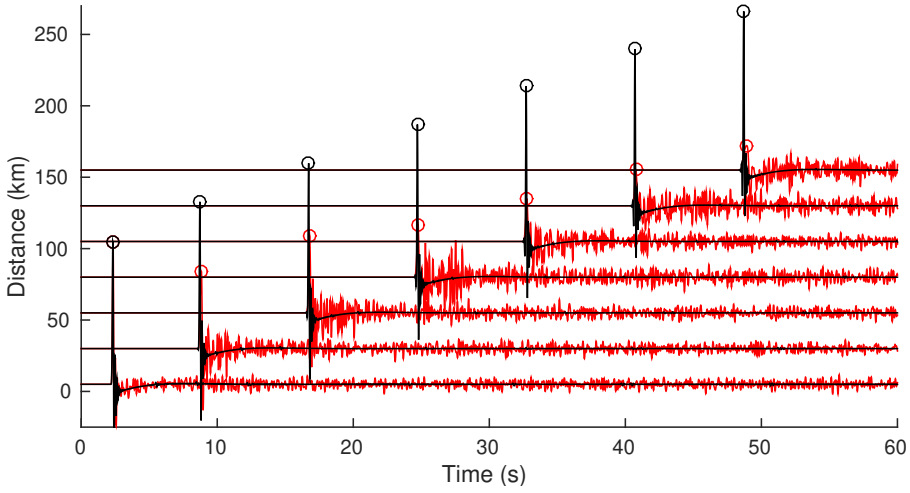

Figure 3.2: Comparison of 2D plane wave propagation in homogeneous medium (black) and random medium(red). The figure highlights the effect of attenuation in the ballistic portion. Additionally the emergence of diffused coda waves in the long-lapse time. Seismograms correspond to receivers spaced every 25 km, ranging propagation distances from 5 to 155 km.

The wave propagation of a scalar wave in a 2D medium with random inhomogeneities can be

described by the wave equation:

$$\rho(\mathbf{x})\frac{\partial^2 u(t,\mathbf{x})}{\partial t^2} - \nabla\cdot(\mu(\mathbf{x})\nabla u(t,\mathbf{x})) = f(t,\mathbf{x}), \tag{3.1}$$

where μ and ρ represent the shear modulus and the density, respectively, and $\mathbf{x}$ is a vector quantity denoting the position. The external source is given by $f(t,\mathbf{x})$ and the wave velocity is defined by the so know expression as $v(\mathbf{x}) = \sqrt{\mu(\mathbf{x})/\rho(\mathbf{x})}$. Random variations of the wave velocity in space can be represented as the sum of a background velocity plus some random perturbations $v(\mathbf{x}) = v_0(1+\xi(\mathbf{x}))$.

These random inhomogeneities fluctuate around the background velocity v_0, so that its ensemble average is $\langle v(\mathbf{x})\rangle = v_0$. In the same way the average over the fractional fluctuation of the wave velocity $\xi(\mathbf{x}) = \delta v(\mathbf{x})/v_0$ can be also expressed as $\langle\xi(\mathbf{x})\rangle = 0$. Same as the wave velocity $v(\mathbf{x})$, the spatial variations of the density can also be described as $\rho(\mathbf{x}) = \rho_0(1+\nu\xi(\mathbf{x}))$. ν is a parameter correlating density and velocity fluctuations and it is known as the Birch coefficient (Sato et al., 2012). Experimental data have shown that the seismic wave velocity can roughly increase linearly with mass density for several type of rocks (Birch (1960);Birch (1961)). Similarly, in the earth's crust, this correlation is also validated by borehole observations (e.g. Shiomi et al., 1997). Random media can be characterized by auto-correlation functions (ACF) of the velocity fluctuations, which generally, are defined as:

$$R(\mathbf{x}) \equiv < \xi(\mathbf{y})\xi(\mathbf{y}+\mathbf{x}) > \tag{3.2}$$

The above expression is valid when the randomness is stationary, in which the ensemble average will only depend on $\mathbf{x}$. $R(\mathbf{x})$ gives a measure of the spatial scale and the magnitude of the random heterogeneities in the medium. The level of perturbation is defined by the mean square fluctuation $\epsilon^2 = R(0)$ and the spatial variations of the randomness are mainly characterized by the correlation distance a. These two parameters are the key factors to describe the statistical properties of random media.

It is often convenient to define the ACF in the wavenumber (k) domain. By calculating the Fourier transform we can obtain the PSDF of the ACF as:

$$P(k) = \int\int\int_{\infty}^{-\infty} R(\mathbf{x})e^{-ik\mathbf{x}}d\mathbf{x} \tag{3.3}$$

Since the description of small-scale inhomogeneities is stochastic, for a given PSDF several realizations of the random media must be considered in numerical approaches. In this way, by using $\sqrt{P(k)}$ we can define the amplitude spectrum, then the fluctuations in space can be synthetized by the inverse fourier transform as:

$$\xi(\mathbf{x}) = \frac{1}{(2\pi)^3}\int\int\int_{\infty}^{-\infty} \sqrt{P(k)}e^{i\phi(k)}e^{ik\mathbf{x}}dk \tag{3.4}$$

Where $\phi(k)$ is the phase and it is chosen to change randomly between 0 and 2π. This last property enables us to generate several realizations of inhomogeneous media with random phase for the same level of fluctuation and correlation distance. Diverse type of autocorrelation functions have been used in seismology to describe the random inhomogeneities, among them: exponential, Gaussian and von Kármán. The latter being a generalized version of the gaussian medium. The autocorrelation function of a 2D von Kármán medium is given by the following expression (for

cases 1D and 3D we refer the readr to Sato et al. (2012)):

$$R(\mathbf{r}) = \frac{1}{2^{H-1}\Gamma(H)}\left(\frac{r}{a}\right)^{H} K_H\left(\frac{r}{a}\right), \tag{3.5}$$

Where $\mathbf{r}$ is the lag distance, $r = |\mathbf{r}|$. In Eq. (3.5), a is the correlation length of the fluctuations (closely related to the size of the scatterers), H corresponds to the Hurst exponent, $\Gamma(H)$ is the Gamma function and K_H is the modified Bessel Function of order H. By calculating the Fourier transform of $R(\mathbf{r})$ we can obtain the so know 2D spectrum of heterogeneities:

$$P(k) = \frac{4\pi\Gamma(H+1)\varepsilon^2 a^2}{\Gamma(H)(1+a^2k^2)^{H+1}}. \tag{3.6}$$

In Fig. 3.3 we show a set of von Kármán spectra for different Hurst exponents and a fixed correlation length $a = 0.5$ km. Note that H is the parameter controlling the decay of the level of fluctuations at high wavenumbers.

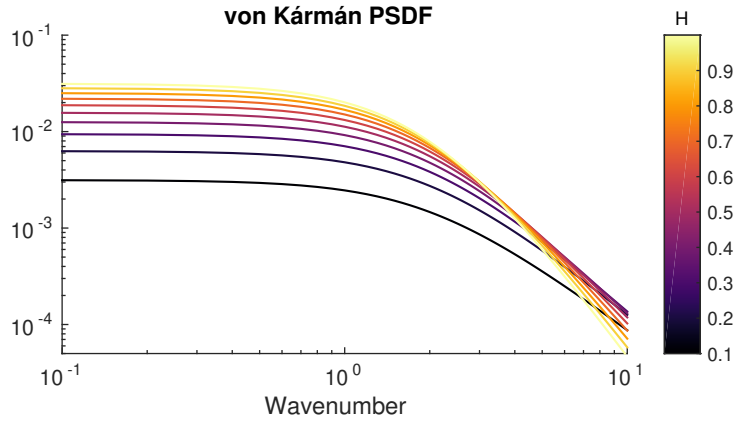

Figure 3.3: PSDF of the von Kármán function for different values of H. Note that for $H = 0.5$ the auto-correlation function becomes exponential

In the isotropic case, the shape of P is fully controlled by $|\mathbf{k}|$. At length scales $2\pi/k$ smaller than the correlation length ($\lambda << a$), spectrum (3.6) follows a power law behavior. Such behavior is strongly supported by field and laboratory measurements of rock velocities and densities (see Sato (2019)). Since heterogeneities in the earth exist at all length scales, accounting for them in seismology represents a challenge for both, forward and inverse problems. In this way, the shortest scales of heterogeneities might often be much smaller than the minimum wavelengths that numerical simulations can represent. In the practice, numerical simulations often require the artificial incorporation of a cut-off wavenumber k_c after which the spectrum of heterogeneities is assumed to be 0 (i.e. $P(k) = 0$ for $k \geq k_c$). Note that his parameter can have an effect on the amount of scattering that numerical simulations can reproduce. The choice of parameter k_c will be discussed in Section. 3.2.3.

The most general way to quantify the scattering strength of a medium with random inhomegeneities, is through the total scattering coefficient g_0. Besides absorption, this parameter can control the shape and amplitudes of coda waves. g_0 is often expressed as inversely proportional to the mean free path ℓ which is the parameter that controls the scattering attenuation and it is defined as the typical length after which the coherent wave (ensemble average of the wavefield) has been significantly attenuated. Thus, at given frequency, the amplitude decay with distance, of plane wave can be expressed as $e^{-g_0 x}$. To quantify the scattering attenuation, in this work we

make use of the coherent wavefield obtained as the ensemble average over several realizations, and the meanfield theory. The latter will be introduced in the next section.

3.2.2 Mean field theory

As it was mentioned in section 3.2.1 attenuation of ballistic waves is one of the most prominent signatures of scattering. Diverse approaches have been used to measure scattering attenuation (eg Sato, 1982; Wu, 1982). (Shapiro and Kneib, 1993) discussed how different representations of the wavefield can reproduce different estimates of this parameters. When travel distance and frequency increase multiple scattering dominates over single scattering which causes that near the apparent ballistic part random components of the wavefield contribute strongly. This poses a difficulty to measure attenuation directly from the initial waveforms as early parts of the records are not purely composed by direct waves. This makes necessary the implementation of statistical approaches to measure scattering attenuation. A first statistical moment corresponds to the mean wavefield, which allows to extract the coherent wavefield. The latter is defined as the portion of the wavefield that resist the averaging procedure and keeps the memory of propagation direction. A direct measurement of the decay of this parameter gives the scattering attenuation. In this way, the whole wavefield can be written as the combination of coherent and non-coherent parts:

$$u = \langle u \rangle + u' \tag{3.7}$$

Where $\langle u \rangle$ is the mean wavefield (coherent wave), which theoretically is obtained as the ensemble average over several realizations of the random media and u' denotes the fluctuations around $\langle u \rangle$, such that $\langle u' \rangle = 0$. The coherent wave decays exponentially over a length scale known as the scattering mean free path ℓ, which is the central quantity of transport theory since it also represents the average distance between two scattering events. The attenuation of the coherent wave can be predicted by the solution of the Dyson equation (Frisch (1968); Rytov et al. (1989)). If the medium is excited by an impulse source, then the generated wavefield can be expressed in terms of the Green's function. Thus, the Dyson's equation in the frequency and wavenumber domain can be written as:

$$G(\omega, \mathbf{k}) = \frac{(2\pi)^3}{k_0^2 - k^2 - (2\pi)^{-3}\Sigma(\omega, \mathbf{k})} \tag{3.8}$$

Where k_0 is the wavenumber of the background medium, and Σ is the so-called 'Mass operator' or self-energy which represents all the possible scattering paths in the random medium. The exact solution of Eq. 3.8 requires the perturbation level ε to be of low order. In that case, the 'self-energy' term is given by (Frisch (1968)):

$$\Sigma(\omega, \mathbf{k}) = \frac{k_0^4}{(2\pi)^{-3}} \int G_0(\omega, \mathbf{r}) P(\mathbf{k} - \mathbf{r}) d^3 r \tag{3.9}$$

Where G_0 is the Green's function of the background medium and P represents the spectrum of heterogeneities for a given auto-correlation function. Eq. 3.9 is known as the first-order smoothing approximation. The physical interpretation states that waves can interact with a random number of inhomogeneities, as soon as they are different. This avoids the recurrent scattering, which is valid for small levels of perturbations (Margerin (2006)).

An additional simplification to the problem might be achieved by assuming that the wavenumber inside each inhomogeneity does not differ that much from k_0. This simplification is known as

the Born approximation (Weaver (1990)). Thus, the effective wavenumber k_e of the medium can be obtained as:

$$k_e(\omega, \hat{\mathbf{k}}) = k_0 - \frac{1}{16\pi^3 k_0} Re\{\Sigma(\omega, k_0\hat{\mathbf{k}})\} - i\frac{1}{16\pi^3 k_0} Im\{\Sigma(\omega, k_0\hat{\mathbf{k}})\} \tag{3.10}$$

Where the imaginary part of k_e suggests that the mean Green's function (coherent wave) experiences some amplitude decay with distance. Such attenuation is not related to the absorption but it is rather a transfer of energy from coherent to incoherent wavefields. The real part of Eq. 3.10 can be used to obtain the phase velocity due to scattering. As mentioned above, the amplitude decay of the coherent wave is controlled by the scattering mean free path. In what follows we will show the expressions we used to calculate ℓ for the 2D case of the SH wave in a von Kármán medium.

Sato (1984) showed that the scattering attenuation can be approximately evaluated by using the Born approximation in the calculation of the scattered energy of a plane wave incident to a localized inhomogeneous region of dimension L, surrounded by a homogeneous background medium having constant ρ_0 and v_0. The typical scale length of the inhomogeneities a (correlation length) should be considerably smaller than L, so that a large number of scatterers compose the inhomogeneous region. To make valid the applicability of the Born approximation, we assume that the magnitude of the inhomogeneities is much smaller than those from the unperturbed medium ($\delta\rho/\rho_0$, $\delta v/v_0 << 1$).

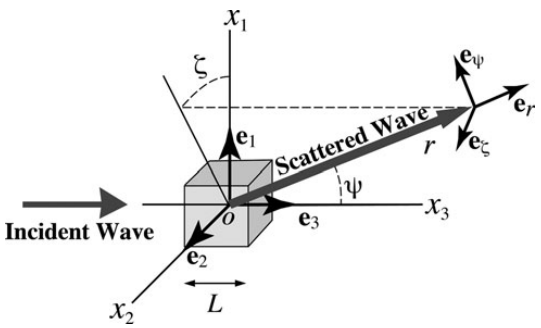

Figure 3.4: Geometry of scattering by a localized inhomogeneity of extent L for the incidence of a plane wave to the x_3-direction, where (r, ϕ, ξ) are spherical coordinates and (e_r, e_ϕ, e_ξ) are unit base vectors. Taken from Sato et al. (2012)

The scattering attenuation (ℓ^{-1}) is then obtained by normalizing the scattered wavefield by the volume of the inhomogeneous region. Note that at very high frequency ($\omega \to \infty$), the Born approximation can predict extremely large levels of scattering which at some point exceeds the scaling conditions of the problem, in such case, ℓ could become close to a in the so-called geometrical optics limit $\omega a/c_0 \gg \sqrt{\langle\varepsilon^2\rangle}$. ℓ^{-1} can be calculated by following the above method.

$$\ell^{-1} = \frac{k_\beta^3}{8\pi}\int_{2\pi}\left[\langle\varepsilon^2_{\rho\rho}\rangle(-1+\hat{\mathbf{k}}\cdot\hat{\mathbf{r}})^2 + 4\langle\varepsilon^2_{\rho\beta}\rangle(-1+\hat{\mathbf{k}}\cdot\hat{\mathbf{r}})\hat{\mathbf{k}}\cdot\hat{\mathbf{r}} + 4\langle\varepsilon^2_{\beta\beta}\rangle(\hat{\mathbf{k}}\cdot\hat{\mathbf{r}})^2\right]P(k_\beta|\hat{\mathbf{r}}-\hat{\mathbf{k}}|)d\hat{r}, \tag{3.11}$$

where $\hat{\mathbf{k}}$ and $\hat{\mathbf{r}}$ are the propagation direction of the incident and scattered wave, respectively. $\langle\varepsilon^2_{\rho\rho}\rangle$, $\langle\varepsilon^2_{\beta\beta}\rangle$ represent the variance of density and velocity fluctuations, and $\langle\varepsilon^2_{\rho\beta}\rangle$ is the covariance between the two. It is worth noting that at a given central frequency ω, the argument of the spectrum P, $(k_\beta|\hat{\mathbf{r}}-\hat{\mathbf{k}}|)$ varies between 0 and $2k_\beta = 2\omega/c_0$. Such condition would imply that,

from the perspective of scattering attenuation, a wave with frequency ω is not sensitive to inhomogeneities with length scales smaller than $\pi c_0/\omega$. This feature is relevant for the full wave propagation modelling since it suggests the frequency limit at which scattering is still well represented.

Making use of Birch's law and assuming random media of von Kármán type, formula (3.11) leads to:

$$\ell^{-1} = \frac{k_\beta^3 a^2 \Gamma(\kappa+1)}{2\Gamma(\kappa)} \int_{2\pi} \frac{(\nu - \cos\theta(2+\nu))^2}{\left(1 + 4k_\beta^2 a^2 \sin^2\frac{\theta}{2}\right)^{\kappa+1}} d\theta, \tag{3.12}$$

Where θ is the scattering angle. The scattering attenuation could be easily solved from Eq. (3.12) by solving numerically the integral. To better illustrate the frequency dependence of ℓ^{-1}, some approximations can be presented separately for the low and high frequency regimes. In the low frequency regime ($k_\beta a \ll 1$), the denominator of the integrand term in (3.12) tends to be 1. That implies that the angular dependence of the integrand term is entirely controlled by the correlation coefficient ν. As in the case of the earth ρ and β are generally, positively correlated, the amount of scattering is expected to be dominant in the backward direction. By solving the integral, Eq. 3.12 becomes:

$$\ell^{-1} \approx \frac{k_\beta^3 a^2 \pi \Gamma(\kappa+1)(4+4\nu+3\nu^2)}{\Gamma(\kappa)} \quad (k_\beta a \to 0). \tag{3.13}$$

Note that the frequency dependence is now cubic, which is representative of the so-called Rayleigh regime. In this case, the wavelengths are considerably larger than the size of the inhomogeneities. The behavior at the intermediate frequency range is known as stochastic regime. The reader might refer to (Yang et al., 2011) to see in more detail. Here we simply recall the approximation in the stochastic regime:

$$\ell^{-1} \approx \frac{2\sqrt{\pi} k_\beta^2 a \Gamma(\kappa+1/2)}{\Gamma(\kappa)} \quad (1 < k_\beta a \ll 1/\sqrt{\langle \varepsilon_{\beta\beta}^2 \rangle}). \tag{3.14}$$

In this way, in the stochastic regime, where the wavelengths are of the order of the length scale of the inhomogeneities, ℓ^{-1} is expected to grow as ω^2. Note that under this approximation scattering attenuation becomes independent on the correlation coefficient ν. However there are correction terms that depend on ν. This last fact will be more clear when we consider applications to different types of random media. In Fig. 3.5 we compare the asymptotic approximations with the exact solution of Eq. 3.11 for a von Kármán medium with correlation length $a = 500$ m, Birch coefficient $\nu = 1$ and standard deviation of the fluctuations 5%

Even though this way to estimate the scattering attenuation should, in theory, be linked with the mean wavefield, in the practice of observational seismology the ensemble averaging procedure is rarely accessible. Even for highly dense arrays, huge assumptions such as statistically uniform scattering are considered. This simplification would pose difficulties for the appropriate measurements of scattering attenuation since the mean wavefield it would not be purely coherent but it would rather be a mix between coherent and incoherent components.

3.2.3 Numerical settings

The numerical modelling of the SH wave propagation in random media was performed by using `specfem2D` code, which applies the Spectral Element Method (Komatitsch and Vilotte (1998), Chaljub et al. (2007)) in space and second order finite difference scheme in time. The

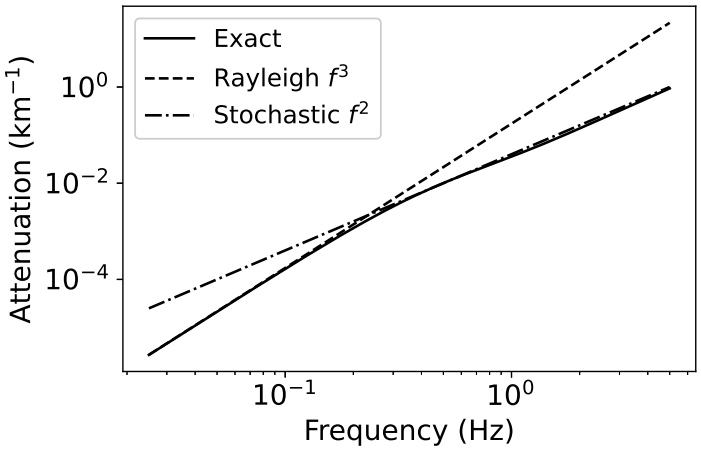

Figure 3.5: Frequency dependence of scattering attenuation: comparing the exact solution (solid) of formula 3.11 with the Rayleigh (dashed) and stochastic approximations (dash-dotted). The example corresponds to a von Kármán medium with $a = 500$ m, $\nu = 1$ and $\varepsilon = 5\%$.

computational domain consists of a square mesh whose size is $L = 314$km with periodic boundary conditions in the laterals and absorbing boundaries in the top and the bottom. The 2D mesh is composed by 10^6 squared elements of size $L_e = 314m$ and a polynomial order N = 4 is used for the spectral element solution of the 2D wave equation. In order to simulate the interaction of the primary waves with the small-scale inhomegeneities we define the random media as the superposition of velocity and density fluctuations in an homogeneous back ground media whose shear wave velocity is $V_0 = 3.14$ km s^{-1}, and with density $\rho_0 = 2500$ kg m^{-3}. Velocity and density fluctuations are correlated as $d\rho/\rho_0 = \nu\, dV/V_0$, where ν is the Birch coefficient for which we define four possible cases: 0.5, 0.67, 0.8, 1. For the description of the small-scale inhomogeneities we used a von Kármán auto-correlation function (ACF) with typical crustal values: correlation length $a = 500$ m, Hurst exponent $\kappa = 0.25$, and standard deviation $\varepsilon = 5\%$ or 10%. The four values of Birch coefficient combined with the two level of fluctuations (ε) gives a total of eight different random media from which we perform different simulations.

Fluctuations are implemented by following the classical spectral approach (see e.g. Sato et al. (2012)): they are initially defined in wavenumber domain, in which the amplitude of the spectrum is given by the square root of the modulus of the ACF and the phase is considered as random and uniformly distributed. We then apply the inverse Fourier transform to the spectrum of heterogeneities in order to represent the fluctuations in the spatial domain. Finally, a cosine taper is applied on the fluctuations along a 5 km thick layer just next to the lateral edges, in order to be consistent with the periodic boundary conditions. Note that since we chose a background velocity with value π and correlation length $a = 0.5$km, the normalized wave number is equal f. It is worth mentioning that ka characterizes the scattering regime.

As it was mentioned in 3.2.2, the appropriate interaction of a given wavelength λ with a random medium requires that heterogeneities with size larger than $\lambda/2$ are well discretized. By assuming a minimum of 5-6 points per wavelength, such requirement could be satisfied. However, as waves can not resolve inhomogeneities with length scales smaller than $\lambda/2$, these have to be eliminated in order to avoid spatial aliasing. In order to avoid this problem we apply a low-pass butterworth filter with four poles and two passes for normalized wave numbers smaller than 10Hz. This procedure is performed directly on the ACF before the inverse Fourier transform.

The criterion outlined above for the discretization parameters suggests that the propagation of SH waves in random media can be accurately simulated for frequencies up to at least 5 Hz. The media are then excited by a plane wave propagating vertically from the bottom to the top. Note that by choosing an incident plane wave as source mechanism, no geometrical spreading can occur, which simplifies our further interpretations of the amplitude decay with distance.

In Fig. 3.6 (left) we show an example of random medium, which has a standard deviation ε of 5% with the von Kármán parameters previously described. For further analyses several realizations of the random media will be considered in order to make an ensemble average of the wavefield. Thus, we perform 60 realizations for each of the eight random media. For each simulation (480 in total) we record the particle velocity at three sets of receivers to which we shall refer as West (W_i), Central (C_i) and East (E_i) with a separation of 50 km, and located at the same vertical position Z_i which means same distance to the source (see Fig. 3.6, right).

To retrieve the coherent wavefield, we considered different averaging procedures: the first one, the ensemble average over the 60 realizations $\langle u \rangle_\phi$; the second one, the space average over a horizontal line of receivers of a single realization $\langle u \rangle_z$, this includes all the nodes of the Gauss-Lobatto-Legendre quadrature (about 5000 points) ; and finally, the ensemble average over 60 realizations of spatially averaged traces, to which we will refer as ensemble-space average $\langle \langle u \rangle_z \rangle_\phi$. By considering that for a realization i, receivers located at W_i, C_i and E_i are statistically independent to each other, we perform the average between these set of receivers. Thus, the ensemble average over 60 realizations would now be equivalent to 180 realizations.

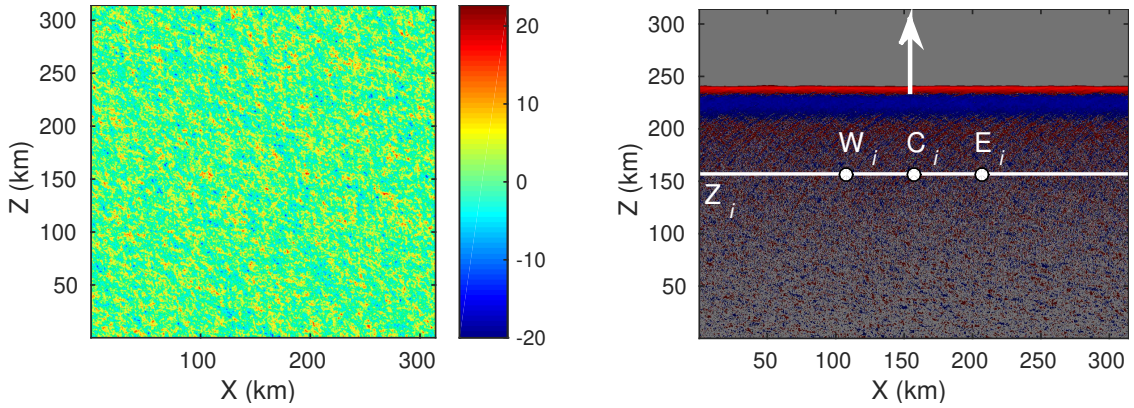

Figure 3.6: Left: 2D fluctuations defined by a von Kármán ACF with correlation length 500 m, Hurst exponent 0.25 and standard deviation 5%. The colorbar indicates the amplitude of the fluctuations in %. Right: snapshot of an up-going plane wave in the random medium with a Birch coefficient $\nu = 1$. Red/blue colors indicate positive/negative particle velocity. At a given propagation distance Z_i, 3 receivers are defined: W_i (west), C_i (centre) and E_i (east).

In Fig. 3.7-left we show the source time function. We used a Dirac delta function that was band-pass filtered between 10^{-1} Hz and 8 Hz with Butterworth filters of different orders. Note that our choice of a Dirac-type source time function makes our simulated wavefield rich in high frequency content.

In Fig. 3.8 we show the three different ways to obtain the coherent wavefield: ensemble (black), space (red) and the ensemble-space averages. Additionally, in order to show the effect of averaging on the waveforms we show also a trace corresponding to a single realization (grey line). This example is shown for a receiver located at a distance of 150 km from the source for a random medium with $\nu = 1$ and $\varepsilon = 5\%$. The three coherent wavefield cases show a significant reduction of the late coda components. This effect is more pronounced on the space

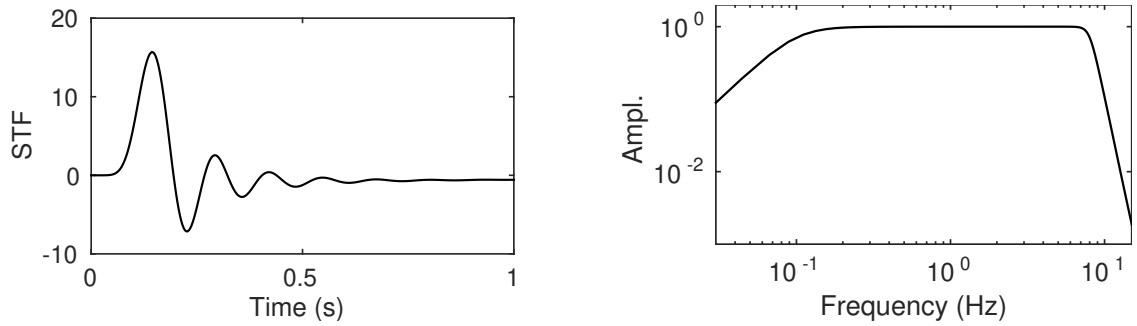

Figure 3.7: Left: source time function (top) with its Fourier amplitude spectrum (bottom) showing energy uniformly distributed between 0.1 Hz and 8 Hz. Right: particle velocity obtained after 150 km of propagation for a single realization of the random medium of Fig. 4.2. The red curve corresponds to a single receiver whereas the black curve corresponds to the spatial average along the horizontal white line of Fig. 4.2.

and ensemble-space averages since a higher number of waveforms were used than in the ensemble average. Fig. 3.8-right shows the corresponding Fourier amplitude spectra of the waveforms shown in Fig. 3.8-left. High frequency components are observed in the one-single realization waveform, whereas these components tend to be reduced on the mean waves. This suggests that non-coherent components become more important at high frequency. In the following subsections we will show how scattering attenuation and velocity dispersion can be measured from the coherent wave. We also discuss the accuracy of our measurements by comparing the numerical results with those obtained from analytical solutions of the Dyson's equation.

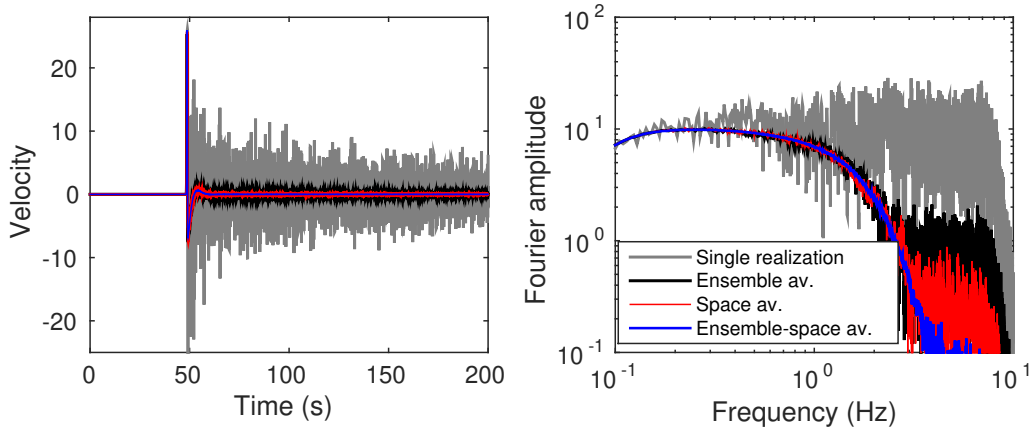

Figure 3.8: Different ways to obtain the coherent wavefield: ensemble average, space average and ensemble-space average. Waveforms and Fourier amplitude spectra are shown in left and right, respectively. Case $\nu = 1$ $\varepsilon = 5\%$ at 150 km from the source

3.3 Scattering attenuation

Scattering attenuation is measured from the amplitude decay of the coherent wavefield with distance. The measurement procedure is illustrated in Fig. 3.9: in Top-left we show a set of waveforms for one single realization, corresponding to the vertical line of receivers located at C_i. These waveforms are then averaged (top-right) for the retrieval of the coherent wavefield

and their Fourier amplitude spectra are computed (bottom-left). Note that since the source is given by a Dirac type function, energy remains almost constant for receivers located at short distances. As distance increases amplitude spectra start being distorted due to scattering. The Fourier amplitudes are also displayed as function of distance (bottom-right) from which we obtain scattering attenuation ℓ^{-1}. This is performed by fitting an exponential decay $\exp(-z/2l)$. As propagation distance increases, measurements of amplitude decreases become less stable due to the strong levels of scattering attenuation specially at high frequencies. That would make necessary to bound the mean free path measurements by distance and frequency. In this case, by visual inspection we use a characteristic amplitude at which the curves start fluctuating. Since we want to evaluate how properly the scattering attenuation is being measured, the effect of the number of realizations on the estimation of ℓ is analyzed. Thus, we compare the estimates of ℓ from the different averaging procedures.

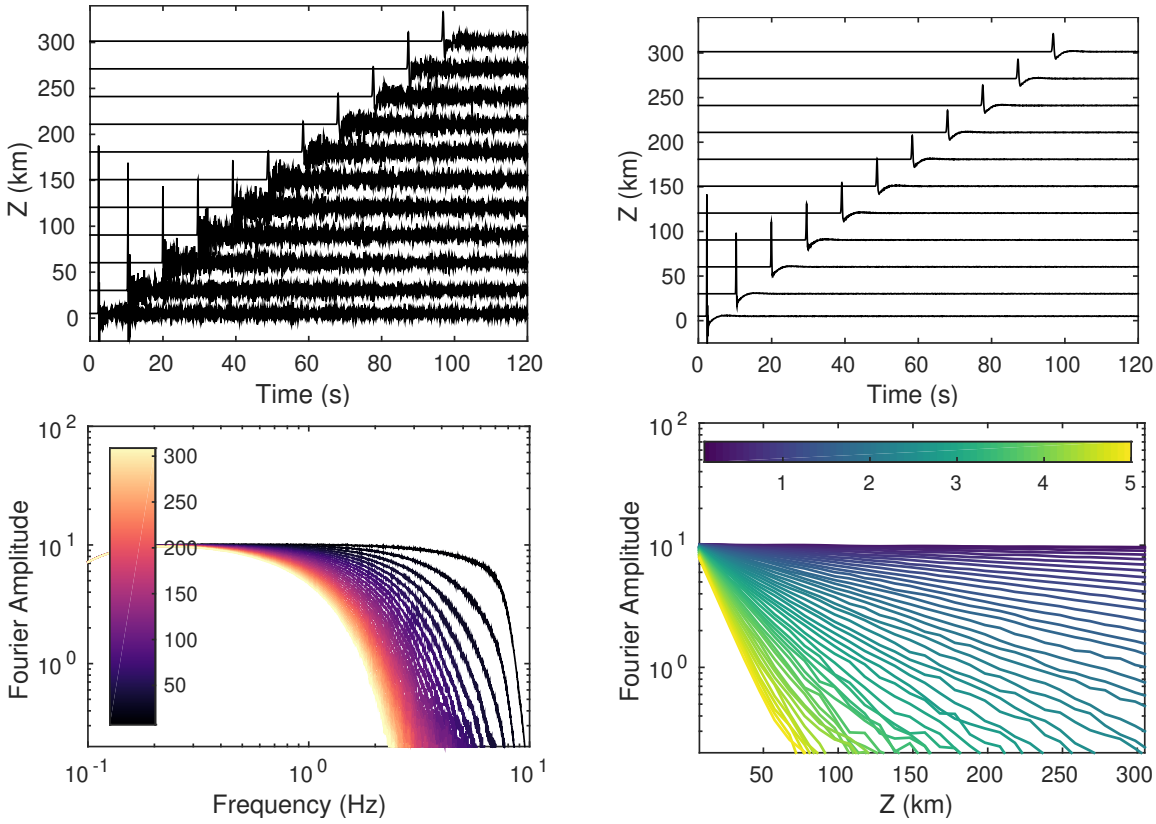

Figure 3.9: Waveforms and Fourier spectra for the case $\nu = 1$ and $\varepsilon = 5\%$. Top: seismic sections of particle velocity for one single realization (left), and for the coherent wavefield obtained by ensemble-space average (right). Bottom: Fourier amplitude spectra of the coherent wavefield as a function of frequency (left) and source-receiver distance (right). Color bars represent the range of propagation distance (in km) and frequency, respectively

In Fig. 3.10 we show estimates of scattering attenuation from the three different types of wavefield average for the two set of cases $\varepsilon = 5\%$ and $\varepsilon = 10\%$. The solid lines represent the measurements obtained from the ensemble average over 180 realizations, the dotted lines correspond to the space average and the dashed lines are those from the ensemble-space average. Results were obtained in the frequency range between 0.1 and 5 Hz with a step of 0.1 Hz. For all the cases, results in the three approaches are pretty similar in the low frequency range (low attenuation). Estimates start to differ as frequency increases, specially for the ensemble average

measurements, presenting some instabilities after 3 Hz (resp. 1 Hz) for all cases $\varepsilon = 5\%$ (resp. $\varepsilon = 10\%$). Interestingly, robust estimates are found for cases $\varepsilon = 5\%$ when using the space average for a single realization. However this averaging procedure exhibits some difficulties at frequencies above 4 (resp. 2) Hz for Birch coefficients below 0.67 (resp. 0.5) when $\varepsilon = 10\%$. As expected, the ensemble-space average measurements present the most stable estimates in most of the correlation coefficient cases, except for $\nu = 0.5$ $\varepsilon = 10\%$. In this case the scattering attenuation starts behaving irregularly after 2.5 Hz. Such behavior might be related to the fact that ℓ becomes shorter than the minimum inter-station distance. A more stable estimate would probably require a denser array of receiver for such a high level of scattering.

A comparison between theoretical and numerical scattering estimates is shown in Fig. 3.11. We used the Ensemble-Space average (referred as SEM) as the numerical reference to be compared with the theoretical calculations. Note that we were able to reproduce the behavior presented in Fig. 3.5. Both scattering regimes can be appreciated: in the low frequency range, scattering attenuation increases as f^3 in the Rayleigh regime; and at higher frequencies, the variations of ℓ^{-1} take the form of f^2. The results show that overall, there is a good agreement between SEM measurements and theoretical calculations for most of the cases. As it was mentioned before, some instabilities are observed in the high frequency range for case $\nu = 0.5$ $\varepsilon = 10\%$, which suggest the impossibility to make attenuation measurements at such strong levels of scattering.

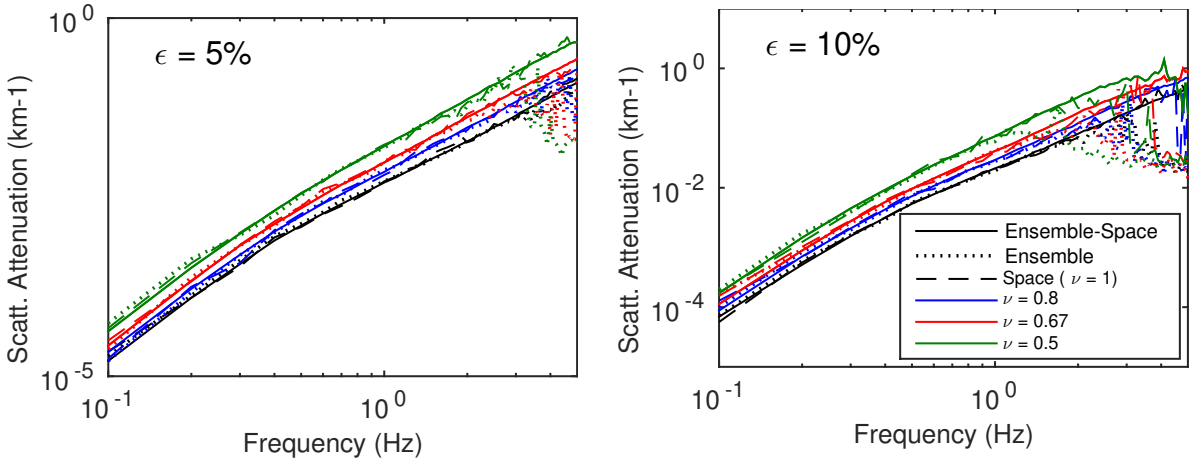

Figure 3.10: Comparison of scattering attenuation estimates obtained with different measures of the coherent wavefield: ensemble average (dotted lines), space average (dashed lines) and ensemble-space Average (solid lines). Left (resp. right) figure corresponds to random media with $\varepsilon = 5\%$ (resp. $\varepsilon = 10\%$).

3.4 Dispersion

By averaging the wavefield over several realizations (or spatial average) we are equivalently transforming a full wavefield from a heterogeneous and lossless medium into that from a homogeneous, 'absorbing' and dispersive medium. In the previous section we studied how by performing this equivalence we are able to retrieve the attenuation of coherent waves. Besides this amplitude decay effect, the travel time of this coherent wave can experience some frequency dependence due to the interaction with the small scale inhomogeneities. These interactions are inherently controlled by the wavelengths and can result into a dispersion velocity. The goal of this section is to measure the emerged phase velocity and to compare it with theoretical estimations.

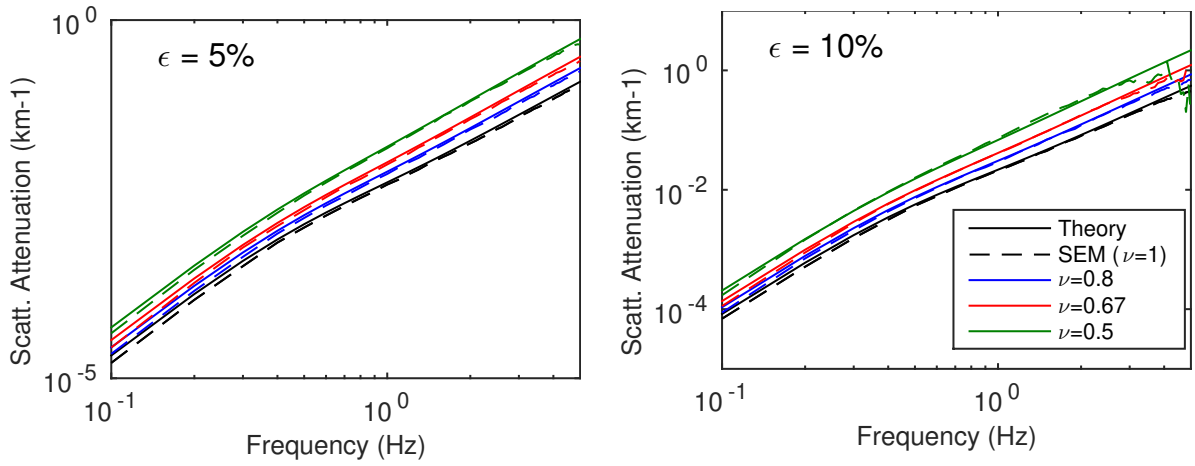

Figure 3.11: Comparison of scattering attenuation between SEM (dashed lines) and the analytical solution (solid lines). SEM solution corresponds to the ensemble-space average approach and the theory is given by the solution of the Eq. 3.12. (Left) Cases $\varepsilon = 5\%$; (Right) Cases $\varepsilon = 10\%$

At a propagation distance z, the Fourier transform of the mean wave $\langle u \rangle$ has the form:

$$\hat{U}(\omega, z) = A(\omega, z)e^{-i\phi(\omega,z)} \tag{3.15}$$

Where the real part $A(\omega, z)$ is the amplitude spectrum, and the imaginary term represents the phase spectrum, with phase ϕ. The phase velocity $c(\omega)$ is then measured from the distance dependence of the phase difference between a given receiver and the source. For a given frequency ω, at a distance z from the source, the phase is given by:

$$\phi(\omega, z) = \frac{\omega}{c(\omega)} z + \phi_0(\omega, z_0) \tag{3.16}$$

Where ϕ_0 and z_0 are the unwrapped phase and the location of the source, respectively. In the practice of seismology, the phase information of the external source is not often accessible. For this reason we re-define the location z_0 as the corresponding to the closest receiver to the source. Thus, relative measurements of the phase are performed with respect to a waveform not significantly attenuated or perturbed. Then, for a given frequency ω, the distance dependence of the phase can be written as:

$$\phi(z) = \frac{\omega}{c}(z - z_0) + \phi(z_0) \tag{3.17}$$

In this way we can measure the phase velocity from the linear system:

$$\frac{\phi(z) - \phi(z_0)}{\omega} = c^{-1}(z - z_0) \tag{3.18}$$

The individual phases $\phi(\omega)$ are computed as the arc-tangent of the ratio between the imaginary and real parts of the Fourier spectrum in Eq. 3.15. This parameter can be displayed as function of the frequency and the propagation distance. In Fig. 3.12(a) and (b) we show an example of individual phases for a von Karman medium with properties $\nu = 1$ and $\varepsilon = 5\%$. Fig. 3.12(a) shows the quasi-linear variations of the phase with distance. Note that, as distance and frequency increase, the phase variations start being distorted. This might be interpreted as the undesired

influence of non-coherent components on the definition of the mean wave. In order to improve the quality of our measurements we bound the range of frequencies and distances by visual inspection. Thus, we select an upper bound of phase after which the corresponding frequencies and propagation distances are excluded.

In Fig. 3.12(c) and (d) we represent the variations of the phase difference, which is given by the left hand term of Eq. 3.18. Same as for individual phases, the normalized phase differences are displayed as function of distance and frequency. Phase velocities are measured by fitting the curves in Fig. 3.12(c) to a linear regression within the distance range previously defined at each frequency. Note that term $(\phi(z) - \phi(z_0))/\omega$ can be interpreted as the time delay at a given frequency ω. Hence, the contour lines in Fig. 3.12(d) denote the variation of time delay for different frequencies. In the absence of dispersion these contour lines would be perfectly vertical, which means that the time delay would be constant along the whole range of frequencies; the white line in Fig. 3.12(d) represents the chosen distance range according to the visual inspection strategy above mentioned. As reference, we also show the scattering mean free path (blue line). It is worth mentioning that due to the relatively low level of scattering of this case, we are able to use inter-station distances much larger than the scattering mean free path. However for cases with stronger levels of scattering, the white line indicating the frequency dependent distance range, becomes closer to the scattering mean free path. This is illustrated in the supplementary material Fig. 3.15.

Measurements of phase velocity (from SEM simulations) for all the von Kármán media are shown in Fig. 3.13(a) and (b) (dashed lines). Overall, the velocity dispersion of the coherent wavefield is not significant. They represent variations ranging from 0.1% to 2% of the background velocity. For most cases $\varepsilon = 5\%$ (Fig. 3.13top-left), measurements are relatively stable. Except for case $\nu = 0.5$, showing some abrupt increases of phase velocity above 3Hz. Measurements are less stable at cases $\varepsilon = 10\%$, presenting huge fluctuations for frequencies above 1 Hz, except for case $\nu = 1$, where the trend of the dispersion curve can still be appreciated up to 4 Hz. The difficulties to perform robust measurements might be related to the significantly distorted the phase information in the von Karman media with the highest scattering strength.

For comparisons purposes we also plot the phase velocity calculations from the mean field theory (solid lines). It is worth mentioning that, unlike calculations of the scattering mean free path, the solution for the phase velocities are not localized for a given wavelength. It rather requires the evaluation of an integral over an infinite number of wavelengths which complicates the direct comparisons with SEM measurements. To circumvent this difficulty, same as with the SEM model, the spectrum of heterogeneities is low-pass filtered with a cut-off frequency of 10 Hz. In Fig. 3.13-(c) and (d) we show the effect of the filtering on the theoretical calculations of the phase velocity. It can be seen that for the normalized wave number we used, not significant variation in the shape of the curves is observed. However, absolute values of phase velocity are significantly scaled after applying the filtering. This is observed as a reduction of the dispersion (curves attempt to get closer to the back ground velocity). The lower values of the phase velocity when the filter is not applied might be originated by the contribution of very short wavelengths (frequencies above 10Hz) in the evaluation of the integral.

Comparisons in Fig. 3.13(a) and (b) evidence some significant differences between SEM and theoretical calculations, in terms of absolute values. At cases 5% there exists a similar frequency dependence between the two approaches , the variations with frequency increase as the correlation coefficient ν decreases (stronger scattering). A similar signature is observed for the set of cases 10%, however, the huge instabilities at high frequencies and short correlation coefficients makes difficult these comparisons.

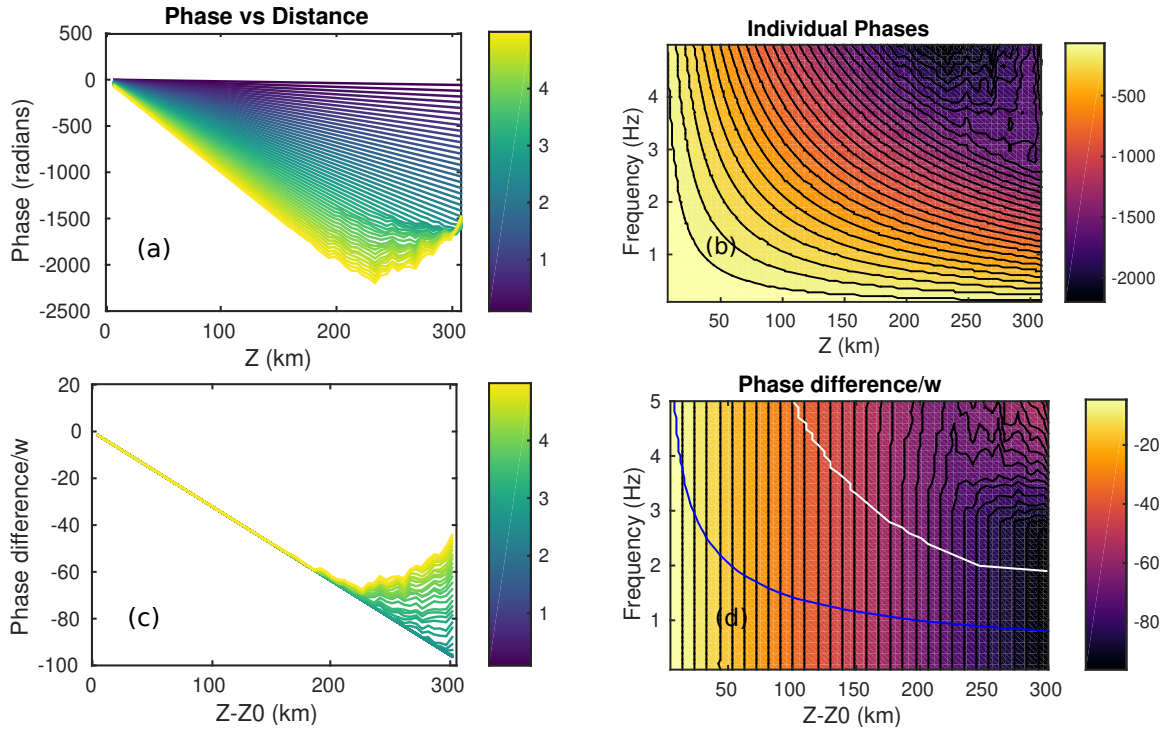

Figure 3.12: (a) Distance and frequency dependence of individual phases for the color bars indicate different values of frequency and (b) its 2D representation, where the colorbar indicates different values of phase; (c) Distance and frequency dependence of individual phases. The horizontal axis represents the relative distance with respect to the first receiver. (d) The 2D representation of phase difference. The white line denotes the range of propagation distances used at each frequency, and blue line is the corresponding scattering mean free path. This example corresponds to the case $\nu = 1$ $\varepsilon = 5\%$

3.5 Conclusion

By analyzing the properties of the coherent wavefield, we studied the propagation of SH waves in 2D random media. Several cases of von Karman media were considered, with different strengths of scattering. Scattering attenuation and phase velocities were measured and compared with their theoretical counterpart. Different averaging procedures were used for the extraction of the coherent wavefield: (i)the ensemble average over 180 realizations, (ii)the horizontal space average and (iii)the ensemble-space average. The latter being the one that allowed to reproduce the most robust estimates of scattering attenuation. Difficulties with the ensemble average procedure were related to insufficient number of realization to retrieve a cleaner coherent wave. Estimates from the horizontal space average showed, in general, very stable estimates of scattering attenuation except for some von Kármán media with the highest scattering strength and at high frequency. However the good quality of this averaging procedure confirms the feasibility of spatially averaged waveforms since it's computationally less expensive. Comparisons between the different averaging procedures from both scattering attenuation below 2.5 Hz, as well as the waveforms and the Fourier amplitude spectra of the coherent wave, showed that very similar estimates and mean wave can be retrieved from different concepts of mean wave. This last observation validates the ergodicity hypothesis as the ensemble average over several realizations of the random media is equivalent to the horizontal space average over several waveforms located at the same distance to the source.

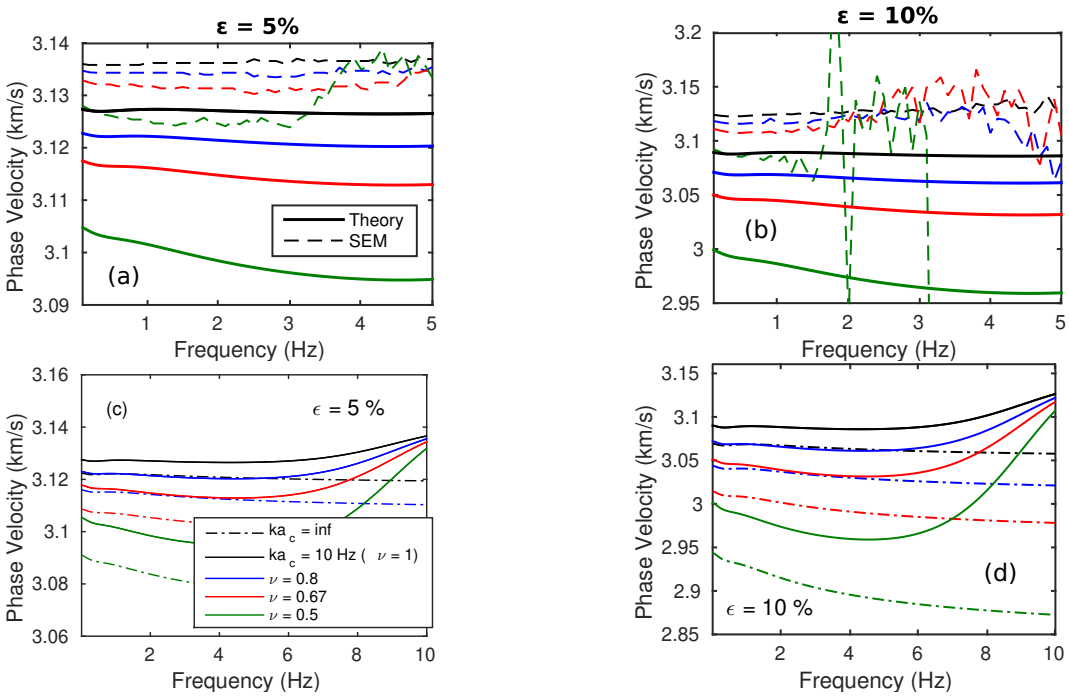

Figure 3.13: Phase velocities. (a) and (b) Comparisons between measurements from full-wavefield simulations (dashed lines) and meanfield theory (solid lines); (c) and (d) Effect of the low-pass filter on the heterogeneities on the theoretical calculations of the phase velocity

Comparisons of scattering attenuation, measured from SEM simulations with those from the Dyson's equation evidenced the robustness of our numerical simulations as well as the adequacy of the proposed verification procedure. Estimates had excellent agreement with theoretical predictions except for the extremely high levels of scattering. Particularly at high frequency, SEM estimates showed some instabilities when the scattering mean free path is shorter than the minimum inter-station distance. That might suggest the use of a denser array of receivers when scattering is that strong.

Phase velocities were measured from the distance dependence of the phase differences. Measurements at cases with the highest perturbation levels showed some difficulties to obtain stable estimates, specially above 1 Hz. Comparisons with the solution of the Dyson's equation showed significant differences of absolute values in all the cases. However, we were able to reproduce a similar frequency dependence. We attribute the substantial differences between synthetics and theory to the contribution of small-scales ($ka > 5$ Hz) on the theoretical calculations in the frequency range of interest. Although this is what physically should be reproduced, our numerical simulations do not consider length scales ka smaller than $10Hz$. Such discrepancy would systematically complicate the comparisons in terms of phase velocity, and it would require an homogenization technique that takes into account the effect of small-scales on the large wavelengths estimates of phase velocity.

3.6 supplementary material

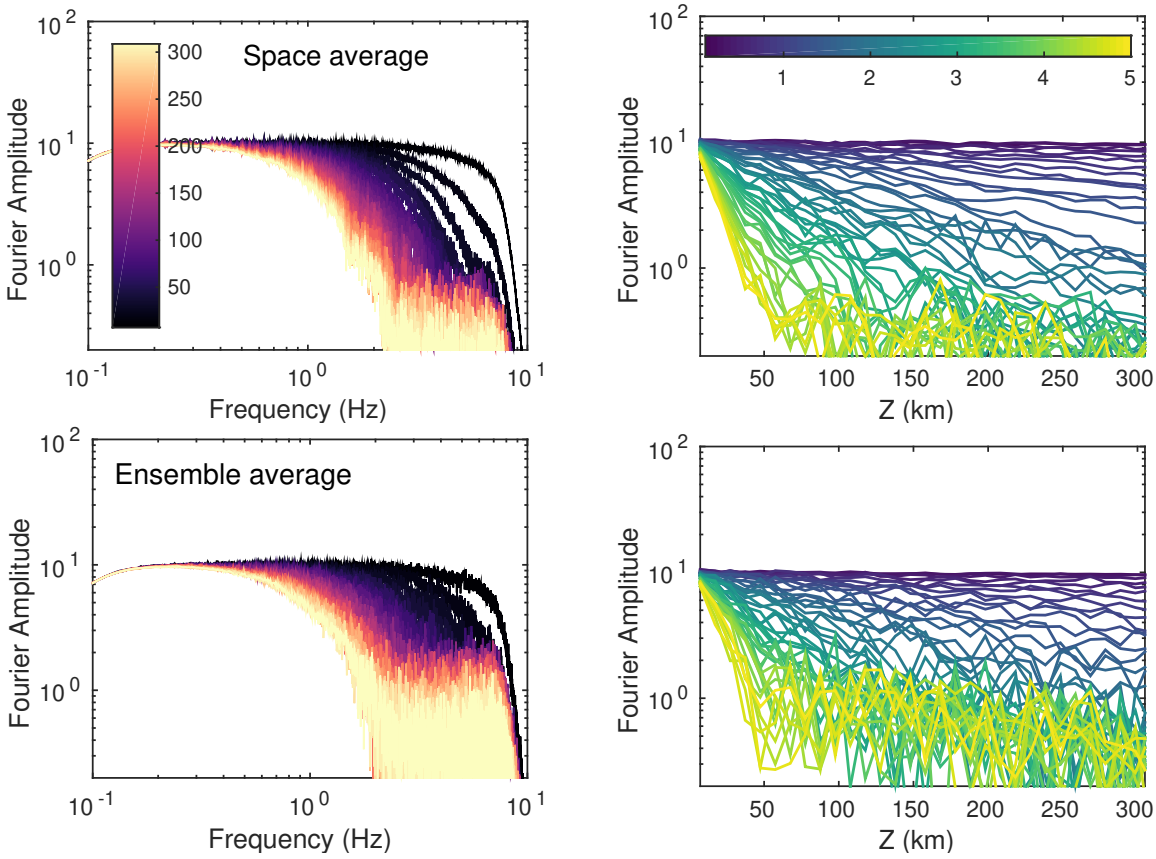

Figure 3.14: Fourier amplitude spectra as a function of frequency (left) and source-receiver distance (right) for the case $\nu = 1$ and $\varepsilon = 5\%$. Mean wavefield is estimated either by using the space average (top) or the ensemble average (bottom). Color bars represent the range of propagation distance and frequency, respectively

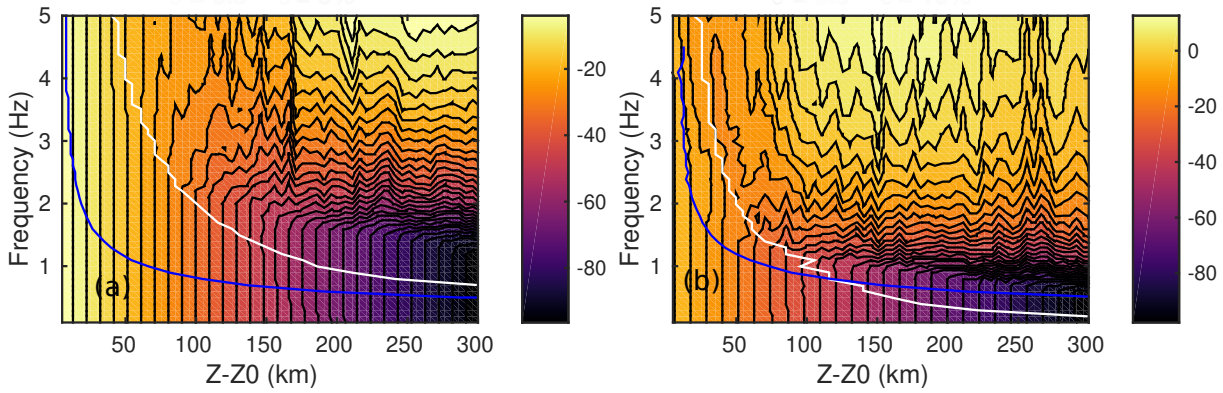

Figure 3.15: Frequency and distance dependence of the phase difference. The white line denotes the range of propagation distances used at each frequency, and blue line is the corresponding scattering mean free path. Cases $\nu = 0.5$ (a) $\varepsilon = 5\%$ and (b) $\varepsilon = 10\%$

Chapter 4

Energy transport in 2D random media: from ballistic to diffusive behavior

We present a comprehensive analysis of the energy transport of SH waves in 2D random media, covering a broad range of propagation regimes from ballistic to diffusive. In this work we use the same von Kármán media as the one presented in chapter 3: Hurst coefficient of 0.25 and a correlation length a=500 m. The correlation coefficient has 4 possible values between 0.5 and 1, and the perturbation level is either 5% or 10%. As quantity representing the wavefield we use the mean intensities from SEM simulations which are then compared with Monte-carlo solutions of the radiative transfer theory (RTT). Comparisons show excellent agreement between SEM intensities and the theoretical predictions. The numerical analyses evidence the difference of attenuation length between the coherent wave (mean field) and the mean intensity. Whereas the amplitude decay with distance of the coherent wave is controlled by the scattering mean free path, the peak of the mean intensities seems to be controlled by the transport mean free path. Additionally, we perform statistical analyses on the fluctuations of the ballistic peak which exhibits a transition from log-normal to exponential distribution. These two types of distribution characterize the ballistic and diffusive behaviors, respectively, which means that after certain propagation distances the quasi-ballistic peak is composed mainly by multiply-diffused components. Such critical distance is of the order of the scattering mean free path and offers an alternative method to measure this parameter.

Keywords: mean intensities, ballistic peak, quasi-ballistic peak, diffusive behavior, transport mean free path.

4.1 Introduction

As travel distance increases, the coherent wavefield might become significantly attenuated and contaminated by multiply diffused components, which can destroy the phase information. This makes difficult to study the propagation characteristics of seismic waves in random media at further scattering regimes. The second statistical moment of the wavefield is the average energy and it can hold a wider information about different propagation regimes. Thus, energy envelopes are used to study the attenuation properties of highly heterogeneous media. Diverse models have been proposed to study the transport of energy in scattering media, among them, the Radiative transfer theory (RTT) (Wu (1985); Margerin et al. (1998)) and the diffusion approximation (Dainty et al. (1974); Wegler and Lühr (2001)). Radiative transfer was initially developed in the field of astrophysics to describe the transport of light energy in the atmosphere (Chandrasekhar (1960)). This was later introduced in seismology by Wu (1985) for the separation of scattering and intrinsic attenuation. It is worth noting that RTT discards the phase information of each individual wave, and it rather focuses on the transport of the ensemble of energy. By assuming infinite space, Weaver (1990) and Ryzhik et al. (1996) derived transport equations for elastic waves from the equation of motion. Despite its apparent facility to be extrapolated to different fields, solutions of RTT are regarded as considerably difficult. Very few analytical solutions have been proposed under the assumption of isotropic scattering with the dominance, either of body or surface waves (Sato (1993); Paasschens (1997)). With the advent of computational resources, Monte-Carlo (MC) simulations emerges as an efficient solution of more complicated problems such as, the anisotropic scattering or the coupling between surface and body waves (Tregoures and Van Tiggelen, 2002; Margerin et al., 2019; Xu et al., 2022; de Hoop et al., 2022).

Retrieving scattering and absorption properties of the earth crust and volcanic environments have been possible by comparing observed energy envelopes with those from RTT simulations (Fehler et al. (1992); Hoshiba (1993); Carcole and Sato (2010); Ugalde et al. (2010); Eulenfeld and Wegler (2016)). A current frontier in the application of RTT solutions for the estimation of attenuation mechanisms concerns the use of noise-based techniques (Hirose et al. (2019); van Dinther et al. (2020); Hirose et al. (2022)). Either from earthquake, active sources or noise correlated signals, many of the RTT schemes for the inversion of attenuation properties rely on the assumption of isotropic scattering. In such hypothesis the transport of energy is simulated such that scattering events do not have a preferred direction. A further development in RTT would treat the scattering phenomenon as anisotropic (Margerin et al. (1998); Sens-Schönfelder et al. (2009); Gaebler et al. (2015)). This allows the distinction of two length scales known as scattering and transport mean free paths. The former controls the attenuation of the coherent wave and the latter is the typical length after which diffusion regime emerges. By comparing estimates from real data under the isotropic and anisotropic assumptions, Gaebler et al. (2015) showed that the transport mean free path is the key parameter controlling the scattering attenuation of energy envelopes.

In the context of ground motion simulations, diverse works have analyzed the effects of small-scale inhomogeneities (e.g. Imperatori and Mai (2012);Takemura et al. (2015);Hu et al. (2022)). However, most of these works remain difficult to interpret due to the lack of a precise description of the propagation regimes they simulate. As mentioned before, the spatio-temporal evolution of mean intensities offer the possibility to observe the interaction of these regimes. In this work, we present a comprehensive analysis of the energy transport of SH waves in 2D random media from ab-initio numerical simulations and RTT. Simulated full-waveforms were computed by using the spectral element method (SEM) and they were introduced in the previous chapter. The wide range of von Kármán, propagation distances and frequency bands allows to study diverse

propagation regimes from ballistic to diffusive behaviors. We perform some comparisons between SEM energy envelopes and RTT similar to previous works (Wegler et al. (2006); Przybilla et al. (2006); Przybilla and Korn (2008); Emoto and Sato (2018)). We pay particular attention on the space evolution of the so-called 'ballistic' peak. Thus, we perform some statistical analyses on the fluctuations of the 'ballistic' peak as an indicator of the propagation regime. Finally we study the attenuation of the ballistic peak with distance, which is a relevant parameter in the context of seismic risk assessment.

The organisation of the manuscript is as follows: in Section. 4.2 we present some useful concepts on the radiative transfer theory and diffusion approximation; Analyses on SEM energy envelopes, as well as the comparisons with RTT are presented in Section. 4.3. In Section. 4.4 we introduce the statistical analyses on the fluctuations of the ballistic peak, whose decay with distance is studied in Section. 4.5. Finally, in Section. 4.6 we present some conclusions.

4.2 Transport theory

The radiative transfer theory predicts the transport of average energy density in media whose elastic parameters have random fluctuations. Transport equations are derived from the wave equation by considering the Wigner transformation of Green's function in the inhomogeneous medium. For a deeper treatment of the RT equations, we refer the reader to the works of Weaver (1990) and Ryzhik et al. (1996). In the present work, we simply recall the form of the transport equation as:

$$\left(\frac{\partial}{\partial t} + c\hat{\mathbf{k}}\cdot\nabla_{\mathbf{r}}\right) e(t,\mathbf{r},\hat{\mathbf{k}}) = -\tau^{-1}e(t,\mathbf{r},\hat{\mathbf{k}}) + \tau^{-1}\oint p(\hat{\mathbf{k}},\hat{\mathbf{k}}')e(t,\mathbf{r},\hat{\mathbf{k}}')d\hat{k}' + S(t,\mathbf{r},\hat{\mathbf{k}}), \qquad (4.1)$$

where c is the wave velocity, $\hat{\mathbf{k}}$, the propagation direction, τ, is the scattering mean free time, which is related to ℓ as $\tau = \ell/c$. $e(\mathbf{r},\hat{\mathbf{k}},t)$ is the specific energy density at position $\mathbf{r}$ and time t, $\oint d\hat{k}'$, an integral over all propagation directions. $p(\hat{\mathbf{k}},\hat{\mathbf{k}}')$ is the phase function and it represents the probability that a wave with direction $\hat{\mathbf{k}}'$ is deflected into direction $\hat{\mathbf{k}}$, and $S(\mathbf{r},\hat{\mathbf{k}},t)$ is the energy source term. The physical interpretation of the transport equation terms (except for the source) can be illustrated in 4.1, where the left hand terms correspond to the incident and transmitted energy into a scattering section, which results (right hand) into a loss of energy (redistribution) and a "probable" gain that is given by the random walks that could be deflected into direction $\hat{\mathbf{k}}$.

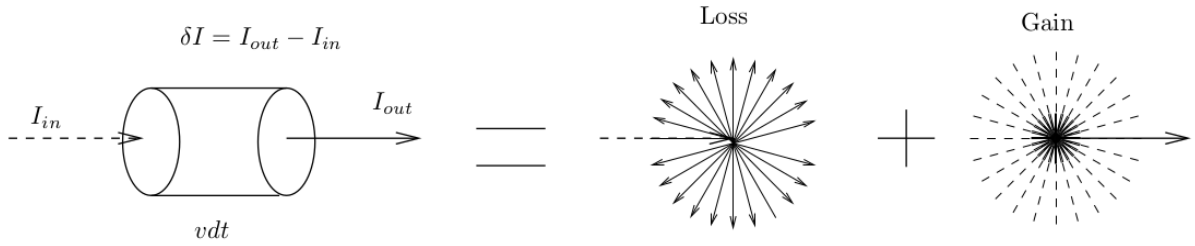

Figure 4.1: Different terms of the transport equation. E_{in} is the incoming energy into an elementary cylindrical volume with length vdt, and E_{out} is the outgoing energy after interacting with the volume. Two factors contribute to the sign of the intensity variation δE: energy losses (first term of the right hand-side) or gains (second term of the right hand-side) by scattering. Taken from Margerin (2005)

The specific energy density is proportional to the amount of energy propagating in direction $\hat{\mathbf{k}}$ per unit volume and is related to the wavefield u by a Wigner-Ville transform:

$$e(t,\mathbf{r},\hat{\mathbf{k}}) = C\int\int\langle u(t-\theta/2,\mathbf{r}-\mathbf{x}/2)u(t+\theta/2,\mathbf{r}+\mathbf{x}/2)\rangle e^{i\omega\theta-i\omega\hat{\mathbf{k}}\cdot\mathbf{x}/c}d\theta d^2x \tag{4.2}$$

Here C is a normalization factor that depends on the type of wave. Eq (4.2) defines the specific energy density as the power spectral density function of the wavefield at time t, position $\mathbf{r}$ and frequency ω. Note that the wavefield u was filtered in a narrow frequency band, in which we have assumed that variations of energy in the Wigner-Ville distribution are not that important. As the scattering mean free time depends strongly on the frequency, loss and gain terms in right hand side of Eq. 4.1 also have a significant frequency dependence. This last point is the key for transport equation as it controls different scattering regimes.

Solutions of the transport equation are in general considered as difficult for the most realistic cases. Analytical solutions are often found in literature under some simplifications such as, isotropic scattering, either body or surface waves dominance, etc. (Wu (1985); Sato (1994); Paasschens (1997)). Numerical methods offer an interesting approximated solutions for the transport equation. In this work we use one of the most popular techniques, the Monte-Carlo method (MC), in which the propagation of energy is described as a model for random walks of a huge number of particles. In this method diverse realistic scenarios can be incorporated such as anisotropic scattering and mode conversion.

At sufficiently long lapse times, multiple scattering tend to uniformize the angular dependence of energy density. Under these circumstances the direction of the wave propagation becomes predominantly random as several scattering events redistribute the energy in all angles. This propagation regime is known as multiple diffusion and it can lead to an interesting approximation of the RTE, which is know as diffusion approximation (e.g. Kourganoff, 1969; Weaver, 1990)

$$\frac{\partial e(t,\mathbf{r})}{\partial t} - D\nabla^2 e(t,\mathbf{r}) = S(t,\mathbf{r}) \tag{4.3}$$

where the diffusion constant in 2-D is defined as: $D = c\ell^*/2$. The formula for the diffusivity of seismic waves features the transport mean free path ℓ^* as a new length scale:

$$(\ell^*)^{-1} = \frac{k_\beta^3\langle\varepsilon_{\beta\beta}^2\rangle}{8\pi}\int_{2\pi}(\nu-\hat{\mathbf{k}}\cdot\hat{\mathbf{r}}(2+\nu))^2\Phi(k_\beta|\hat{\mathbf{r}}-\hat{\mathbf{k}}|)(1-\hat{\mathbf{k}}\cdot\hat{\mathbf{r}})d\hat{r} \tag{4.4}$$

The relation between the transport and the scattering mean free paths is given by $\ell^* = \ell/(1-Cos\theta)$. The transport mean free path ℓ^* is physically interpreted as the typical length of propagation after which an incident wavefield is randomized. In this regime the wavefront loses significantly the memory of its initial propagation direction. Note that the ratio between ℓ^* and ℓ is controlled by different scattering regimes. For example, when backscattering is dominant the transport mean free path is slightly smaller than the scattering mean free path. In the other hand, in the forward scattering regime ℓ^* is absolutely larger than ℓ. For cases of isotropic scattering ℓ^* and ℓ are the same. The role of these two propagation lengths on the amplitude of the wavefield will be more deeply discussed in sec. 4.5.

4.3 Energy envelope analyses

In this work we exploit the scattering properties of 2D random media by using the energy envelopes of propagating SH waves. The synthetic waveforms were obtained from the 2D numerical simulations of the SH waves of eight von Kármán media. The source is given by a Dirac-type plane wave propagating vertically, from the bottom to the top (see Fig.4.2-top). Analyses on the energy envelopes from SEM and RTT approaches are performed at three frequency bands ($[0.5, 1]$ Hz, $[1, 2]$ Hz and $[2, 4]$ Hz). In order to observe different propagation regimes, we choose three epicentral distances ($\{50, 100, 150\}$ km). The von Kármán media consist of Birch correlation coefficients ($\{0.5, 0.67, 0.8, 1\}$), RMS velocity perturbations ($\{0.05, 0.1\}$) and The Hurst exponent is fixed at 0.25. At each single realization waveforms are filtered in three frequency bands 0.5-1, 1-2 and 2-4 Hz. The energy envelopes of the filtered waveforms are calculated as:

$$\langle |u(t)|^2 \rangle = \langle u^r(t)^2 + u^i(t)^2 \rangle \tag{4.5}$$

Where $u^r(t)$ is the observed wavefield having $u^i(t)$ as its Hilbert transform. Mean SEM intensities are then obtained as the ensemble average over 180 realizations $\langle |u(t)|^2 \rangle_\phi$ (60 realizations and three independent receivers $W_i, C_i E_i$, see chapter 3). In Fig.4.2-bottom an example of energy envelopes for the case $\nu = 1$ $\varepsilon = 5\%$ with propagation distances $\{50, 100, 150\}$ km. Note that different propagation regimes emerge, from the apparent dominance of ballistic components at low frequency, to the predominant coda at long propagation distances in the high frequency. In sections 4.3.2 and 4.4 we will explain this transition in more detail.

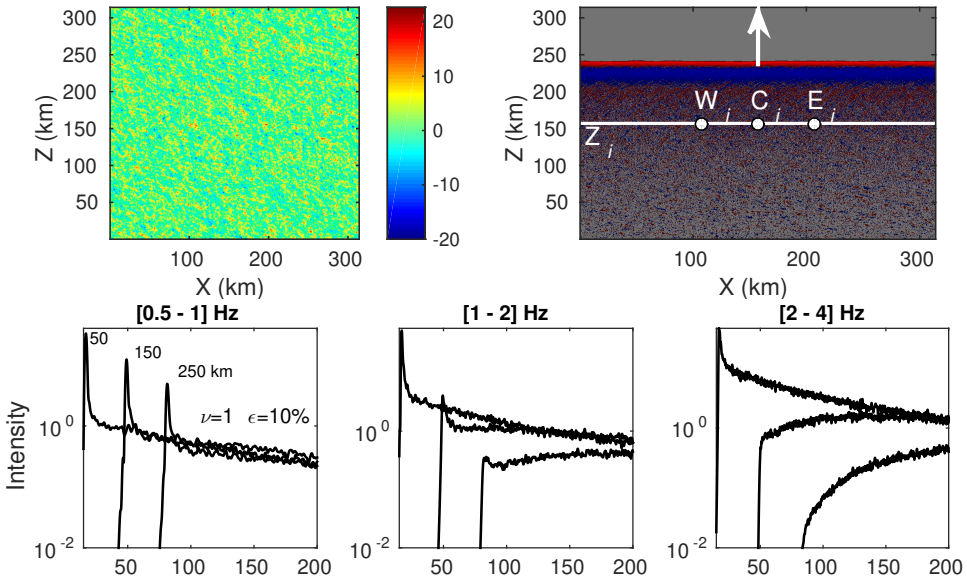

Figure 4.2: (Top) Left: 2D fluctuations defined by a von Kármán ACF with correlation length 500 m, Hurst exponent 0.25 and standard deviation 5%. The colorbar indicates the amplitude of the fluctuations in %. Right: snapshot of an up-going plane wave in the random medium with a Birch coefficient $\nu = 1$. Red/blue colors indicate positive/negative particle velocity. At a given propagation distance Z_i, 3 receivers are defined: W_i (west), C_i (centre) and E_i (east). (Bottom) Example of energy envelopes at three frequency bands and for three epicentral distances. Envelopes are obtained for case $\nu = 1$ $\varepsilon = 10\%$

4.3.1 Temporal source term in RTT

In this section we show our strategy to compare mean intensities derived from RTT and SEM full wave simulations (SEM intensities). Note that RTT predicts energy envelopes of waves propagating in a random medium at a given frequency (Ryzhik et al., 1996). Unlike the wave equation, RTT uses quantities that depend quadratically on the wavefield. In the practice of seismology, the energy envelopes are often defined by using the square and the Hilbert transform of the seismogram, as shown in Eq. 4.5. The observed wavefield $u^r(t)$ can be expressed as the convolution between the Green's function (impulse response) $G(t)$ and a source term (applied force) $f(t)$

$$u^r(t) = G(t) \otimes f(t) \tag{4.6}$$

Where $f(t)$ is the source time function. Since the propagation phenomenon is predominantly frequency dependent, observations must be localized at the frequencies of interest. This makes necessary to filter seismograms previous to compute their energy envelopes. Note that eq. 4.6 incorporates the narrow band-pass filter with central frequency ω_0 through the term $f(t)$. Here we drop the spatial dependence of the wavefield quantities in order to make easier the notations. One of the critical aspects in the comparisons between RTT and full-waveform simulations is the effect of the frequency band. In this way, we decompose the intensity over its different frequency components in order to understand the impact of filtering on the RTT energy envelopes:

$$\langle |u(t)|^2 \rangle = 4 \iint_0^{+\infty} \langle \hat{G}(\omega_1)\hat{G}(\omega_2)^* \rangle \hat{f}(\omega_1)\hat{f}(\omega_2)^* e^{-i(\omega_1-\omega_2)t} \frac{d\omega_1 d\omega_2}{(2\pi)^2} \tag{4.7}$$

where the hat represents the Fourier transform (FT) of a given function and the source time function would take the following form:

$$f(t) = s(t)\cos(\omega_0 t) \tag{4.8}$$

where $s(t)$ is the envelope of $f(t)$ and ω_0 is the frequency of interest. $s(t)$ varies over a characteristic time T such that $\omega_0 T \gg 1$. By assuming that $\hat{s}(\omega)$ converges to a delta function we may localize the spectrum of u in an arbitrarily small neighborhood of ω_0. In this way, the spectrum of f can be approximated by $\hat{s}(\omega - \omega_0)/2$. By introducing barycentric coordinates in the frequency domain, $\omega = (\omega_1 + \omega_2)/2$, $\Omega = (\omega_1 - \omega_2)$, then Eq. 4.7 can be rewritten as:

$$\begin{aligned} \langle |u(t)|^2 \rangle = \frac{1}{(2\pi)^2} \int_0^{+\infty} d\omega \int_{-\infty}^{2\omega} \langle \hat{G}(\omega + \Omega/2)\hat{G}(\omega - \Omega/2)^* \rangle \\ \hat{s}(\omega - \omega_0 + \Omega/2)\hat{s}(\omega - \omega_0 - \Omega/2)^* e^{-i\Omega t} d\Omega \end{aligned} \tag{4.9}$$

Where intervals $|\omega - \omega_0| \leq B/2$, $|\Omega| \leq B$ produce the most significant contributions to the integrals, with $B \propto 1/T$ being the bandwidth of the source energy envelope $s(t)$. ω represent the internal or carrier frequency and Ω is the external or modulation frequency. By assuming that the scattering properties are almost constant within the frequency band B, we can evaluate the ensemble average product of the Green's function at the central frequency ω_0. We can now define the intensity Green's functions at the central frequency ω_0 as:

$$I(t, \omega_0) = \frac{1}{2\pi} \int_{-\infty}^{+\infty} \langle \hat{G}(\omega_0 + \Omega/2)\hat{G}(\omega_0 - \Omega/2)^* \rangle e^{-i\Omega t} d\Omega. \tag{4.10}$$

The solution to the transport Eq. (4.1) provides an approximation to $I(t, \omega_0)$ which, according to Eq. (4.9) must be convolved with a source term $S(t)$ whose FT is given by:

$$\hat{S}(\Omega) = \frac{1}{2\pi} \int_{-\infty}^{+\infty} \hat{s}(\omega + \Omega/2)\hat{s}(\omega - \Omega/2)^* d\omega \tag{4.11}$$

Equation 4.11 can be recognized as the auto-correlation function of $\hat{s}(\omega)$. Thus, the energy envelope can be approximated as:

$$\langle |u(t)|^2 \rangle \approx I(t; \omega_0) \otimes S(t) \quad \text{with } S(t) = |s(t)|^2 \tag{4.12}$$

Eq. 4.12 represents the ideal case in which the RTT intensities must be convolved with the energy envelope of a given source time function in order to properly reproduce the characteristics of direct waves. However, in the practice of seismology this procedure is rarely achieved in such a direct way. For instance, observed energy envelopes are often filtered at a given frequency band with a two-pass Butterworth filter with 4 poles. In our case, the SEM waveforms were also filtered as shown previously. In addition to this, MC solution for RTT equation averages intensities over a finite volume, whereas our SEM intensities are obtained at each point of the 2D mesh. To circumvent these issues, we retrieve the source time function by deconvolving the RTT energy densities from the SEM intensities in a homogeneous medium. We perform these procedure for each frequency band and we use (for both approaches) receivers located at 5 km from the energy injection. In Fig. 4.3 we illustrate this procedure: the RTT energy density (red line) and the SEM intensity (black line) are shown, as well as the retrieved source time function (green line). Finally, the RTT intensities are from inhomogeneous media are convolved with the retrieved source term previous to the comparisons with the SEM intensities. Margerin and Nolet (2003) adopted a similar strategy for the modeling of PKP precursors.

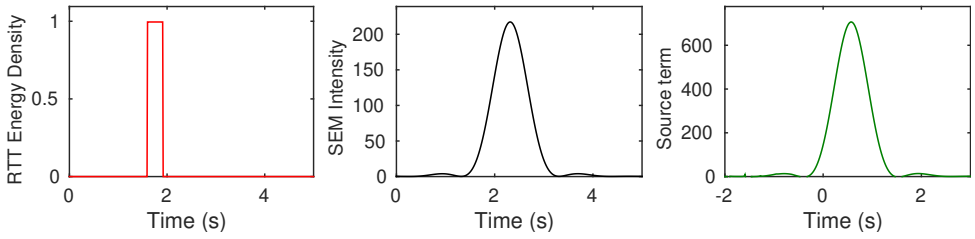

Figure 4.3: Identification of the source term in the radiative transfer equation. At a distance $z = 5$ km from the source in a non-scattering medium, the energy density predicted by RTT (Left) is deconvolved from the intensity computed by SEM simulations (Center) to obtain the source time function (Right). This example corresponds to the frequency band $[1, 2]$ Hz.

4.3.2 Comparing RTT and SEM energy envelopes

Same as in the previous chapter, comparing 'observations' from numerical simulations with their theoretical counterpart confirms the appropriate incorporation of small-scale inhomogeneities for the prediction of the seismic wavefield. In addition to this, SEM and RTT comparisons might also be useful to examine in detail the potential of RTT for the spatio-temporal evolution of seismic energy in random heterogeneous media. Comparisons are performed for the eight random media previously mentioned (Birch correlation coefficients ($\{0.5, 0.67, 0.8, 1\}$) and RMS velocity perturbations ($\{0.05, 0.1\}$)), in the frequency bands $[0.5, 1]$ Hz, $[1, 2]$ Hz and $[2, 4]$ Hz, and for different propagation distances ($\{50, 100, 150\}$ kms). The Hurst exponent is fixed at 0.25, which

corresponds to random media that are relatively rich in small-scale heterogeneities, thought to be representative of geological materials (Sato, 2019). The huge variety of propagation distances and the diverse levels of scattering as well as the three frequency bands, enables us to perform observations covering different propagation regimes, from ballistic to diffusive behaviors. As well as different frequency dependent regimes such as the Rayeligh and stochastic regimes at low and high frequencies, respectively. The emergence of the diverse regimes might also have a signature on the shape of seismogram envelopes, which are apriori controlled by the transport mean free time (τ^*) and the scattering mean free time (τ). In order to facilitate the discussion, in Table 4.1, we summarize the main scattering properties of the eight random media.

Case	$\ell(f)$			$\ell^*(f)$		
	$f = 0.75Hz$	$f = 1.5Hz$	$f = 3Hz$	$f = 0.75Hz$	$f = 1.5Hz$	$f = 3Hz$
$\nu = 1, \varepsilon = 5\%$	315.5	85.5	21	278.6	131.8	77.9
$\nu = 0.8, \varepsilon = 5\%$	229.4	58.2	13.7	221.7	103.9	60.35
$\nu = 0.67, \varepsilon = 5\%$	173.3	41.9	9.6	180.5	83.8	47.9
$\nu = 0.5, \varepsilon = 5\%$	107.8	24.6	5.5	125.8	57.4	32.0
$\nu = 1, \varepsilon = 10\%$	78.7	22.4	5.5	69.5	32.9	19.5
$\nu = 0.8, \varepsilon = 10\%$	57.4	14.6	3.4	55.6	25.9	15.1
$\nu = 0.67, \varepsilon = 10\%$	43.5	10.5	2.4	45.1	20.9	11.9
$\nu = 0.5, \varepsilon = 10\%$	26.9	6.1	1.4	31.5	14.4	8.0

Table 4.1: Scattering (ℓ) and transport (ℓ^*) mean free paths for the set of random media considered in Figures 4.4 and 4.5. The central frequencies correspond to the analyzed frequency bands ($[0.5, 1]$, $[1, 2]$ and $[2, 4]$ Hz)

RTT and SEM energy envelopes are compared in 4.4 and 4.5. To eliminate statistical fluctuations, SEM intensities were averaged over 180 realizations. Overall, very good agreement is found between both approaches, either in the early ballistic part or in the late coda. However, the fit between SEM and RTT is not uniform and can slightly change depending on the level of perturbation, distance or frequency band. The biggest discrepancies are observed at random media with the strongest scattering (small values of ν and $\varepsilon = 10\%$). Diverse reasons might explain these discrepancies: (i) the treatment of the absorbing boundary conditions which is different at each approach. In the case of MC simulations of RTT, this absorption is perfect as the random walk of the seismic phonon is automatically terminated since this escapes the propagation medium. Whereas in SEM simulations the absorbing BC is less efficient (we used the old implementation of Stacey (1988)). This can generate that waves interacting with the boundaries at large incidence angles get partially reflected, and as result, these spurious reflections may contribute to the high amplitudes in the coda. A second fact that might explain the discrepancies between SEM and RTT envelopes is the finite frequency band in SEM simulations. As shown in chapter 3, in the Rayleigh regime (low frequency) scattering attenuation presents strong variations. The effects of these huge variations might be less significant at cases with low perturbation levels as attenuation is still very weak. This might explain the differences of amplitude in the early regimes, particularly at cases $\nu = 0.67$ and $\nu = 0.5$ with $\varepsilon = 10\%$. (iii) A third source of discrepancies is evidenced by the systematic gap of amplitudes in the coda part as the scattering strength is more significant (ν decreases and ε increases). This behavior is observed predominantly at the 250km receiver in the frequency bands [1-2] and [2-4]Hz, and for cases with $\varepsilon = 10\%$ (Fig. 4.5). Such discrepancy might be due to the possible limitations of our adopted solution for the RTE which is based on the Born approximation which is a perturbative approach.

Comparisons shown in Figures. 4.4 and 4.5 (predominantly in the intermediate-to-high

frequency ranges,[1, 2] Hz, [2, 4] Hz), exhibit diverse scattering signatures that are well captured by both approaches with very good agreement. A first, and most evident signature, is the attenuation with distance of the ballistic components, which can also experience a broadening of its peak. The second mayor evidence of scattering, shown on our energy envelopes, is the emergence of coda waves. This is the result of back-scattered energy coming from the attenuated coherent components. Quantifying this ratio of energy from coherent-to-incoherent are the basis to characterize scattering properties in the contexts of seismology and acoustics ((Fehler et al., 1992; Hoshiba, 1993; De Rosny and Roux, 2001)). The implementation of some of these techniques will be discussed in next chapter.

At long propagation distances, the majority of energy envelopes of random media with $\varepsilon = 10\%$ in the [1-2] and [2-4]Hz bands, exhibit shapes that are characteristic of the diffusion regime. This is the scenery when the propagation distance is larger than the transport mean free path ℓ^*. In such cases, the amplitudes of coda regime can be even larger than the ballistic components, which can completely lose the signature of the seismic source. This makes convenient the use of diffusion approximation as no ballistic regime is needed. In Fig. 4.6 we show an example of comparison between SEM and RTT envelopes with those from the diffusion approximation. The agreement is better as frequency increases (stronger scattering), whereas at low frequency there are huge discrepancies due to the high dominance of ballistic components. Note that, since our random media do not have absorption, envelopes seem to gain energy with time. However, in real cases (media with absorption) energy would decrease with time until reaching the background noise level. This diffusive behavior have been reported in highly heterogeneous geological contexts such as volcanoes (Wegler and Lühr, 2001; Wegler, 2003; Del Pezzo, 2008) or in planetary seismology (Dainty et al., 1974; Gillet et al., 2017; Karakostas et al., 2021). The application of the diffusion model to constrain attenuation properties from real data will be discussed in chapter 5.

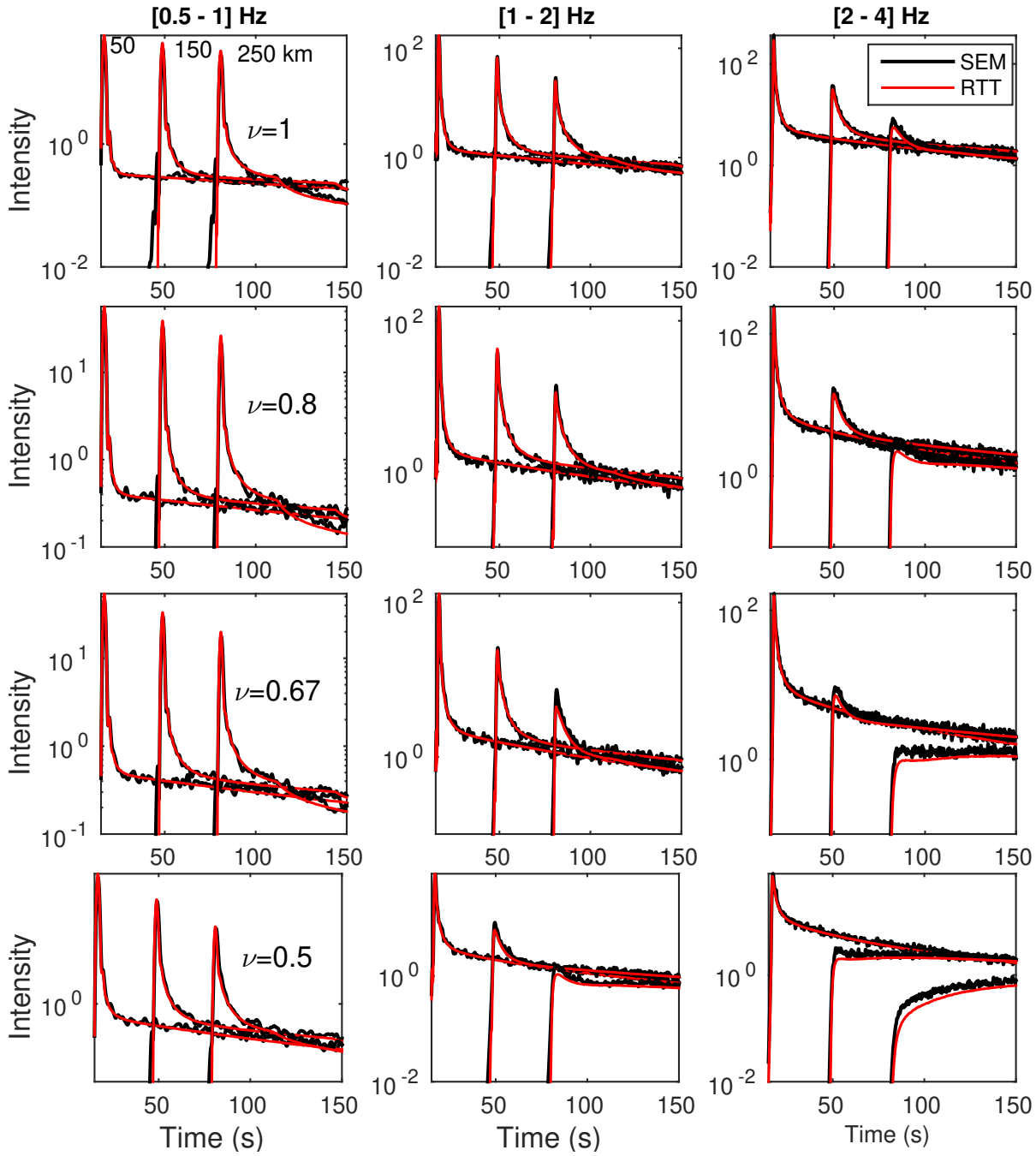

Figure 4.4: Mean intensity comparisons between SEM and radiative transfer theory solution. Results are shown for three frequency bands [0.5 1], [1 2] and [2 4] Hz, and for three different distances, at 50, 150 and 250 km. Red line corresponds to SEM intensities and the black lines are the radiative transfer theory solution. Cases $\varepsilon = 5\%$.

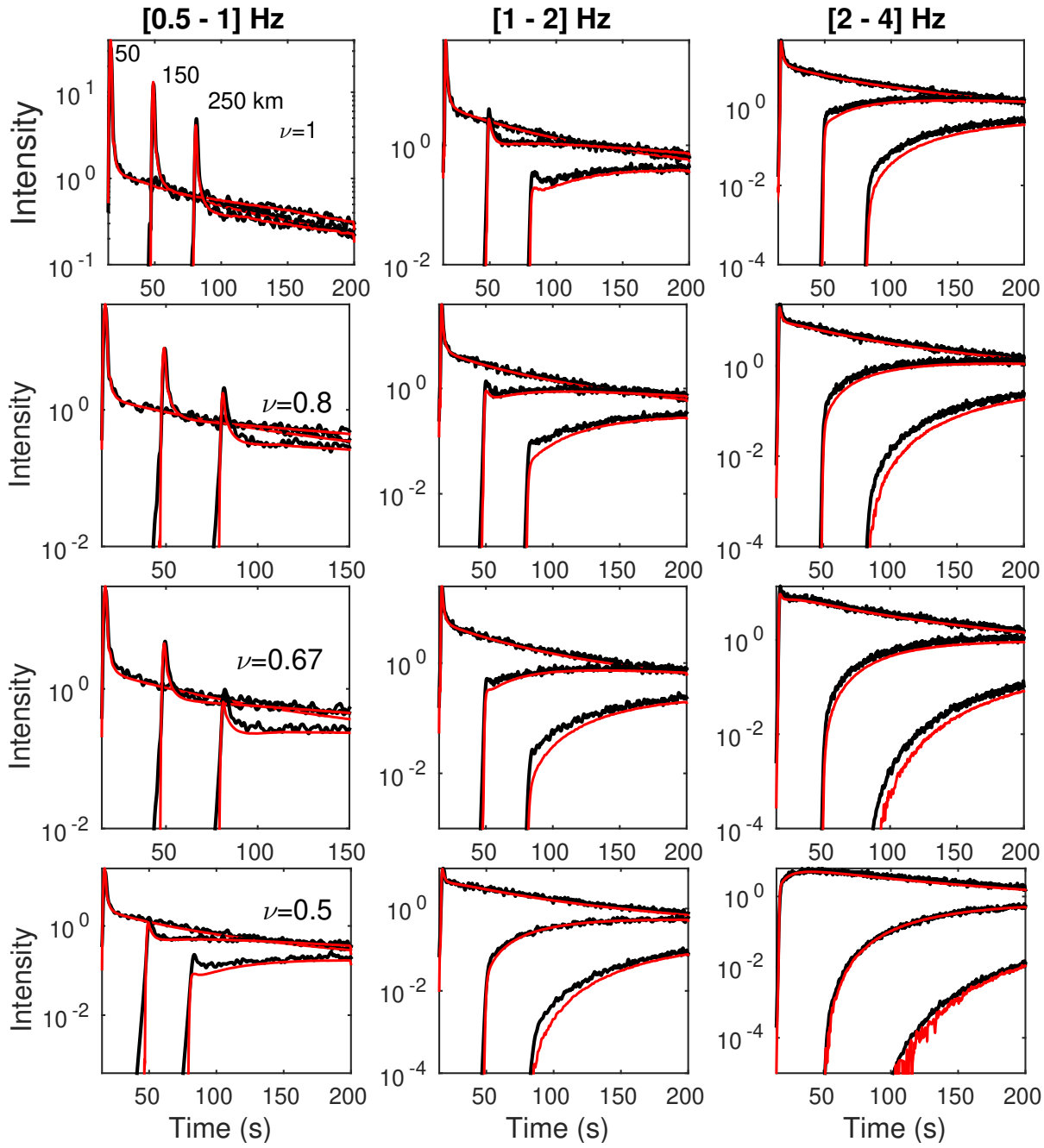

Figure 4.5: Same as Fig. 4.4 for cases $\varepsilon = 10\%$

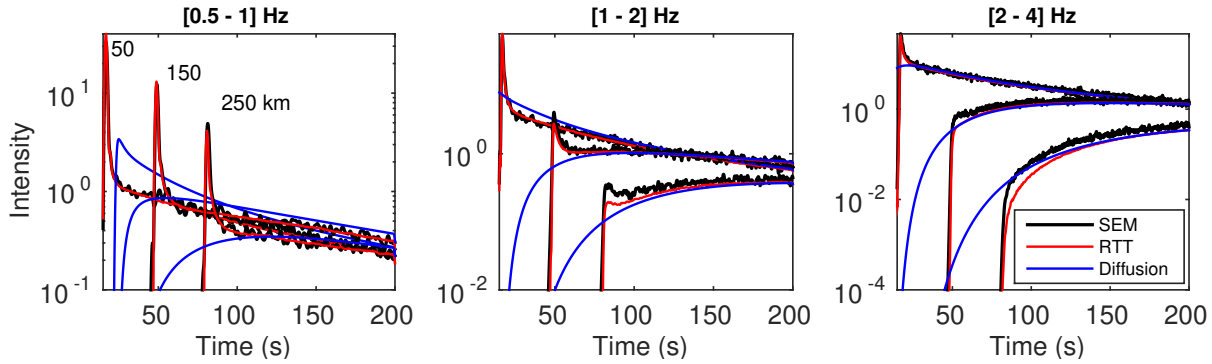

Figure 4.6: Comparisons of SEM, RTT and diffusion approximation envelopes in the case $\nu = 1$ and $\varepsilon = 10\%$. Red and blue lines correspond to the theoretical models (RTT and Diffusion), while the black solid lines represent the SEM simulations.

4.4 Intensity distributions

In the previous section we have studied the spatio-temporal evolution of energy envelopes, by analyzing different von Kármán media, frequency bands and propagation distances. The quantities shown in Figures. 4.4 and 4.5 represent average values over several realizations. The level of fluctuations around these mean quantities can potentially indicate the transitions between different propagation regimes or reveal some scattering information of the heterogeneous media. In the field of atmospheric optics, the level of fluctuation is often quantified through the scintillation index $\beta^2 = \langle I^2 \rangle / \langle I \rangle - 1$, as an indicator of the propagation regime (Rytov et al., 1989). For example, $\beta \ll 1$ is interpreted as a regime of weak fluctuations, and $\beta \approx 1$ would indicate a strong fluctuations regime. In seismology, investigating these fluctuations is a recent and active work (Hoshiba, 2000; Nakahara and Carcolé, 2010; Müller and Shapiro, 2003; Yoshimoto et al., 2015; Emoto and Sato, 2018). In the context of engineering seismology, fluctuations on the prediction of the peak ground motion (velocity or acceleration) is a useful tool to quantify the epistemic uncertainty of the seismic hazard assessment. Yoshimoto et al. (2015) observed that these fluctuations increase with frequency and hypocentral distance. These authors proposed an equation to evaluate the amplitude fluctuations of seismic waves propagating in von Kármán media. They found that the fluctuations of peak amplitude are governed by a log-normal distribution. By using 3D numerical simulations of the full-wavefield Emoto and Sato (2018) analyzed the distribution of intensities confirmed the dominance of log-normal and exponential density functions on the distribution of peak and late coda intensities, respectively (see Goodman (2015) for the basic theory). Inspired by the works of Yoshimoto et al. (2015) and Emoto and Sato (2018) we perform statistical analyses on the fluctuations of intensities in order to understand the transition from ballistic to diffusive behaviors.

The identification of different scattering regimes is achieved by comparing how well SEM intensities obey, either a Log-normal or an exponential distribution. These distributions were analyzed by choosing two different lapse times: $T1$ which corresponds to the arrival time of the ballistic peak and $T2$, 80 seconds later of it, in which the late coda is expected to be dominant. We used cumulative distribution functions (CDF) for our statistical analyses. Empirical and modelled CDF were calculated at short time windows around lapse times $T1$ and $T2$ whose size were chosen as $\frac{1}{f_c}$, where f_c is the central frequency. The CDF of the log-normal distribution was

computed as:

$$F_{ln}(I) = \frac{1}{\sigma\sqrt{2\pi}} \int_0^I \exp \frac{-(\ln x - \mu)^2}{2\sigma^2} dx \tag{4.13}$$

And that of the exponential distribution was computed as

$$F_{exp}(I) = 1 - \exp \frac{-I}{\mu} \tag{4.14}$$

Where μ and σ are the mean intensity and its standard deviation at a given lapse time. In this way, the calculation of modelled CDF require only these two basic statistical parameters. Emoto and Sato (2018) reported that when intensities obey an exponential distribution, the phase of the wavefield is random and incoherent, due to a multiple diffusion regime. Furthermore, when intensities are well described by a log-normal distribution, the coherent wave is still dominant over the incoherent part. This behavior can be observed in Fig. 4.7 (top) for frequency band [1 2] Hz at a distance of 5 km from the source, case $\nu = 1$ $\varepsilon = 5\%$. For both time windows, the statistical behavior is as expected: $T1$ exhibits low deviation and it is well controlled by a log-normal distribution. In the long lapse-time, fluctuations are considerably higher and intensities are rather exponentially distributed. At a longer propagation distance ($Z = 150$ km) Fig. 4.7-bottom, intensities are, unsurprisingly governed by an exponential distribution. However, the ballistic peak, which is often expected to obey a log-normal distribution, is now rather controlled by an exponential one. This behavior might suggest the dominance of multiply-scattered components on the ballistic peak. Such interpretation is consistent with the values of the scattering (ℓ) and transport (ℓ^*) mean free paths for the model and [1-2]Hz band shown in Fig. 4.7-bottom. As the propagation distance (150 km) is much larger than both, $\ell = 24$ km and $\ell^* = 57$ km, one might expect first, a significant attenuation of the coherent components and second the emergence of multiple diffusion. The portion of these scattered waves which propagates in the forward direction, might be mixed with the direct energy. This would generate the formation of a 'quasi-ballistic' peak whose attenuation properties will be investigated in Section. 4.5.

We will now focus on the intensity distributions on the ballistic peak and its dependence with distance. By identifying the transition from log-normal to exponential behavior, we might be able to track the emergence of different scattering regimes with distance. Emoto and Sato (2018) studied the lapse time dependence of the intensity distribution for which they used a set of von-Kármán media with different statistical parameters. They found that for most of the cases, distribution changes from log-normal to exponential in the lapse times just after the ballistic peak. However for certain levels of velocity perturbation and distance ranges they observed this crossover at earlier lapse times. In this work we perform a similar analyses on distance domain. To quantify the dominance of a given modelled CDF, we measured the mean absolute error (MAE) between observations and predictions (log-normal and exponential). In this way, at a given distance, the smallest MAE would indicate the best modelled CDF describing the distribution of peak intensities. The MAE is measured as $(1/N)\sum_{i=1}^{N} |O_i - Ei|$, where N is the number of data, O_i and E_i are the observed and expected CDF values for each intensity, respectively.

In Fig. 4.8 we show the distance dependence of MAE at two cases with the same correlation coefficient $\nu = 0.8$ and different perturbation levels ($\varepsilon = 5\%, 10\%$) in the three frequency bands. As reference and for further analyses, we also show the location of scattering mean free path (black dashed line) in the horizontal axis. Overall, the ensemble of cases shown in Fig. 4.8 cases exhibit some crossover from log-normal to exponential distribution, except for the frequency band [0.5 - 1]Hz, $\varepsilon = 5\%$. In this case, the distribution of intensities remain dominated by the log-normal distribution ($MAE_{ln} < MAE_{exp}$) within the whole range of propagation distances.

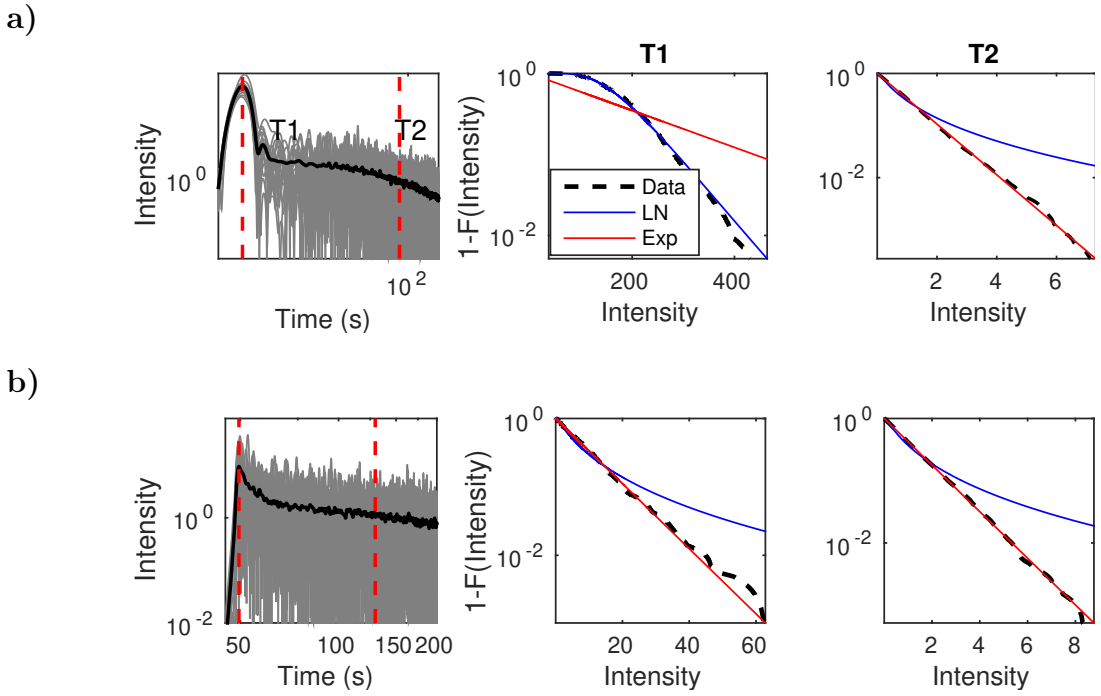

Figure 4.7: Distribution of intensities at distances (a) 5 km and (b) 150 km from the source for the case $\nu = 0.5$, $\varepsilon = 5\%$ in the $[1, 2]$ Hz frequency band. (Left) Ensemble of 180 realizations of SEM intensities (grey lines) and their mean value (black line); (Center and Right): Complement of the CDFs of intensities around lapse times T1 and T2 corresponding to the the ballistic peak and the late coda (as indicated by the dashed red lines in the left panels). The solid blue and red lines show the fitted Log-normal and exponential CDF. The black dashed line represents the the empirical complementary CDF from SEM simulations.

This suggests that the behavior of the ballistic peak is predominantly coherent and no significant incoherent components contribute to it. For the rest of the cases, results evidence that at short distances, intensity distributions are dominated by a log-normal distribution. This dominance is then switched to an exponential behavior as distance increases. Note that for the case with the highest level of scattering ($\varepsilon = 10\%$), the switch from log-normal to exponential behavior occurs near the shortest propagation distance (5 km), suggesting that the whole transport of peak energy is composed by forward scattered waves.

As outlined above, the transition from log-normal to exponential distribution is related to the crossover from coherent to 'quasi-ballistic' behavior. We now pay particular attention to the critical distance (R_c) at which this crossover occurs. Fig. 4.8 shows that this critical distance decreases with frequency and the perturbation level, which is consistent with the frequency dependence nature of the scattering phenomenon. Furthermore, for most of the cases there exists some degree of coincidence between R_c and the scattering mean free path. In order to analyze more systematically this potential agreement, in Fig. 4.9 we plot the ratio of R_c and ℓ as a function of ℓ for all the von Kármán media and frequency bands. Circles represent the extreme cases at which the intersection does not occur either because of very weak or extremely high scattering. In the former, intensities behave as ballistic in the whole range of propagation distances. In the latter, scattering is that strong that even at very short propagation distances, the peak intensity is dominated by forward scattered waves. For graphical purposes, in this case we represent R_c as 5 km (shortest propagation distance) and 300 km (longest propagation distance). The crosses

represent that majority of cases, for which there exist an critical distance within the whole range of propagation distance. These results confirm certain relation between the quantities ℓ and R_c, suggesting that the transition from log-normal to exponential distribution might be controlled by the scattering mean free path ($R_c = O(\ell)$). This could be used as an upper bound to constrain ℓ. It is worth mentioning that we are note aware of field observations, and future work could be done with respect to this.

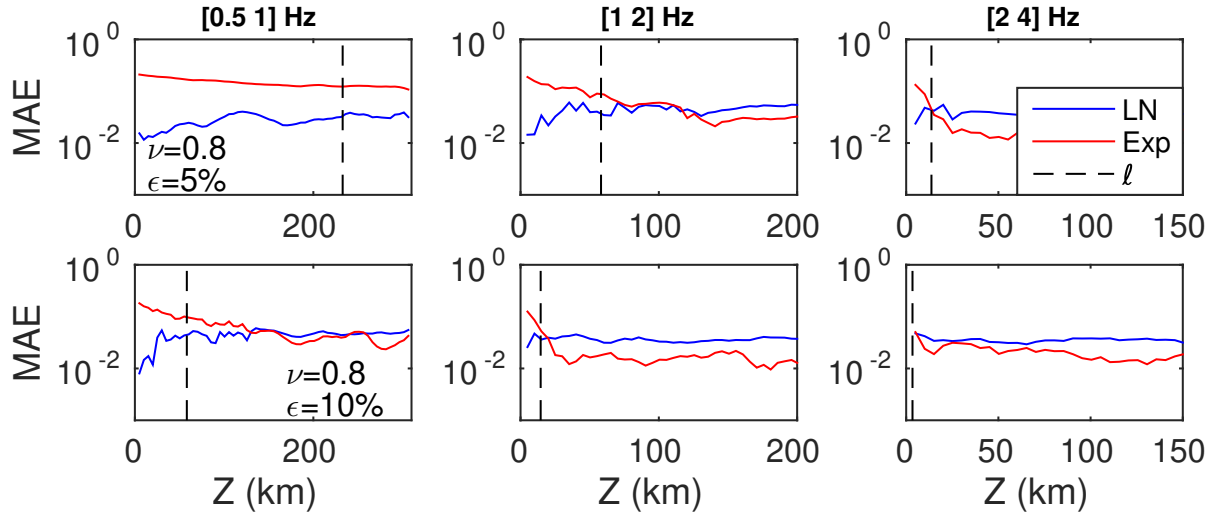

Figure 4.8: Distance dependence of intensity distributions at the ballistic peak for cases $\varepsilon = 5\%$. Blue and red lines are the log-normal and exponential distributions, respectively. The dotted black line corresponds to the value of scattering mean free path for each specific central frequency

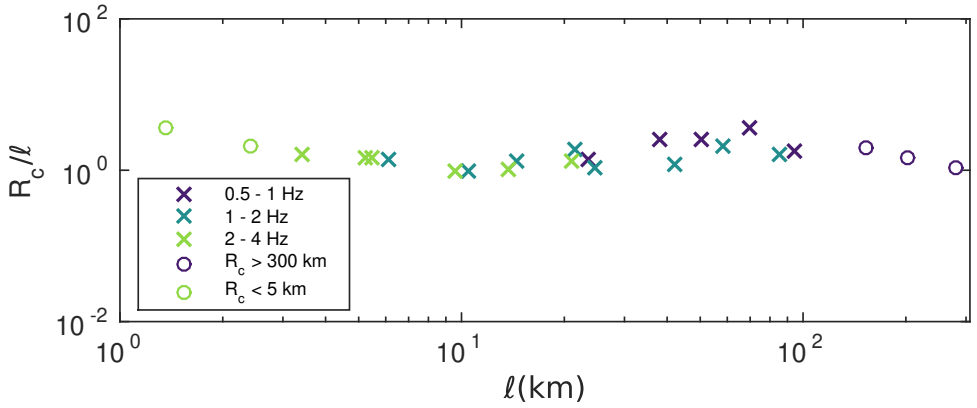

Figure 4.9: Scaled critical distance R_c/ℓ as a function of ℓ. Colors stand for the three frequency bands. The circles denote the cases at which R_c takes values either larger than the maximum epicentral distance (300 km) or shorter than the minimum (5 km)

4.5 Peak Intensity Attenuation

Unlike the mean wavefield (coherent wave), mean intensities provide information from both, coherent and incoherent components of the wave propagation. This allows to visualize different scattering regimes. Previous works (Wu (1982) and Sato (1982)) have already recognized that even the so called 'direct waves' are composed of this mixture (coherent and incoherent energy). Since in the practice of seismology accessing to the coherent wavefield is so difficult, interpretations on the energy decay of 'direct waves' remain ambiguous. The purpose of this section is to shed some light on this issue.

The statistical analyses presented in section 4.4 showed that for propagation distances larger than the scattering mean free path, the peak intensity starts obeying an exponential distribution. This fact was interpreted as the high influence of forward scattered waves on the peak intensity, whose decay might not be given by the scattering mean free path. We now focus on the attenuation characteristic of this 'quasi-ballistic' peak. In this case, we shall localize our observations in higher number of frequencies.

We first filter the waveforms obtained from SEM simulations in narrow frequency bands $\left[5/6f_0, 7/6f_0\right]$ with f_0 increasing from 0.5 Hz to 5 Hz by increment of 0.5 Hz. We used a two-pass Butterworth filter with 4 poles. Intensities are then calculated using the definition (4.5) and averaged over 180 realizations (ensemble average of intensities). The operation is repeated every 5 km for propagation distances ranging from 5 km to 300 km. Finally, at each frequency, we normalize the average intensities by the maximum value $\sup I(z,t)$. Normalized peak intensities are displayed as a function of distance for each frequency in Figure 4.10. Note that since a logarithmic scale is used on the vertical axis, an apparent linear behavior corresponds to an exponential decay in space. Such a behavior is clearly observed at all frequencies at sufficiently short distance from the source.

As distance increases the apparent exponential behavior eventually breaks down. This feature is particularly clear for the strongest scattering media for which an an abrupt change of the slope can be observed in the peak intensity decay curve. This corresponds to the transition towards the diffusion regime where the maximum intensity is reached in the coda. Similar to scattering attenuation measurements in chapter 3, the range of propagation distances for which the intensity decay can be considered exponential was determined by visual inspection, resulting in threshold values of intensities ranging from 5% to 10% of the maximum intensity. The apparent attenuation length of the peak intensity (ℓ_I) is subsequently determined by a simple linear regression of the logarithm of intensity with distance. The results (with respective uncertainties) are shown in Figure 4.10 (upper right panel). While peak intensity attenuation increases with frequency, the comparison with results from chapter 3 reveals that both its magnitude and frequency dependence differ significantly from the predictions of mean field theory. In other words, the apparent decay length of the peak intensity is not controlled by the scattering mean free path.

The anisotropic assumption in our adopted RTT solution requires to consider two length scales. On one hand, the scattering mean free path ℓ is defined as the characteristic distance between scattering events and it also predicts the decrease of the coherent wave. On the other hand, the transport mean free path ℓ^* defines the typical length after which the multiple diffusion emerges. The latter also controls the broadening of energy with distance (Gusev and Abubakirov, 1999). By comparing estimates of scattering attenuation from the isotropic and the anisotropic assumption, (Gaebler et al., 2015) showed that ℓ^* is the only scattering property that can be measured with enough confidence. Their results also suggested that the retrieved attenuation length from the isotropic assumption should be interpreted as ℓ^*. In this way, one might expect that ℓ^* controls the decay of 'quasi-ballistic' peak with distance. In order to test this possibility,

in Fig. 4.10 (bottom) we plot the normalized intensity re-scaled by the factor $\exp(z/\ell^*(f))$ as a function of z/ℓ^*. Overall, we observe that in the case $\nu = 0.5$ and $\varepsilon = 5\%$, the transport mean free path can well predict the attenuation of the peak intensity in a range of distances of the order of ℓ^*. Note that in the low frequency regime (low anisotropy), this decay is still controlled by ℓ^* for propagation distances beyond 2 transport mean free paths. This regime is also characterized by the short differences between the scattering and the transport mean free paths. By using theoretical and experimental investigations Zhang et al. (1999) found the that scattered waves exhibit a quasi-ballistic behaviors at propagation distances of the order of three mean free paths. Even though their work did not focus on the peak energy behavior, these insights agree with our results shown in in Figure 4.10.

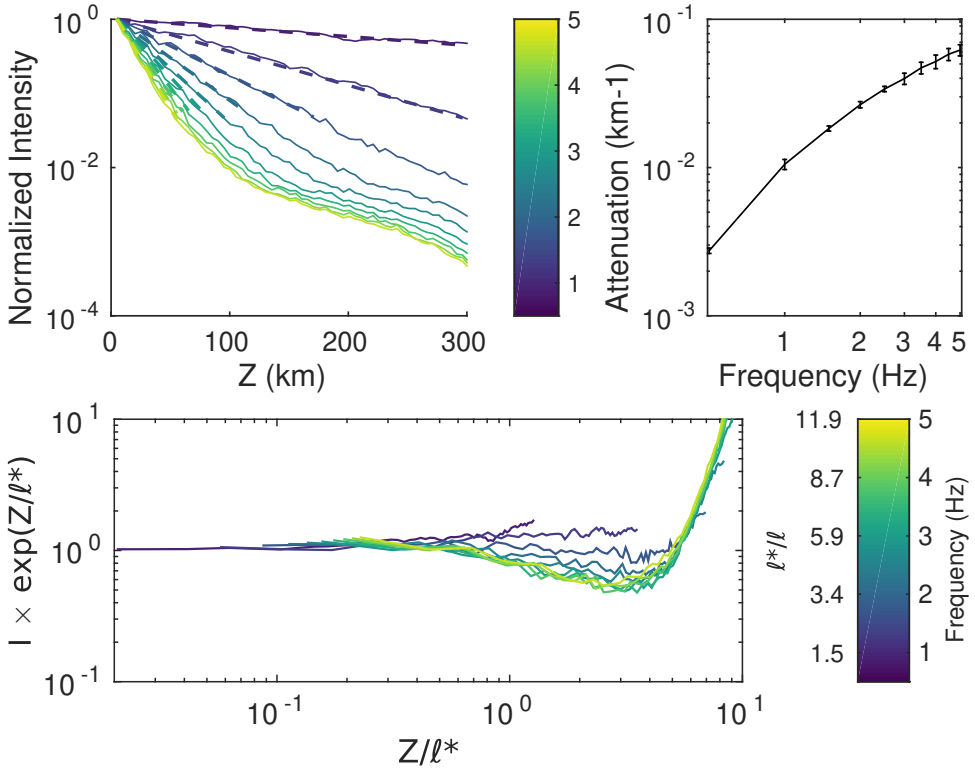

Figure 4.10: Measurement of peak intensity attenuation. (Left) Peak intensity decrease with distance (solid lines) and the fitted exponential regression (dashed lines), the colorbar represents different central frequencies ranging from 0.5 to 5 Hz with a frequency step of 0.5 Hz. (Right) Peak intensity attenuation and bar errors. (Bottom) dependence of scaled intensity $I \times exp(z/\ell^*)$ versus z/ℓ^*. Case $\nu = 0.5$ $\varepsilon = 5\%$

To facilitate the discussion about the role of ℓ^* in seismic attenuation, in Fig. 4.11 we compare the peak intensity attenuation ℓ_I^{-1} estimated from SEM with the theoretical predictions of ℓ^{*-1} and ℓ^{-1} for the ensemble of random media. For reference, we also show the attenuation of the peak particle velocity of the coherent wavefield (ensemble-space average), which was similarly measured through the exponential decay with distance. Overall, peak intensity attenuation remains close to the transport mean free path in the whole frequency range, however this agreement becomes stronger as frequency and perturbation level increase. At lower frequencies, specially $f < 1$Hz, the peak intensity attenuation tends to be closer to the scattering mean free path. This could be related to the low level of scattering at such frequency range where the ballistic pulse stays almost coherent and no significant redistribution of energy occurs. As expected, the attenuation of the coherent peak is well controlled by ℓ in the vast majority of cases, except for $\nu = 0.67$ and

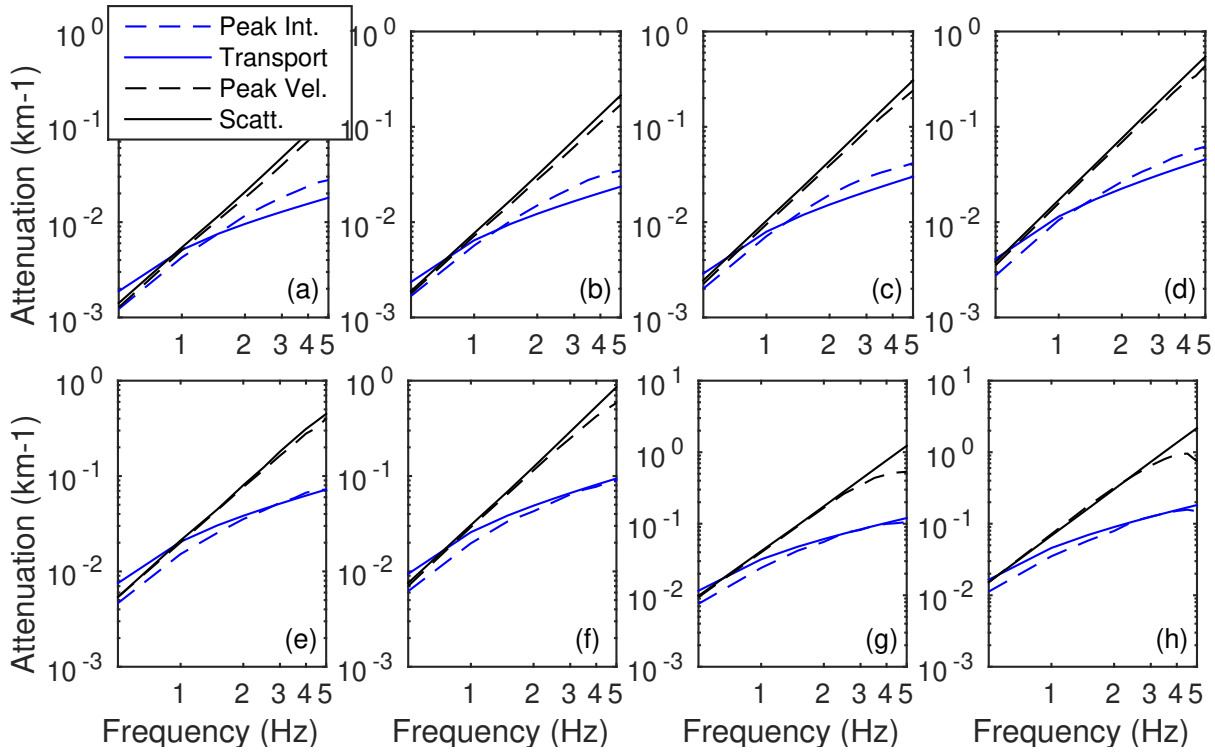

Figure 4.11: Peak intensity attenuation (dashed blue line) and comparison with transport mean free path (solid blue line), peak velocity attenuation of the coherent wave (dashed black line) and scattering mean free path (solid black line). Transport and scattering mean free paths plots correspond to their analytical solutions. Attenuation of the peak intensity is obtained from the ensemble average of the 180 realizations and the peak velocity corresponds to the ensemble-space average coherent wavefield. (Top) cases $\varepsilon = 5\%$ and (Bottom) cases $\varepsilon = 10\%$

0.5 $\varepsilon = 10\%$, where reconstructing the coherent wave becomes difficult at the chosen propagation distances (this was previously discussed in chapter 3).

4.6 Conclusion

The energy transport of SH waves in 2D random media was studied. We considered eight cases of von Kármán media with different scattering strengths. Energy envelopes were analyzed in three frequency bands and at different propagation distances, which allowed the investigation of diverse propagation regimes from ballistic to diffusive. Excellent agreement was found between numerical and RTT predictions, which confirmed the robustness of our numerical simulations but also the applicability of the adopted RTT solution.

We payed some particular attention to the behavior of the ballistic peak. First, we performed some statistical analyses on the fluctuations of the ballistic peak with distance. This allowed observe a transition from log-normal to exponential distributions, which physically is interpreted as a regime transition from ballistic to diffusive. We found some correlation between the distance at which this crossover occurs and the scattering mean free path, which suggests an alternative way to constrain this parameter. In the context of seismic hazard assessment this might shed some light on the relation between scattering properties and the epistemic uncertainty in the peak ground motion prediction. Thus, the estimation of scattering properties might help to quantify

such uncertainty, as well as the length scale at which the simulated ground motion is dominated by coherent components.

Comparisons between the peak of the coherent wave and the peak intensity allowed to identify that the attenuation of these two quantities are controlled by different length scales. While, unsurprisingly, the coherent peak is controlled by the scattering mean free path, the ballistic peak seems to decay exponentially with the transport mean free path. The mixture of coherent and incoherent components on the direct waves have been previously reported (Wu, 1982; Sato, 1982), but the relevant length scale have been under debate. For instance, (Gusev and Abubakirov, 1999; Gaebler et al., 2015) argue that the transport mean free path is the key parameter controlling the decay of seismic waves. Our analyses from full wave simulations showed that indeed the peak intensity decays exponentially with the transport mean free path. It is worth mentioning that our results correspond to media that are considerably rich in small-scale inhomogeneities and that further numerical work should be performed to investigate the range of validity of these results.

Chapter 5

Separation of absorption and scattering attenuation from seismic ambient noise at the Piton de la Fournaise volcano

The goal of this chapter is to propose a method for the characterization of small-scale absorption and scattering properties from seismic ambient noise. We use a continuous data set recorded over four years at volcano Piton de la Fournaise. Attenuation properties are estimated by comparing energy envelopes from cross-correlation functions with those from, either the radiative transfer theory or the diffusion approximation. Our technique is based on the different advantages of long and short propagation distances, which allowed to quantify attenuation properties in two stages: firstly, we measure absorption from short propagation distances to profit of the long coda durations; and secondly, scattering is measured from long propagation distances due to the higher sensitivity to this parameter. Our estimates are compared with results from the MLTWA, which shows certain level of agreement with some improvement on the accuracy. Additionally, the proposed ballistic-to-diffusive ('balldiff') ratio technique can considerably reduce the effect of the uneven distribution of noise sources. In order to validate our method we performed attenuation measurements using earthquake data corresponding to magnitudes between 1.5 to 2.5. Good agreement was found between the global estimates of these two approaches.

Keywords: cross-correlation, scattering, absorption, ballistic-to-diffusive ratio, RTT.

5.1 Introduction

Since the pioneering work of Aki and Chouet (1975), coda waves have been interpreted as the result of the interaction of primary waves with small-scale inhomogeneities in the crust. These authors demonstrated that after sufficiently long lapse-time from the energy release at the source, at a given frequency, the temporal evolution of the seismic energy follows an exponential decay. Such decay is controlled by the so known quality factor (Q_c) whose interpretation depends on the propagation regime. For example, when assuming multiple diffusion Q_c approximates to intrinsic attenuation.

With the advent of more quantitative methods, it has been possible to separate the two mechanisms controlling the attenuation of seismic waves: scattering and absorption. One of the most widely used models is the radiative transfer theory (RTT) (Wu (1985); Margerin et al. (1998)), which describes the transport of energy in media with random heterogeneities. Comparing observed energy envelopes from earthquake data with those from RTT can result in satisfactory estimates of attenuation properties (Fehler et al. (1992); Hoshiba (1993); Carcole and Sato (2010); Ugalde et al. (2010); Eulenfeld and Wegler (2016)). Fehler et al. (1992) introduced a technique based on the spatio-temporal evolution of integrated energy. This consists in comparing the total observed energy contained in three time windows with their theoretical (RTT) counterpart. The calculated energy in the selected windows represents different propagation regimes, from ballistic to diffusive behaviors. Their method, known as multiple lapse-time window analyses (MLTWA), assumes that the propagation medium is composed by isotropic scatterers uniformly distributed. Carcole and Sato (2010) obtained high resolution maps of scattering and absorption parameters by using the MLTWA. They used S-wave data at the 1 to 32 Hz band and showed that variations on attenuation properties were closely related to the tectonic and volcanic contexts in Japan.

In the last decades, the use of seismic noise has shown to be a successful alternative for studying the earth's inner structure in regions with low or moderate seismicity (Shapiro and Campillo (2004), Stehly et al. (2008)). In the context of attenuation studies, diverse works have focused on the ballistic components of the reconstructed wavefield to constrain the "anelastic" properties of the earth (e.g. Prieto et al. (2009), Liu et al. (2015)). Regarding the exploitation of coda waves Soergel et al. (2019) used cross-correlated noise signals (CCF) at the 2.5-20(s) period band to estimate Q_c in the Alps region.

On the other hand, Hirose et al. (2019) implemented by first time the use of CCFs for the separation of absorption and scattering attenuation at Sakurajima volcano. These authors obtained similar estimates to those from active shots. van Dinther et al. (2020) used CCFs to study lateral variations of scattering properties in the North Anatolian Fault (NAF) zone. Their results suggest that lateral variations of scattering should be taking into account in monitoring studies.

Piton de la Fournaise is among the most active volcanoes in the world, presenting three eruptions per year between 2000 and 2010 (Rivet et al. (2014)). It is located in the south-east part of La Réunion island (see Fig. 5.1) and it is often referred as a basaltic-shield volcano (Lénat et al. (2012)). Monitoring seismic properties by using seismic ambient noise has allowed to understand the dynamics of this volcano (Duputel et al. (2009); Rivet et al. (2014); Mordret et al. (2015); Sens-Schönfelder et al. (2014); Clarke et al. (2013); Obermann et al. (2013)). The expected high level of heterogeneities and the presence of magmatic fluids make attractive to study attenuation properties at such an active volcano, as these mechanisms can pronouncedly shape the seismic records of propagating waves. At similar geological contexts, Hirose et al. (2019) and Hirose et al. (2022) used a MLTWA-based technique on CCFs to measure attenuation properties at diverse volcanoes in Japan. Even though the apparent robustness of their results, the interpretation on

the accuracy in scattering estimates remains ambiguous since MLTWA assumes that scattering is homogeneous.

In this work we present measurements of attenuation properties (scattering and absorption) at volcano Piton de la Fournaise from cross-correlation of seismic noise in three frequency bands ([0.5 - 1], [1 - 2] and [2 - 4] Hz). Our attenuation estimates are presented in terms of transport mean free path ℓ, to characterize scattering, and absorption parameter b corresponding to the intrinsic attenuation. First, measurements are performed with the MLTWA, by using three 15(s) time-windows. Secondly, we propose a 2-stages technique that allows the individual measurements of b and ℓ at each energy envelope. Our results evidence the high influence of anisotropic noise source effects on scattering estimates. Additionally, we search to reduce these effects by using the ratio of ballistic to early diffused fields. In order to validate our technique we compare attenuation estimates from CCFs with those from earthquake data whose magnitudes range between 1.5 and 2.5.

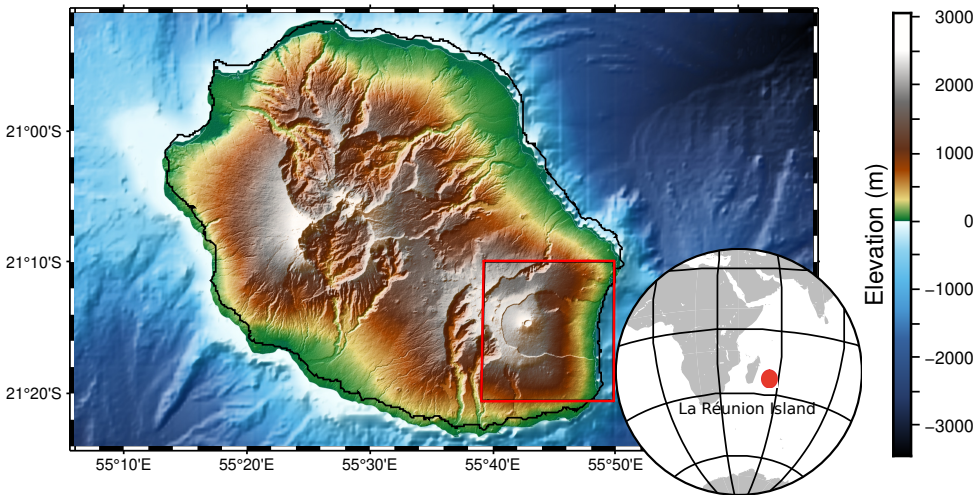

Figure 5.1: Map of Piton de la Fournaise volcano. The red rectangle indicates the location of Piton de la Fournaise volcano on La Réunion Island, as well as the investigation area. The bottom-right inset shows the location of La Réunion island in the Indian Ocean. Colors in the map stand for different elevations.

The organisation of this chapter is as follows: in Section. 5.2 we present the cross-correlation functions and its corresponding processing for the obtention of the observed energy envelopes; Synthetic energy envelopes from RTT and diffusion approximation are shown in Section. 5.3, in which we show the effects of absorption and scattering parameters on the shape of energy envelopes; The inversion techniques for absorption and scattering attenuation are introduced in Section. 5.4, whose results are then compared with estimates from earthquake data in Section. 5.5 in order to validate our method. Finally, some conclusions are presented in Section. 5.6.

5.2 Data and processing

We use continuous data recorded over four years, from January 2018 to December 2021. Such data set corresponds to the PF array (OVPF and IPGP (2008)) which is continuously monitoring the activity of PdF volcano. The PF array is composed by 41 three-component broadband seismometers which are geographically distributed mainly on the volcano edifice, but also on a wider extension of the whole island. Our study focuses on the vertical component of the ground motion, whose wavefield is expected to be dominated by Rayleigh waves. Seventeen

stations (120 paths and 17 auto-correlations) are used, and the maximum aperture is limited to 16 km. The pre-processing and later cross-correlation of noise signals, were performed by using `pycorr` (Stehly and Boué, 2022) which is a suite of python code that also includes the retrieval of seismic stations and waveforms of the study area. Initially, data are down sampled to 20 Hz and corrected for the instrument response. Since noise correlated signals can be significantly affected by transient amplitudes such as storms or volcanic tremors, we apply as a pre-processing the "comb-filter" technique (Soergel et al. (2019)). Noise records are first filtered into seven period bands: [0.125-0.25], [0.25-0.5], [0.5-1], [1-3], [3-5], [5-10], [10-20] and [20-40] s. These filtered signals are then normalized by their energy envelope, and finally, a stacking is performed over the seven period bands. The main advantage of the "comb-filter" pre-processing is that it can keep broadband signals without transient high amplitudes. Note that a different pre-processing technique, such as one-bit normalization (Larose et al. (2004)) would not be convenient to be applied in our study, since such non-linear operation can not retain the relative amplitudes between stations.

Once transient amplitudes have been removed, we cross-correlate vertical-to-vertical components (ZZ) of the records in time windows of 1000 s length. The stacking over time is performed firstly over each day (DCCF) and secondly over the ensemble of days of the whole time period (4 years). Note that seismic stations might often present problems of recording continuously, which results in a significant heterogeneity in the number of days recorded at each station. In order to avoid some biases related to this heterogeneity we use only stations that registered more than 1000 days during the entire period. In what follows we will refer to the cross-correlation functions stacked over the 4 years as CCFs.

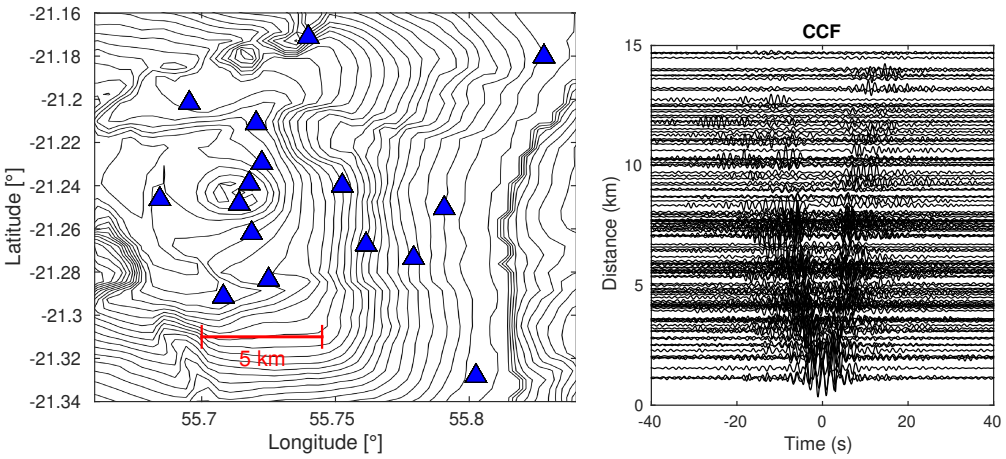

Figure 5.2: Left: Topographic map of the Piton de la Fournaise volcano and the PF seismic array. Contour lines are shown every every 100 m. Green triangles represent the seismic stations, with inter-station distances ranging from 1 to 15 km. Right: Cross-correlation functions in the frequency band [0.5-1]Hz.

Since propagation properties of seismic waves are generally frequency dependent, we must localize our observations at different frequencies of interest. In this work, CCFs are filtered in three frequency bands: [0.5-1], [1-2] and [2-4] Hz. We used a non-causal band pass butterword filter with four poles. In Fig. 5.2-left we show the location of the seismic stations (green triangles) and an example of cross-correlation functions in the [0.5-1]Hz frequency band (right), for inter-station distances up to 15 km. Note that as distance increases the ballistic part of the wavefield tends to disappear, this can be due either to attenuation (scattering or absorption) or to the high presence of undesired noise. This behavior poses a limitation in terms of the optimal distance range

used to measure scattering attenuation. In section 5.4.2 we discuss the sensitivity of scattering and absorption attenuation to distance, and how this can be profited to measure properly both mechanisms.

As mentioned in the previous chapters (e.g. 3 and 4), the models we use to reproduce synthetic data (radiative transfer and diffusion) rely on the transport of energy rather than the full-waveforms itself. For this reason, we use the energy envelopes of the CCFs in order to estimate attenuation properties. Energy envelopes are calculated by using the expression:

$$E(t) = \frac{1}{2}\left[\mathcal{H}^2\{u(t)\} + u\,(t)^2\right] \tag{5.1}$$

Where $\mathcal{H}$ is the Hilbert transform, and the ground velocity u will now correspond to the filtered cross-correlation functions. In Fig. 5.3 we show an example of CCF (top) and its energy envelope (bottom), in the [0.5 - 1]Hz frequency band for a inter-station distance of 8 km. The

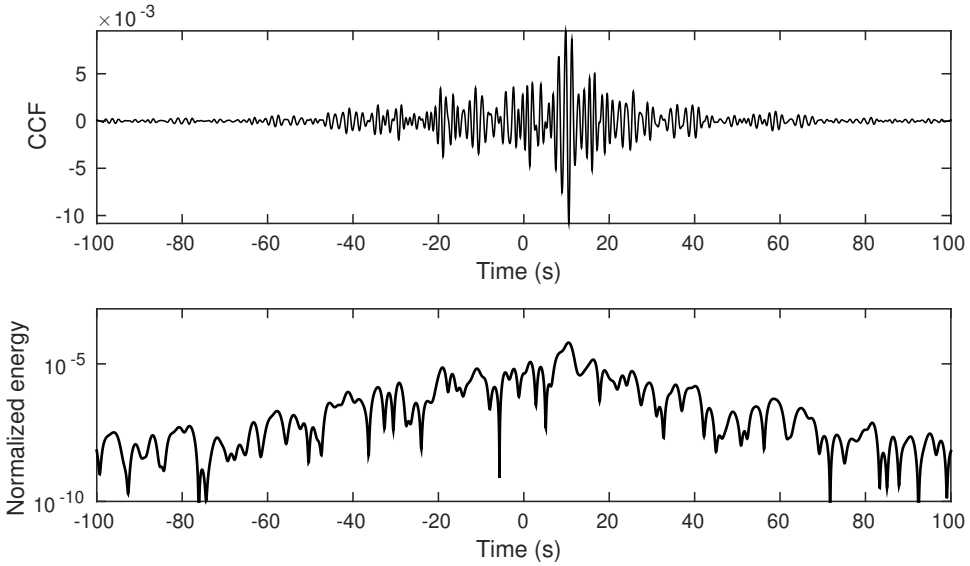

Figure 5.3: Example of cross-correlation function (top) and its energy envelope (bottom) obtained by using the square of the signal and the Hilbert transform. The CCF is reconstructed from a receiver couple whose distance is 8 km and its azimuth is 356°.

ensemble of energy envelopes are shown in Fig. 5.4 as density plots for the three frequency bands. The vertical axis corresponds to the logarithm of the signal-to-noise ratio (SNR) which was computed by dividing the whole envelope by the mean energy in the last quarter of the record. This is done independently for both, causal and acausal parts of the CCF envelope. Note that coda duration becomes shorter as frequency increases, such behavior might be due to two phenomena: (i) frequency dependence of noise source energy necessary to properly reconstruct the propagating surface waves; or (ii) to the possible variations of absorption attenuation with frequency, which determines how fast the coda decays with time.

Since `pycorr` code sets by default the causal and acausal parts of the CCF based on the alphabetic order of the station names, potential effects of directivity or azimuthal dependence can not be directly interpreted. In this manuscript, the causality of CCF are re-defined by choosing the highest SNR between both sides of the signal as causal, and that one with the lowest SNR is chosen as acausal. This re-orientation implies that if in a CCF the former acausal part has a higher SNR, the sides are now reversed but also the new azimuth is changed by its former

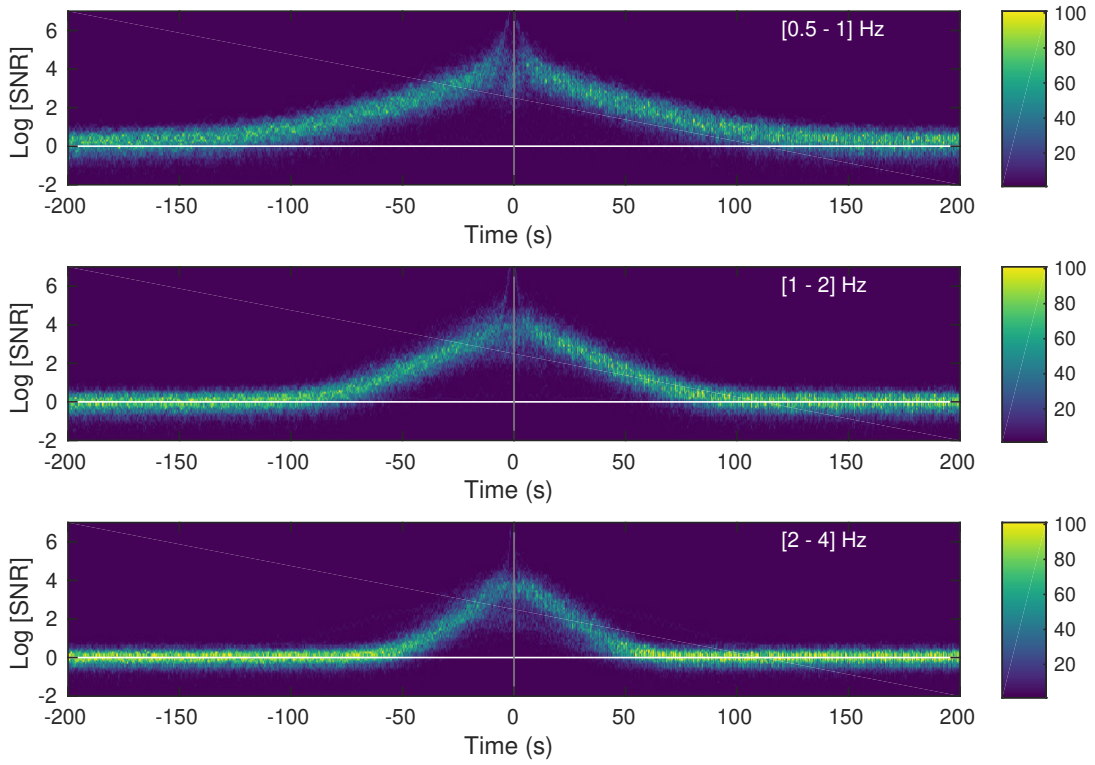

Figure 5.4: Ensemble of energy envelopes for the three frequency bands ([0.5-1], [1-2] and [2-4] Hz). Amplitudes are expressed as the logarithm of the signal-to-noise ratio (SNR). The white horizontal line represents the noise level; the colorbar indicates the density of data at given amplitude and time

back-azimuth. Fig. 5.5 shows the azimuthal dependence of SNR from the reoriented CCFs, the black and red colors represent the causal and acausal parts, respectively. SNR are computed as the mean energy in the search window of the Rayleigh wave velocity (0.5 - 2.5 km/s), divided by the mean energy in the last quarter of the record (150 - 200 s). Note that the highest SNR correspond to receiver couples forming azimuths near 270°, which points out in the west direction. This signature is in agreement with the works of Brenguier et al. (2015) and Nakata et al. (2016) who mention that, within the frequency range that we consider, noise propagates predominantly from the east to the west. It is also worthy noting that the azimuthal dependence of SNR is less significant at higher frequencies. To improve the quality of our estimates we exclude energy envelopes with SNR smaller than 4 and coda durations shorter than 30 s.

In order to remove the source and site effects, we use the coda normalization technique (Aki (1980)), in which energy envelopes are normalized with respect to the total energy contained at a given time window representing the diffused regime. In the context of earthquakes and active sources, the principle of this technique states that at a fixed lapse time in the coda, the distribution of energy becomes homogeneous, which implies that the amplitudes observed at such window are directly proportional to the source magnitude, and that possible variations in space are due to local conditions. In our case, the CCFs represent wave packets generated by an impulse source and propagate from one station to the other. However, our criterion to apply the coda normalization technique will just rely on the emergence of undesired noise. In Fig. 5.6(a) we represent the distance dependence of the lapse time at which noise emerges (noise onset) for different receiver couples at the [0.5-1]Hz band. Note that "noise onset" becomes shorter with propagation distance, which defines also the coda duration for different receiver couples. Based

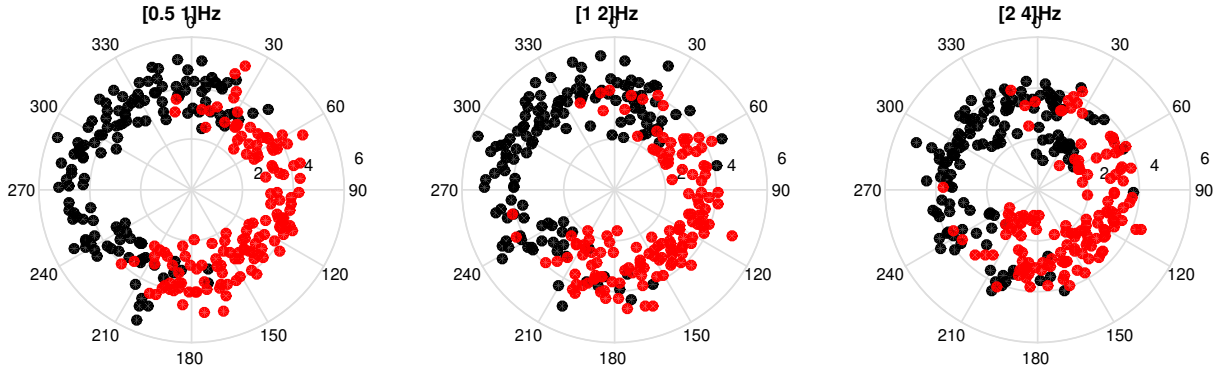

Figure 5.5: Azimuthal distribution of signal-to-noise ratio for the three frequency bands([0.5 - 1], [1 - 2] and [2 - 4]Hz,). Black and red dots correspond to the causal and acausal parts of the CCF envelope, respectively. The radius of the rose plots are given by the log10 of the SNR.

on these observations, we define the reference window for the coda normalization as the last 10 s (resp. 5 s) window before the "noise onset" for frequencies in the range [0.5 - 1]Hz (resp. [1 -2] and [2 - 4]Hz). In order to simplify the interpretation of our results, for a first set of estimates (e.g. MLTWA) we use the same reference window in all the receiver couples. In this way, we choose the minimum "noise onset" for a given frequency band. For example, for the case shown in Fig. 5.6(a) and (b) ([0.5-1]Hz), the reference window would end at 60 s for all the receiver couples. In the subsequent analyses (Sec. 5.4.2) we will discuss the convenience to use certain propagation distances at which it is possible to normalize with respect to later lapse times. As a last step for the treatment of observed energy envelopes, we perform a time smoothing within windows whose length is 2 times the central period of each band-pass filtered envelope.

Since estimates of scattering attenuation strongly depend on the "ballistic" regime, an appropriate estimation of the propagation velocity is needed. Under the assumption that the wavefield is strongly dominated by surface waves, we measure Rayleigh wave velocities by locating the peak amplitude in the range between 2.5 km/s and 0.5 km/s. Fig. 5.6(c) illustrates the steps above mentioned: the blue rectangles represent the time windows at which energy is integrated to perform the coda normalization; black and grey lines correspond to the smoothed and non smoothed energy envelopes; and the grey rectangles indicate the range of possible arrival times for the Rayleigh wave.

5.3 Modelled energy envelopes

Measurements of attenuation properties require that the previously described observed energy envelopes are compared with theoretical predictions. Comparisons are performed in a 2D grid search, from which the best fit-parameters of scattering ℓ and absorption b are constrained (see chapters 3 and 4 for the definitions). The search range for ℓ is between 0.2 to 20 km with an increase of 0.2, and that of b is between 0 to 0.2 s^{-1} with an increase of 0.01. The physical interpretation of ℓ parameter is strictly dependent on the model assumptions. In our case, we use an analytical solution of the 2D radiative transfer equation that represents the propagation of surface waves in inhomogeneous media with isotropic scattering (Sato (1993); Paasschens (1997)). This last condition implies that there is not distinction between scattering (ℓ) and the transport mean free paths (ℓ^*). However, Gaebler et al. (2015) suggest that the scattering parameter estimated from the isotropic assumption should be interpreted as the transport mean free path.

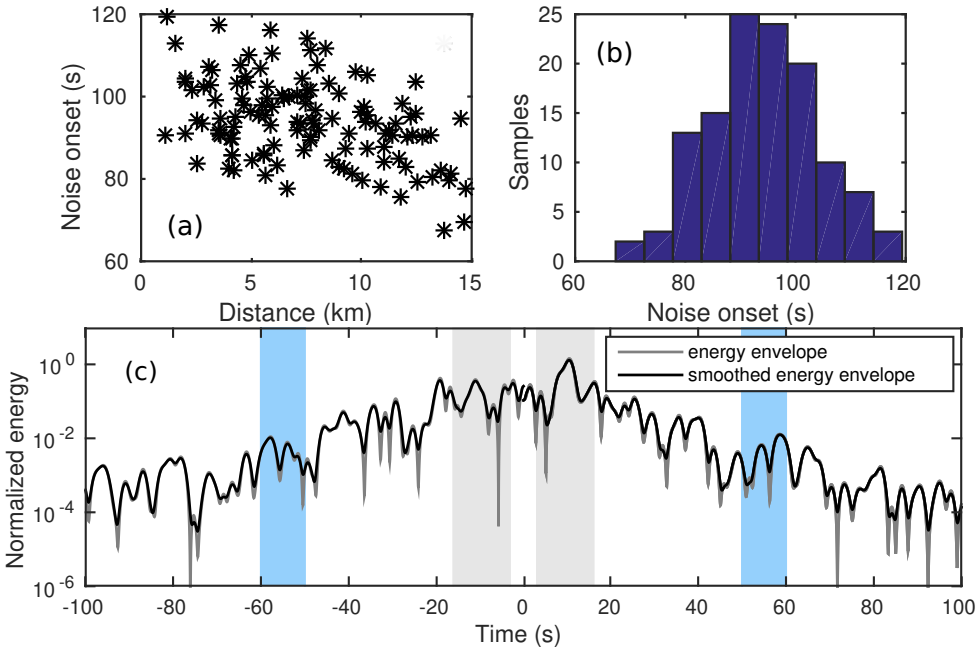

Figure 5.6: (a) Ensemble of "noise onsets" as function of distance and its statistical distribution (b); (c)Example of normalized energy envelope for a propagation distance $r = 8$ km and azimuth of 356°. The grey and blue rectangles denote the window search of the Rayleigh wave velocity and the energy integration for the coda normalization, respectively. Black and grey lines correspond to the smoothed and non smoothed energy envelopes.

These authors compared results obtained from acoustic-isotropic assumption with that from elastic-anisotropic, they found that the retrieved attenuation length from the acoustic case is much closer to the transport mean free path rather than to the scattering mean free path from the elastic approach. In this way, our estimations of ℓ are interpreted as the transport mean free path. The RTT solution for surface waves with isotropic scattering is written as:

$$E_{RTT}(r,t) = \frac{e^{-ct\ell^{-1}-bt}}{2\pi cr}\delta\left(t-\frac{r}{c}\right) + \frac{e^{\ell^{-1}\left(\sqrt{c^2t^2-r^2}-ct\right)-bt}}{2\pi\ell\sqrt{c^2t^2-r^2}}H\left(t-\frac{r}{c}\right) \qquad (5.2)$$

Where $E(r,t)$ is the energy density at a source-receiver distance r and lapse time t. c is the velocity at which the energy is being propagated. δ and H are the Dirac delta and Heaviside functions, respectively. By using this model we are assuming that surface waves are dominant in the direct wavefield and also in the late coda, even though it is known that conversion from surface to body waves is possible to occur in the coda part (Margerin et al. (2019)). The first term of the right side of the equation describes the contribution of the direct wavefield, whose decay with distance is determined by a scattering attenuation length. From 2D numerical simulations of the full wavefield, Celorio et al. (2022) showed that the attenuation length of the ballistic peak for body waves is given by the transport mean free path rather than scattering mean free path. They justify this behavior from the fact that the "ballistic" peak is not completely coherent but several non-coherent components can contribute to it. From now on, we will refer to ℓ as transport mean free path. The second term refers to the backscattered energy forming the coda part, whose amplitudes are inversely proportional to ℓ and whose decrease with time is given the absorption b. In Fig. 5.7(a) we show an example of synthetic envelope by using the Eq. 5.2,

for a propagation distance of 8 km, and wave velocity 1.18 km/s. Scattering ℓ and absorption b are defined as 5 km and 0.05 (s-1), respectively. Fig. 5.7(a) clearly illustrates the two terms of Eq. 5.2: the direct wavefield is given by the Dirac-type pulse and it is followed by a time decreasing heaviside function, which corresponds to the second term of the equation.

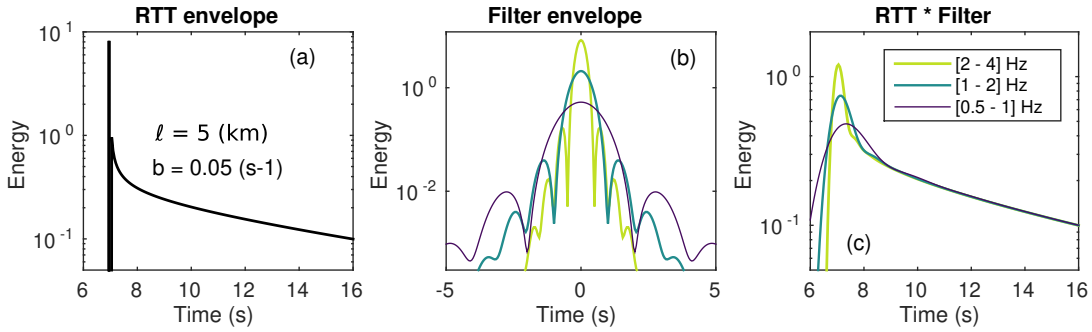

Figure 5.7: Calculation of synthetic energy envelopes. (a)RTT envelope for 2D medium with $\ell = 5$km and $b = 0.05(s^{-1})$; (b)Energy envelopes of the impulse responses for three band-pass filters ([0.5-1], [1-2] and [2-4]Hz); (c)Convolution of band-pass filter envelopes with that from RTT model.

As mentioned in chapter 4, RTT predicts the propagation of quasi-monochromatic waves in randomly inhomogenous media. Furthermore, the frequency dependence of Eq. 5.2 is just implicitly included in ℓ and b. In contrast with the observed energy envelopes, the ballistic regime of RTT does not take into account the effect of the band-pass filter, direct waves are simply represented by a Dirac type pulse. In order to improve the comparisons between RTT and the observed energy envelopes, the effects of the band-pass filters are incorporated in the synthetics by convolving RTT envelopes with the energy envelope of the impulse response of the filter. Fig. 5.7(b) shows the energy envelopes of impulse response of [0.5-1], [1-2] and [2-4] Hz filters, and the convolutions with the RTT envelope are shown in Fig. 5.7(c).
In order to assess the effects of scattering and absorption parameters on the shape of synthetic energy envelopes, in Fig. 5.8 we show diverse calculations of RTT envelopes at three different propagation distances r (2, 12 and 22 km). Scattering effect (Fig. 5.8-top) is evaluated by defining diverse values of ℓ ranging from 0.5 to 10 km and absorption parameter is fixed as $b = 0.05\ s^{-1}$. At short distances ($r = 2$ km) effects of scattering are almost negligeable except for the highest levels of scattering, where ℓ is even shorter than the minimum propagation distance (2 km). At larger distances ($r = 12$ and 22 km) energy envelopes become more sensitive to scattering, allowing to distinguish the effects within a wider range of ℓ values. The distance-dependence of scattering effects will be key for the measurements of scattering, as it will be discussed in the next section.

Absorption effect (Fig. 5.8-bottom) is evaluated by using different values for b, from 0 to 0.2 (s-1), and fixing ℓ as 5 km. Energy density calculations suggest that the effect of absorption is completely independent on the propagation distance, and its effects can rather be observed on time. Note that for real data, the exploitability in time of the energy decay is necessarily dependent on the emergence of noise level. This last condition will also be relevant for the definition of an optimal distance range for absorption measurements.

Since volcanoes are characterized as highly heterogeneous media, the strong levels of scattering might turn the wavefield very fast into the diffusion regime, which would uniformize the angular dependence of energy density. This condition makes convenient to estimate attenuation properties in volcanic environments through the diffusion approximation (Dainty et al. (1974); Wegler and Lühr (2001); Prudencio et al. (2013); Prudencio et al. (2015)). In the present work, besides RTT

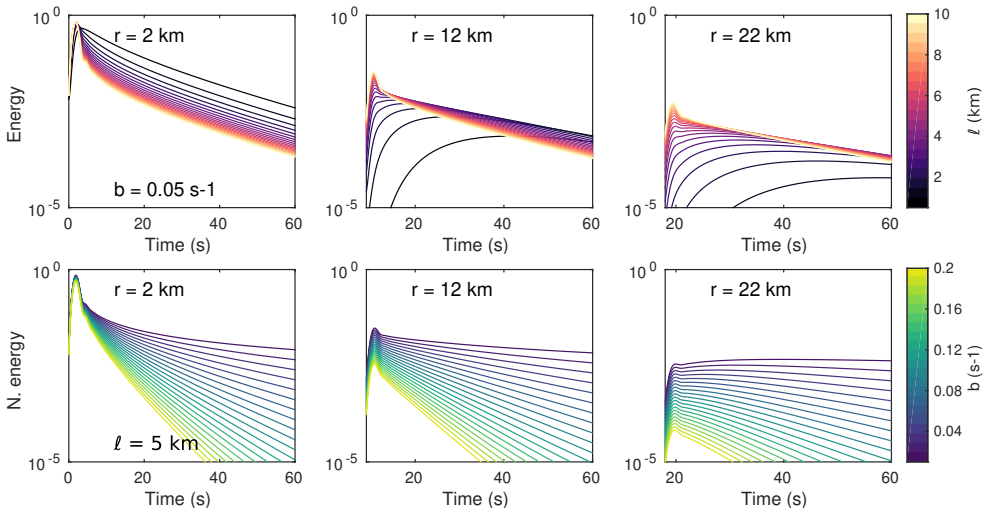

Figure 5.8: Effect of scattering (top) and absorption (bottom) at different propagation distances (2, 12 and 22 km). RTT envelopes were convolved with the energy envelope of the [0.5-1]Hz filter. Colorbar at the top represents different values of the transport mean free path (in km), and that at the bottom corresponds to variations of absorption parameter (in s^{-1}).

model, we use the diffusion approximation to estimate absorption attenuation. Then, energy envelopes are calculated from the following equation:

$$E_{diff}(r,t) = (4\pi Dt)^{\frac{-p}{2}}\, e^{\left(-bt-\frac{-r^2}{4Dt}\right)} \tag{5.3}$$

Where D is the diffusivity parameter, the term p represents the geometrical spreading, which is 2 for surface waves and 3 for body waves. Note that diffusion approximation ignores any signature of direct waves, as well as any information on the background medium. Propagation velocity of direct waves would only be necessary for the conversion of D into the transport mean free path ℓ, whose relation is given by $c\ell/2$. Fig. 5.9 shows the convergence of RTT (black lines) towards diffusion approximation (blue dashed lines) at the same propagation distances presented in Fig. 5.8 in a medium with $b = 0.05$ s-1 and $\ell = 5$ km. It is worth noting that even though there are huge discrepancies between both models at early lapse times, their solutions at longer lapse times are identical. Despite this convergence might intuitively be determined by the transport mean free time t^* (time necessary to randomize the wavefield), Paasschens (1997) repport that a particularity of the 2D case is that the only condition for the convergence of isotropic scattering-RTT towards diffusion approximation is $ct >> r$. Which means that for given propagation distance r, the diffusion regime can be achieved at lapse times just larger than the travel time and not necessarily after the transport mean free time.

5.4 Inverting for scattering and absorption attenuation

Synthetic energy envelopes described in the previous section are now used to estimate attenuation parameters (scattering and absorption) through the comparisons with observed data. Overall, inversion techniques consist in selecting the optimal parameters that reproduce the minimum misfit between observations and predictions. As shown in Fig. 5.8, scattering and absorption can generate different signatures on the appearance of energy envelopes, whose sensitivity is strongly dependent on the propagation distance and the lapse time. Thus, selecting the appropriate

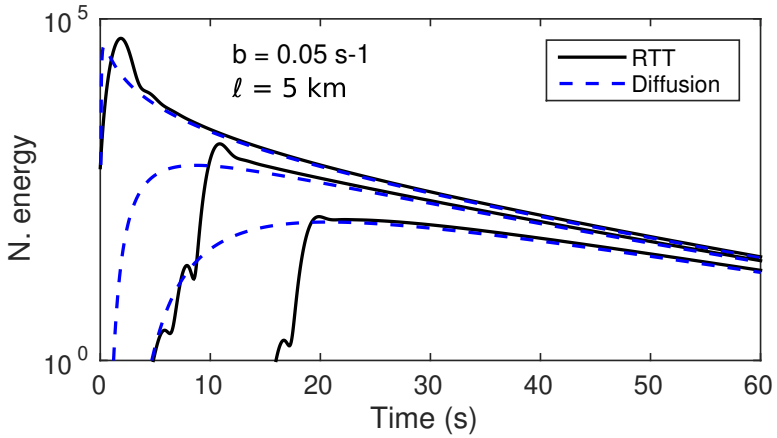

Figure 5.9: Convergence of radiative transfer envelopes (solid black line) towards diffusion approximation (dashed blue line). Envelopes were band-pass filtered at [0.5-1]Hz and correspond to a medium with $\ell = 5$km and $b = 0.05s^{-1}$.

propagation regimes in time and space is critical for the accurate estimation of attenuation properties. In this section we perform the separation of scattering and absorption mechanisms by using different inversion techniques: the first one, the MLTWA, which measures the energy decay with distance in different time windows; and secondly, we introduce a full-envelope based approach, in which we measure the b and ℓ consecutively in longer portions of the energy envelopes.

5.4.1 MLTWA

The MLTWA relies on the idea that different portions of the energy envelopes develop a predominant sensitivity to a given attenuation mechanism (Fehler et al. (1992); Hoshiba (1993)). For example, the first of the typical three 15 s-windows is expected to be strongly controlled by scattering, and the two consecutive windows are rather sensitive to absorption. By using this technique, we calculate the misfit between observations and RTT predictions by comparing the averages of normalized energy densities in three time windows of 15 s. The onsets of the three windows are 0, 15 and 30 s after the peak arrival. Since emergence of noise can occur at earlier lapse times for the 1 - 2 Hz and 2 - 4 Hz bands, we used 10 s window lengths. For these two cases, the average energies are computed at windows starting at 0, 10 and 20 s after the peak arrival. Since normalization of energy is fundamental in the implementation of MLTWA technique, in Fig. 5.10 we show the effect of coda normalization on the observed average energies. Not-normalized average energies (Fig. 5.10-top) experience a higher dispersion with distance in the three time windows, even though the decrease can still be observed. Such dispersion might be related to local site effects or to the influence of noise sources. By applying coda normalization, these effects are removed and the energy propagation can properly be reconstructed. Fig. 5.10(bottom) shows the ensemble of normalized average energies in the three time windows. Note that within the three windows normalized energy densities got closer to an exponential decrease, which might improve the quality of the measurements. In the first window, the normalized energy is some order of magnitudes larger than in $TW2$ and $TW3$ due to the influence of ballistic components, which also depicts a more pronounced decay with distance. In the other hand, time windows $TW2$ and $TW3$ shows how energy tends to get stable at long lapse times due to the proximity to the diffusion regime.

Note that MLTWA is a technique based on RTT, hence, in this subsection we do not use

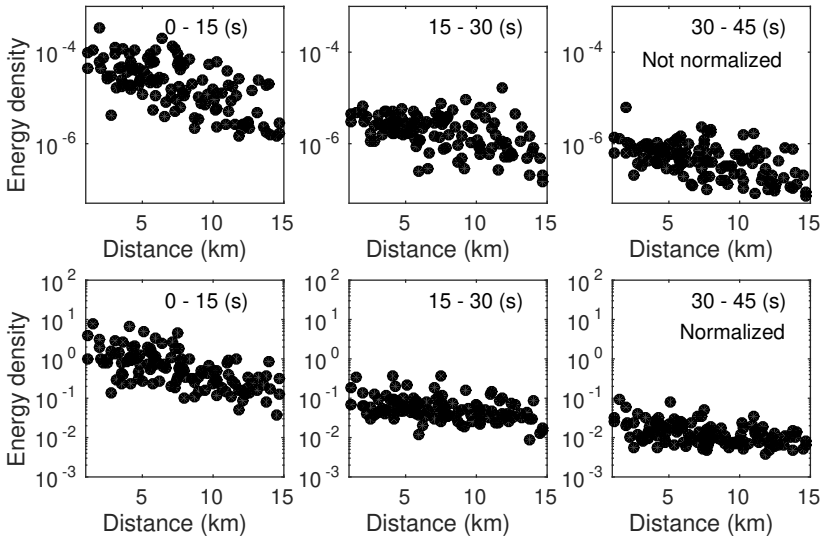

Figure 5.10: Effect of coda normalization on the spatio-temporal evolution of the observed mean energy. (Top) average energies in the three time windows before coda normalization and (Bottom) average energies after normalizing. The example corresponds to the causal part of the [0.5 - 1]Hz frequency band.

diffusion approximation to calculate synthetic envelopes. As mentioned before, attenuation measurements are performed in a 2D grid search in which observed and modelled normalized energy densities are compared. To quantify these comparisons we calculate the sum of the squared residuals between observations and predictions, which is given by:

$$SSR = \sum_{i=1}^{3} \sum_{j=1}^{M} \left[\log \left(\frac{E_{RTT}\left(t_i, j\right)}{E_{obs}\left(t_i, j\right)} \right) \right]^2 \tag{5.4}$$

Where E_{RTT} and E_{obs} are the modelled and observed average energy densities in the time window i for the station pair j. It is worth mentioning that, in order to improve the comparinsons between E_{RTT} and E_{obs} the same operations applied on the observed data must be applied on the predictions. This includes the time smoothing, the coda normalization and the band-pass filter effect (see Fig. 5.7).

In Fig. 5.11 we show the results of the grid search for all frequency bands and both sides of the CCFs. The color bar stands for different values of the sum of the squared residuals (SR) which were normalized with respect to the minimum (best fit); the red cross represents the best fit parameters of ℓ and b. The set of figures at the top are results for the causal part and those at the bottom correspond to the acausal part. Overall, absorption is significantly better constrained than scattering and not significant differences are observed between causal and acausal parts. In the other hand, scattering estimates are more variable, and large differences are observed between causal and acausal parts. In the case of the $[0.5 - 1]$Hz band, such differences are of the order of 75%, however, as frequency increases, the scattering discrepancies between both sides of the CCFs are less significant. This systematic mismatch evidences a possible effect of directivity (i.e. uneven distribution of noise sources) on scattering estimates with certain frequency dependence.

Table 5.1 summarizes the best-fit parameters of scattering ℓ and absorption b. To facilitate the discussion, we also present the results of absorption in terms of absorption length ℓ_a. This representation suggests that scattering dominates over absorption in the three frequency bands, which is expected for a volcanic context. This observation is consistent to what has been found

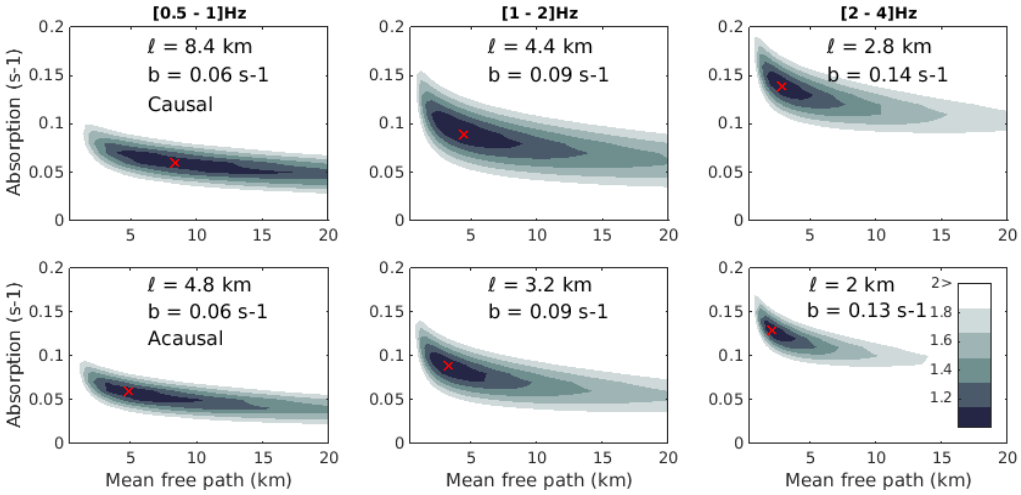

Figure 5.11: 2D grid search: Distribution of the sum of the normalized squared residuals (SSR) between the observed and modelled energy densities at [0.5 - 1], [1 - 2] and [2 - 4] Hz. The red cross indicates the best fit (minimum SSR) and the colormap stands for different ranges of SSR.

in other works in volcanic contexts (Wegler and Lühr (2001),Ugalde et al. (2010),Prudencio et al. (2015)).

Frequency band (Hz)	$\ell(km)$		$b(s^{-1})$		$\ell_a(km)$	
	Acausal $(-)$	Causal $(+)$	Acausal $(-)$	Causal $(+)$	Acausal $(-)$	Causal $(+)$
$0.5-1$	4.8	8.4	0.06	0.06	19.7	19.7
$1-2$	3.2	4.4	0.09	0.09	13.1	13.1
$2-4$	2	2.8	0.13	0.14	9.1	8.4

Table 5.1: Best-fit estimates of absorption and scattering parameters. Scattering is represented by the transport mean free path ℓ, and absorption expressed in terms of b parameter and as absorption length ℓ_a

In Fig. 5.12, we show the spatio-temporal evolution of the observed (black circles) and the modelled energy densities (red lines) for the causal part. Modelled energy densities were computed with the best fit parameters. Note that dispersion of observed data in the first window decreases with frequency, which could explain the higher accuracy of scattering estimates in the [1-2] and [2-4]Hz bands, with respect to [0.5-1]Hz. Similarly, the huge dispersion in [10-20] and [20-30]s windows at the [1-2]Hz band might explain the slightly lower accuracy of absorption in that frequency band. Moreover, the fact that the energy in the first time window in the [0.5-1]Hz is some orders of magnitude higher than in the two other windows, suggests a significant dominance of ballistic components. In contrast, for the [1-2] and [2-4]Hz bands, the energy at the first time window becomes closer to the long lapse time windows, which evidences a higher influence of diffused components due to the increase of scattering.

5.4.2 Full-envelope based approach

Through the former approach (MLTWA), attenuation mechanisms were measured based on the spatio-temporal evolution of seismic energy, and assuming that scattering and absorption are constant. Even though this method has widely been used in diverse geological contexts, the interpretation in terms of the level of accuracy in scattering estimates might remain ambiguous. To shed some light on this issue, we now perform ℓ and b estimations by inverting individually

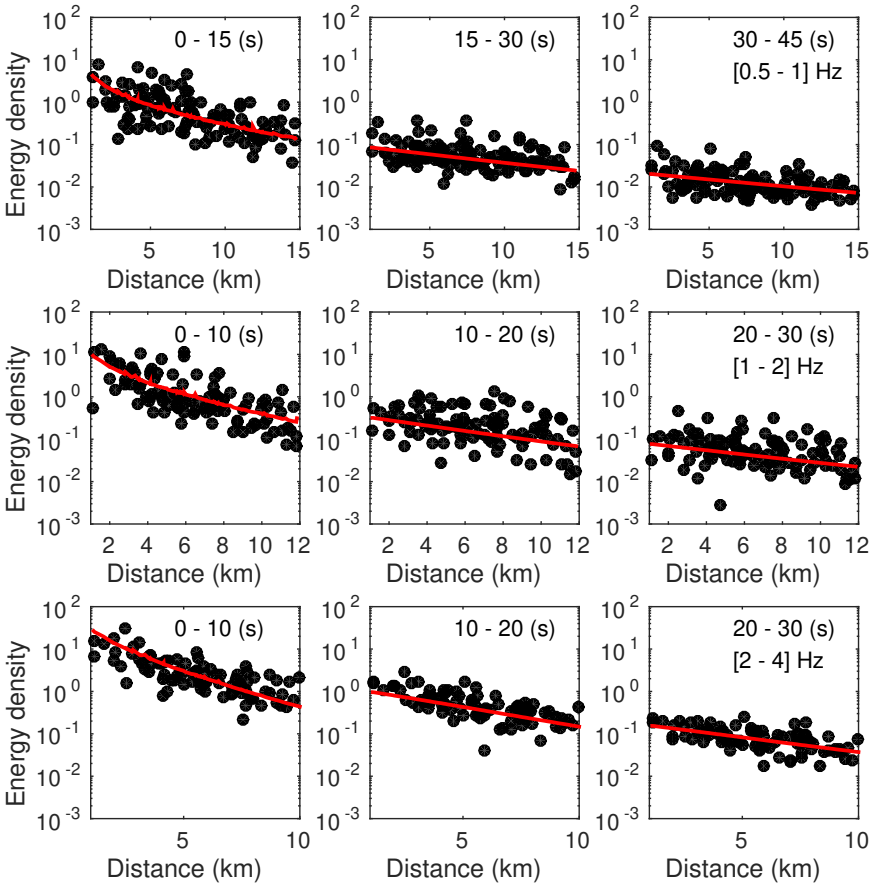

Figure 5.12: Comparisons between observed and modelled (RTT) energy envelopes for different propagation distances. Results are shown for 0.5 - 1, 1 - 2 and 2 - 4 Hz bands and for the ensemble of epicentral distances. Black dots corresponds to the observed envelopes and the red lines are the radiative transfer theory solution. These results correspond to the causal parts of the CCF.

each energy envelope. Additionally, we search to exploit the integrality (in time) of the energy envelopes as much as the SNR allows it. As shown in Fig. 5.8, long propagation distances become more sensitive to scattering, whereas the effects of absorption are independent on distance. Furthermore, the lapse times at which amplitudes of the energy envelopes merges into the noise, suggests that coda duration is inversely proportional to distance (see Fig. 5.6(a)). In order to profit of this dynamics, in this section we propose a technique to estimate scattering and absorption in two stages: (i) b is measured by using short propagation distances and also auto-correlation functions (zero-offset case). Thus, we fix a constant value of absorption which is then used as an input for the (ii) estimation ℓ at longer propagation distances.

Absorption

Initially, we consider CCFs with propagation distances up to 8 km in the [0.5 - 1]Hz band. In this range of distances, we exploit the coda up to 80(s) (also used as reference window) in order to measure absorption attenuation. Since diffusion approximation can properly simulate the distribution of energy at long lapse times, we use both models: RTT and diffusion approximation. Observations and predictions are compared by using all the points of the record, from the arrival time to the reference window. For a given propagation distance (station pair), the misfit between

observed and modelled envelopes is given by:

$$SR = \sum_{t=t_0}^{t_f} \left[\log \left(\frac{E_{RTT}(t)}{E_{obs}(t)} \right) \right]^2 \tag{5.5}$$

Where t_0 and t_f represent the bounds of the misfit operation, from the arrival time to the reference window, respectively. By choosing the best-fit parameters we find the corresponding b and ℓ parameters for a specific path. Note that, at this point, the estimation of ℓ is not relevant as our distance range is not so sensitive to such parameter. In Fig. 5.13 (top) we show an example of absorption estimate for a receiver couple with propagation distance of approximately 4 km. This inversion was performed by using both, RTT and diffusion models, and we found exactly the same misfit distribution. Note that for both sides of CCF, absorption is well constrained, and unsurprisingly, the estimation of ℓ is not accurate. This result is not necessarily undesirable since the estimated absorption parameter might still represent a solution for the whole range of search of ℓ (to be measured in the next section). Fig. 5.13 (bottom) shows a comparison between the observed and synthetic envelopes, the latter was obtained with the best-fit absorption parameter. The thin grey lines indicate the region at which the fitting procedure was performed. Note that after certain lapse times the agreement between RTT (red) and diffusion approximation (blue) is perfect.

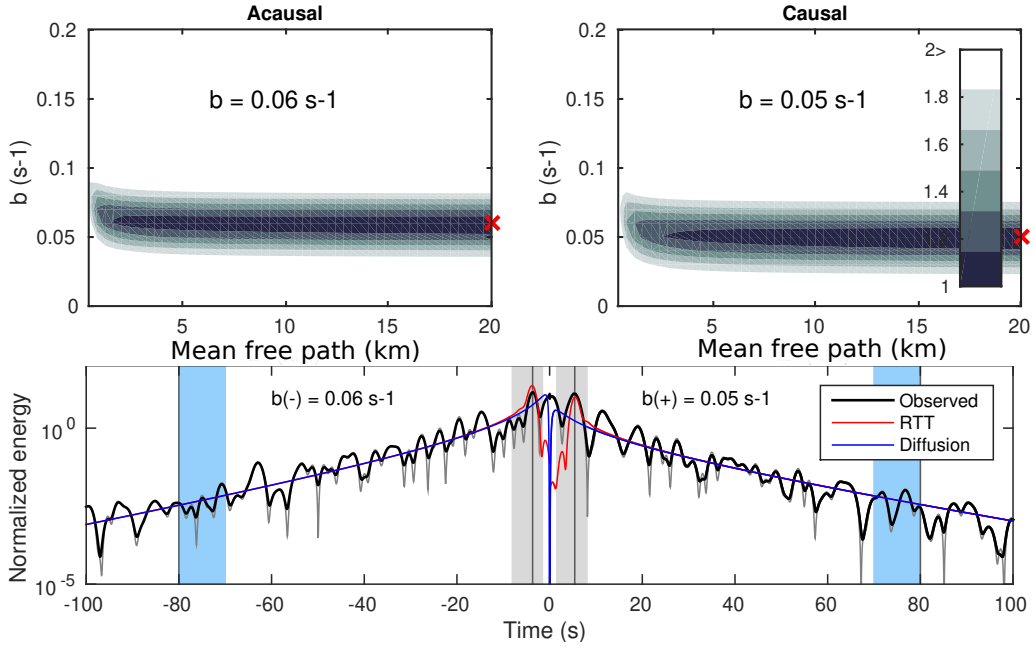

Figure 5.13: Individual estimation of absorption parameter at a short propagation distance. (Top) the 2D grid searches with the normalized squared of residuals. Results are shown for both, causal and acausal parts of the CCF's energy envelope; (Bottom) Comparison of observed energy envelope and the best fit-synthetic envelope when using RTT (red) and diffusion approximation (blue). Thin grey lines bound the exploited portion of the energy envelope. Cases [0.5-1]Hz and propagation distance of 4 km.

The global best-fit absorption parameter could be found by minimizing the sum of Eq. 5.5 over the ensemble of receiver couples and including only the envelopes with coda duration longer than 80(s). Since in the distance range of interest absorption behaves independent on scattering (see Fig. 5.13 top), in what follows we present SSR plots only as a function of b. The global

measurements, presented in Fig. 5.14(top-left), illustrate an excellent resemblance of residual distributions between RTT and diffusion approximation. Moreover, these estimates are pretty similar to those obtained from the MLTWA, which are slightly larger. Such discrepancies are possibly due to the fact that in the MLTWA the duration of the exploited coda is shorter, with potential influence of direct wave arrivals.

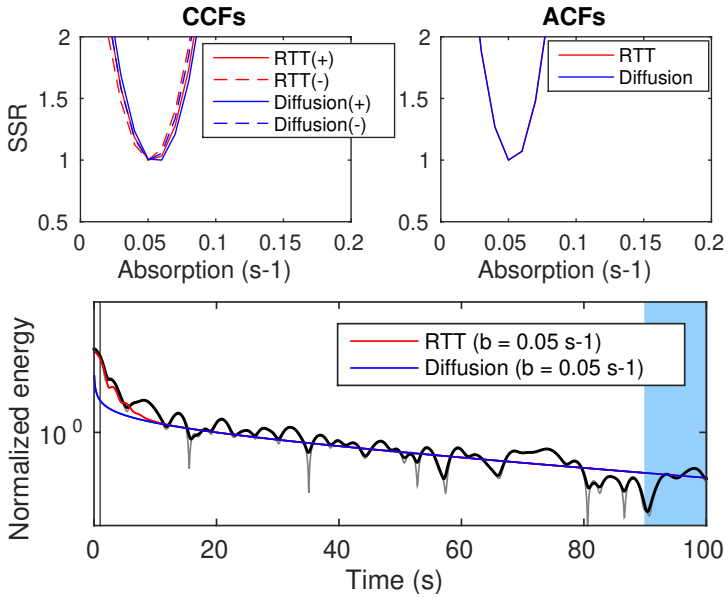

Figure 5.14: Global estimates of absorption parameter. (Top) misfit functions of b parameter from cross-correlation (top-left) and auto-correlation functions (top-right), by using both, RTT (red) and diffusion approximation (blue); (Bottom) example of observed ACF and its synthetic counterpart from the best-fit parameters of RTT and diffusion approximation. Case [0.5-1]Hz.

Since short propagation distances exhibit a longer coda duration, we now explore the auto correlation functions (ACFs), which represent the zero-offset case. Even though the peak amplitude of ACFs just represent the recorded noise level at the station (Stehly and Boué (2017)), the long lapse time components can exhibit a similar decay to those from CCFs (Soergel et al. (2019)). In this way, absorption attenuation is measured from ACFs, to do so, we use receivers with coda duration of minimum 100(s) in the [0.5 - 1]Hz band, and 85 and 70(s), for the [1 - 2] and [2 - 4]Hz bands, respectively. In Fig. 5.14(c) we show an example of auto-correlation in the [0.5 - 1]Hz band. Both, RTT and diffusion approximation are used, and excellent agreement between these to models is found. Global estimates for the ensemble of frequency bands are shown in Fig. 5.14(b).

Model	$b(s^{-1})$		
	[0.5 - 1]Hz	[1 - 2]Hz	[2 - 4]Hz
RTT	0.05	0.08	0.11
Diffusion approximation	0.05	0.08	0.11

Table 5.2: Global best-fit estimates of absorption when using ACFs (r = 0 km). best-fit parameters were obtained from RTT and diffusion models at the the three frequency bands.

Note that, since our technique allows us to measure absorption attenuation at each energy envelope, either from CCFs or ACFs, it results convenient to visualize lateral variations of this

parameter from ACF's estimates. The variations of absorption attenuation are shown in Fig. 5.15 for the three frequency bands. Same as in Table. 5.1 b parameter is converted into absorption length ℓ_a.

At low frequency ($[0.5-1]$Hz), ℓ_a lateral variations seem to exhibit two main signatures: near the volcanic summit absorption is stronger (shorter ℓ_a), and it decreases at regions far from it.

This pattern is certainly consistent with the phase velocity maps obtained by Mordret et al. (2015) at the PdF volcano. By using seismic noise data recorded over 4 years, in a range of periods (frequency) between 0.6 (1.7) and 5s (0.2 Hz), they found lower values of Rayleigh wave velocity near the summit than in regions far from it. A second signature on the lateral variations of absorption estimates exhibits some heterogeneity at stations right above the volcanic summit (red ellipse), in which, for one of the receivers, absorption is significantly lower than those surrounding the summit. This behavior might be consistent with the works of Prôno et al. (2009) and Lénat et al. (2012) who reported the presence of a high velocity zone under the summit. They interpret this anomaly as the result of small magma cooled body emplaced at shallow depth. The surrounding low velocity area near the crater (possibly correlated with our higher absorption estimates) could be related to the high fracturation and presence of lava flows, also reported by Prôno et al. (2009). In contrast to this pattern at low frequency, our estimates at $[1-2]$ and $[2-4]$Hz bands, exhibit spatial variations that seem to be less correlated with the subsurface geology of the volcano. Mayor et al. (2016) suggest that coda waves may become more sensitive to deeper structures as frequency increases due to the higher proportion of body waves compared to surface waves at high frequency. Based on this hypothesis we might expect that the observed space variations of absorption at high frequency might be controlled by deeper structures. Also note that the dispersion of ℓ_a values is smaller at high frequency.

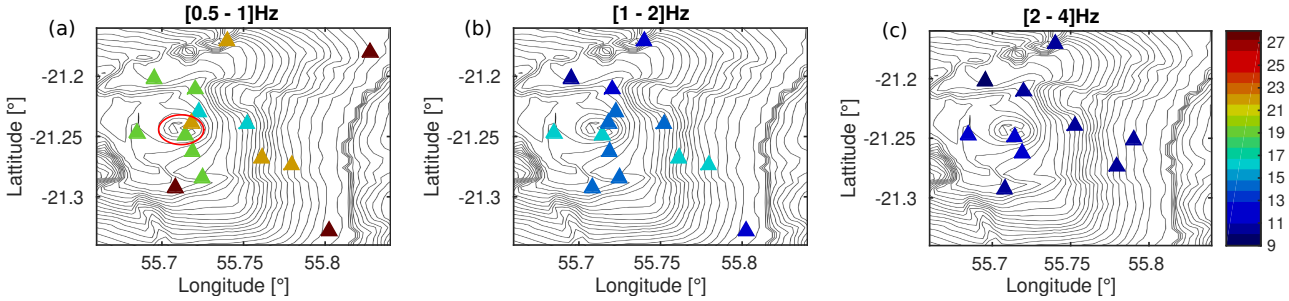

Figure 5.15: Lateral variations of absorption parameter (absorption length ℓ_a in km) from individual measurements when using ACFs. Results are shown for the three frequency bands: (a)[0.5-1]Hz, (b)[1-2]Hz and (c)[2-4]Hz. The colormap stands for different values of ℓ_a. The number of stations gets reduced with frequency as coda duration decreases. The red ellpise indicates the volcanic summit

Scattering

The second step of the full-envelope based approach consists in estimating scattering from receiver couples with sufficiently long propagation distances. Absorption attenuation is now a fixed parameter, whose values are shown in Table. 5.2. The range of propagation distances for scattering estimation is chosen as 8 - 15 km at the [0.5 - 1]Hz frequency band, and those for the [1 - 2] and [2 - 4]Hz bands are chosen as 4 - 12 km and 4 - 10 km, respectively. Our strategy is based on the Q_{open} method whose basis were initially proposed by Sens-Schönfelder and Wegler (2006b) and largely applied not only to constrain attenuation properties but also to estimate source and site amplification parameters (Eulenfeld and Wegler (2016); Eulenfeld and Wegler (2017); Ranjan

and Konstantinou (2020) van Laaten et al. (2021)). As shown in the analyses of modelled energy envelopes (see Fig. 5.8), for a wide range of mean free paths, early lapse time components are more sensitive to scattering than the late coda. Thus, for a more accurate estimation of ℓ, the inversion procedure will be performed by comparing amplitudes at early lapse times. As reported by Sens-Schönfelder and Wegler (2006b), RTT can not take into account several effects occurring at the ballistic pulse, such as peak broadening and wandering effects. These discrepancies in the characteristics of the ballistic pulse can complicate the comparisons between the modelled and observed energy envelopes. To circumvent these difficulties they propose to average the energy contained in a short window around the ballistic pulse. In our case, we use the average energy contained in a first window with duration $2T_0$ (T_0 is the central period at given frequency band) starting at the peak amplitude. In contrast to Sens-Schönfelder and Wegler (2006b) and the previously mentioned works, we use a second window with a larger size (8 seconds), in which energy is also averaged. The reason to use a second window is the high sensitivity of the early coda to scattering. The total duration of our early regime (including the two windows) is in agreement to what van Laaten et al. (2021) suggest, who mention that, depending on the investigation area, the early components window should have a duration between 4 and 10s since it must contain both, ballistic and the early forward scattered waves. In this way, our inversion technique for scattering will make use of two points representing early lapse time, which are expected to be highly sensitive to scattering: the ballistic and early diffused fields.
In a first attempt to estimate ℓ from the full-envelope based approach, we search to fit modelled to observed envelopes by comparing average energies in the two windows. Fig. 5.16 (Top) shows an example of normalized energy envelope, in which the vertical grey lines bound the two windows where average energy is computed. At this point, the misfit function for a given receiver couple, takes a similar form to the one of the MLTWA:

$$SSR = \sum_{w=1}^{2} \left[\log \left(\frac{E_{RTT}(t_w)}{E_{obs}(t_w)} \right) \right]^2 \tag{5.6}$$

Where w is a given window in which energy is averaged. For the example in Fig. 5.16 (Top), the synthetic envelopes from the best-fit parameters are also shown with the previously fixed absorption $b = 0.05(s^{-1})$ in the [0.5-1]Hz band. The ensemble of individual measurements are shown in Fig.5.16(b,d an f) for all the azimuths and frequency bands. The circles (crosses) correspond to the causal (acausal) part of CCFs and the colors denote the corresponding signal-to-noise ratio.

The azimuthal distribution of ℓ shows that the variability is higher for receiver couples with azimuths near the predominant direction of the noise sources (270^o), most of them belonging to the causal parts (circles) of CCFs. On the other hand, measurements from acausal parts (crosses) exhibit a lower variability. This behavior also implies certain degree of proportionality between the SNR and the transport mean free path. A global estimation of scattering (Fig. 5.16b-g) can be performed by fitting the ensemble of energy envelopes through the sum of expression 5.6 over all the paths. We show global estimates for the causal (black line) and acausal (red line) parts of the CCFs at the three frequency bands with significant discrepancies between them. The lower accuracy in the causal part can be explained by the huge variability of individual measurements ℓ near the dominant direction of the noise sources. Same as with the MLTWA, the accuracy of the global scattering estimates increases with frequency. The ensemble of individual measurements might indicate that the azmuthal dependence of the SNR (which is also frequency dependent as shown in Fig. 5.5) can strongly affect the accuracy of scattering estimates.

Results shown in Fig. 5.16 evidence how well the individual measurements of scattering can help to interpret the level of accuracy of the global estimates. However, the observed azimuthal and SNR dependence of ℓ might be contaminating the actual propagation properties of the investigation area. To circumvent this difficulty, we shall modify our fitting procedure by using a different observable. Thus, we perform the ratio of energy between the ballistic and early diffused fields utilized previously. We rely on the idea that the ratio of observed average energies in the early regimes may cancel the influence of noise directivity, as both windows might contain such effects. Furthermore, this observable is consistent with the physics of waves in heterogeneous media since the ratio between the ballistic and diffuse fields is an indicator of the redistribution of energy due to scattering. We refer to this inversion technique for scattering as "Ball-diff" (ballistic to diffusive) ratio, which misfit function is given by:

$$SR = \log \left[\frac{C_{RTT}}{C_{obs}} \right]^2 \tag{5.7}$$

Where $C_{RTT} = E1_{RTT}/E2_{RTT}$ and $C_{obs} = E1_{obs}/E2_{obs}$, with E1 and E2 being the average energy contained in the ballistic and early diffuse windows, respectively. Thus, Eq. 5.7 could be rewritten as:

$$SR = \log \left[\frac{E1_{RTT}E2_{obs}}{E2_{RTT}E1_{obs}} \right]^2 \tag{5.8}$$

In Fig. 5.17 (Top) we present the same case of energy envelope as in Fig. 5.16 in the [0.5-1]Hz. Here, the envelope is normalized with respect to the average energy contained in the early diffused field window (TW_2). Note that for this example, the value ℓ in the causal part of CCF is reduced, from 9.6 km in the average energy-fit procedure to 6.6 km when using the "ball-diff" technique, thus reducing the difference with the acausal part. The ensemble of individual measurements of the whole set of receiver couples are shown in Fig. 5.17(b) ([0.5-1]Hz), where the variations of ℓ around 270^o are significantly smaller than those in Fig. 5.16(b). Similarly, the global misfit functions 5.17(c) evidence that scattering measurements of the causal and acausal parts are much closer, as well as significant increase of accuracy in the estimates of the causal part. The same type of improvement is observed at higher frequencies (see Fig. 5.17 d-g).

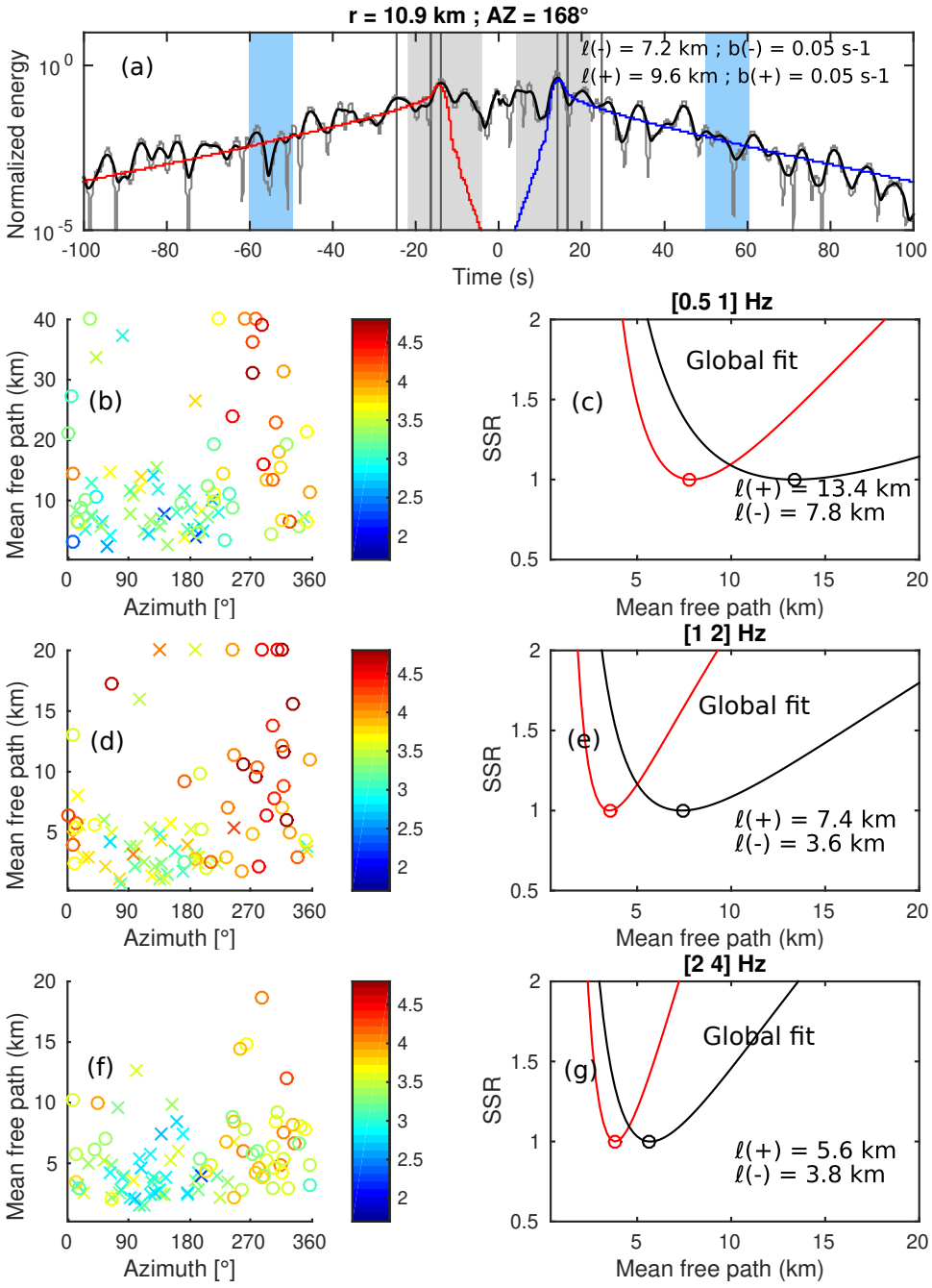

Figure 5.16: Scattering estimates from the fitting of average energies at early lapse times for long propagation distances. (a) Example of observed energy envelope and best-fit synthetic envelope at the [0.5-1]Hz; (b), (d) and (f) ensemble of individual measurements at the three frequency bands and their azimuthal dependence: circles and crosses correspond to the causal and acausal parts of the CCFs, respectively, and colors represent their SNR of each energy envelope; (c), (e) and (g) global fit of ℓ for causal (black) and acausal (red) parts of the CCFs.

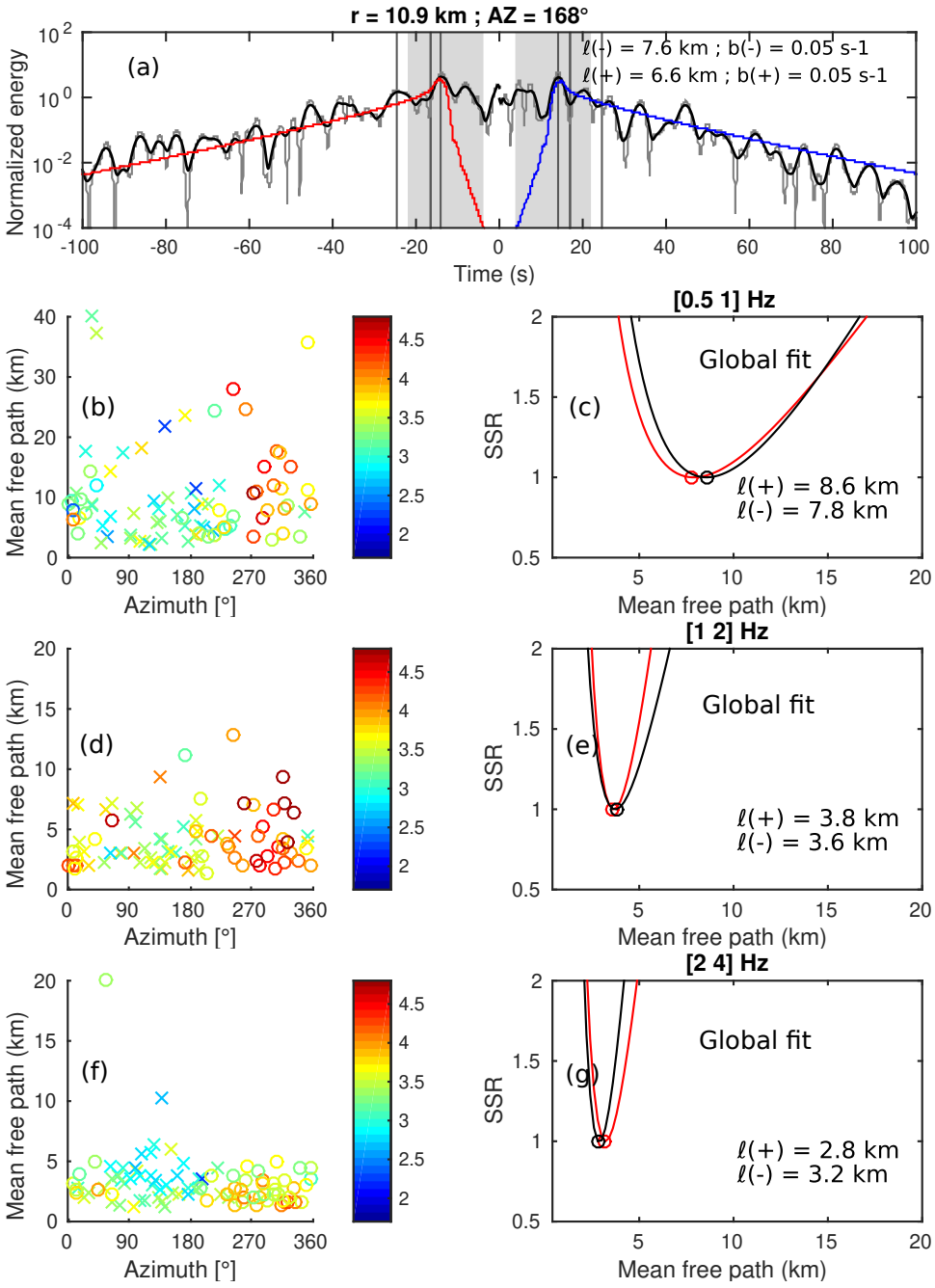

Figure 5.17: Same as Fig.5.16 for the ball-diff ratio technique.

5.4.3 Comparing MLTWA with the Full-envelope based approach

Besides reducing the effect of noise directivity in scattering estimates, the proposed "ball-diff" ratio technique does not require the coda normalization step. This last fact represents a reduction in the number of choices on the energy envelope processing. Thus, it avoids that attenuation measurements could be biased by any assumption regarding the reference window for the coda normalization (see Heller et al. (2022)). In contrast to the ball-diff ratio technique, the so known MLTWA method is strongly dependent on the coda normalization as it is based on the spatio-temporal distribution of the energy ratio. van Laaten et al. (2021) performed some comparisons between estimates obtained from the MLTWA and Q_{open} method by using earthquake data. These authors found good agreement in terms of the absolute values of both attenuation mechanisms over their whole range of frequencies (from 3 to 34 Hz). They found small discrepancies in terms of the error magnitudes, with a higher accuracy for the Q_{open} method. In a similar way as van Laaten et al. (2021), we compare our attenuation estimates between MLTWA and the full-envelope based approach.

In Fig. 5.18 we present the global estimates of absorption and scattering parameters as a function of frequency and their corresponding error bars, obtained from the two approaches in both, causal and acausal parts. Error bars were obtained as the range of parameters ℓ and b at which the normalized SSR is smaller than 1.1. Overall, there is good agreement between MLTWA (black circles) and the full-envelope based approach (blue circles): absorption estimates (top panels) are very similar, with systematic difference in terms of their absolute values. Estimates of MLTWA are slightly higher than those from the FEBA, such systematic differences are possibly related to exploited duration of the coda window, which is shorter in the MLTWA.

In terms of scattering, there is a good agreement between both approaches, with higher discrepancies in the acausal part. Such differences could be related to the possible noise directivity effects in the MLTWA, which in contrast to the "Ball-diff" technique were not cancelled. Results when using the causal part (right side of the panel) evidence an excellent agreement between both approaches in terms of absolute values of scattering estimates. In the other hand, error bars are significantly smaller in the Ball-diff approach than in MLTWA, and this might be due to two reasons: (1) the restriction of ℓ measurements to long propagation distances expected to be highly sensitive to scattering in the "ball-diff" ratio technique; and (2)the chosen early regime composed by two windows (ballistic and early diffused fields) migh have a higher sensitivity to scattering than the 15 s window in the MLTWA. The latter might contain a mix of scattering regimes.

A comparison of observed energy envelopes and the best-fit envelopes from both approaches is shown in Fig. 5.19. These results are shown just for causal estimates and causal observed energy envelopes as this data set presents a better agreement between the two approaches. Overall, both methods can properly describe the distribution of energy in the study area.

5.5 Validation of the method: comparisons with results using earthquake data

The above measurements of scattering and absorption attenuation through the full-envelope based approach are numerically robust, as their corresponding error bars are small and the absolute values of b and ℓ have good agreement with those from the MLTWA method. As expected, estimates on absorption attenuation are more accurate than those on scattering. However, in order to properly validate our technique, we perform the same type of measurement, by using the same approach, on earthquake data. In their pioneering work, Hirose et al. (2019) compared measurements of absorption and scattering from seismic noise with those from active shots, obtaining very

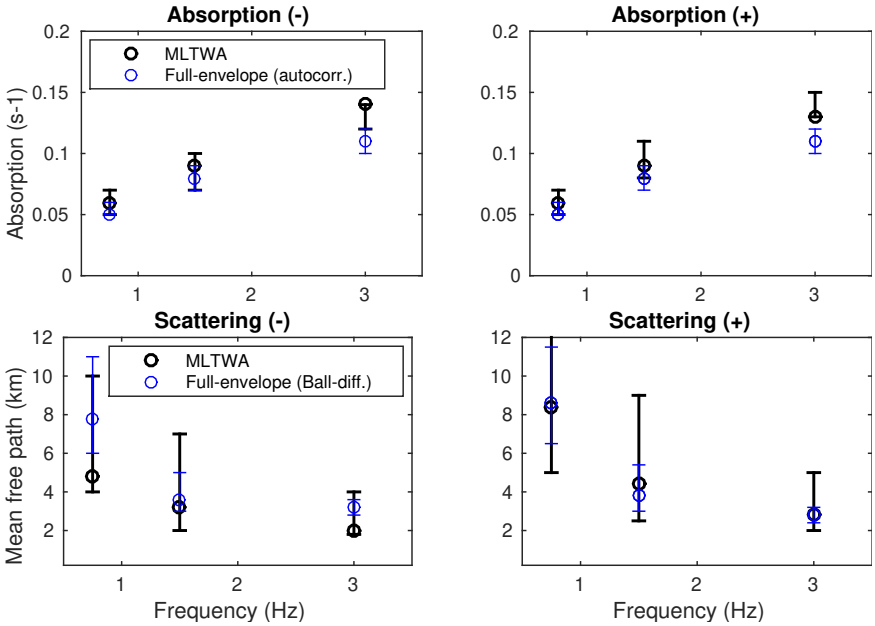

Figure 5.18: best-fit attenuation estimates of MLTWA (black) versus the Full-envelope based approach (blue). (Top) absorption estimates and associated error bars: black circles correspond to the MLTWA and the blue ones are the full-envelope based approach (FEBA). Left and right sides represent the acausal and causal parts, however for the b estimates of FEBA only ACFs were used (no distinction between causal and acausal parts), but they are compared with the two sides of MLTWA measurements. (Bottom) scattering estimates.

similar results. In the present work, we perform comparisons with local earthquakes in the PdF volcano, whose magnitudes range between 1.5 and 2.5, with reported depths of approximately 0 km. These shallow volcano-tectonic events often occur under the Dolomieu crater, just above the potential location of a shallow magma reservoir (Peltier et al. (2009) Prôno et al. (2009) Duputel et al. (2022)). The structure to which these earthquakes are associated, corresponds to a ring-fault system at the summit caldera (Duputel et al. (2022)). The almost negligible depth and the short epicentral distances allow us to consider the generated wavefield as dominated by surface waves. Thus, same as with the noise-based measurements, we might be able to use the RTT solution for surface waves shown in Sec. 5.3 (see Eq. 5.2). The spatial distribution of earthquakes and seismic stations can be found in Fig. 5.22(see supplementary material). Epicentral distances are similar to those from the seismic noise part. In Fig. 5.20 we show an example of seismic wavefield for an earthquake with $M_d = 2.0$, in which we present the waveforms at different distances as well as their corresponding Fourier amplitude spectra. This figure gives also an idea about the energy content in the frequency bands of interest ([0.5-1],[1-2] and [2-4]Hz). While most of the energy content in the low frequency belongs to noise sources, higher frequencies are richer in earthquake energy. However, we shall limit our earthquake-based measurements to 4 Hz: first, because comparisons with noise results must be performed in the same range of frequencies ([0.5 - 4]Hz), and secondly because higher frequencies might be dominated by body waves Nakata et al. (2016).

Following the same procedure as the one used for the noise-based measurements, seismograms are filtered in three frequency bands ([0.5-1],[1-2] and [2-4]Hz), and energy envelopes are calculated by using the Hilbert transform of the filtered seismograms. The same selection criterion is applied:

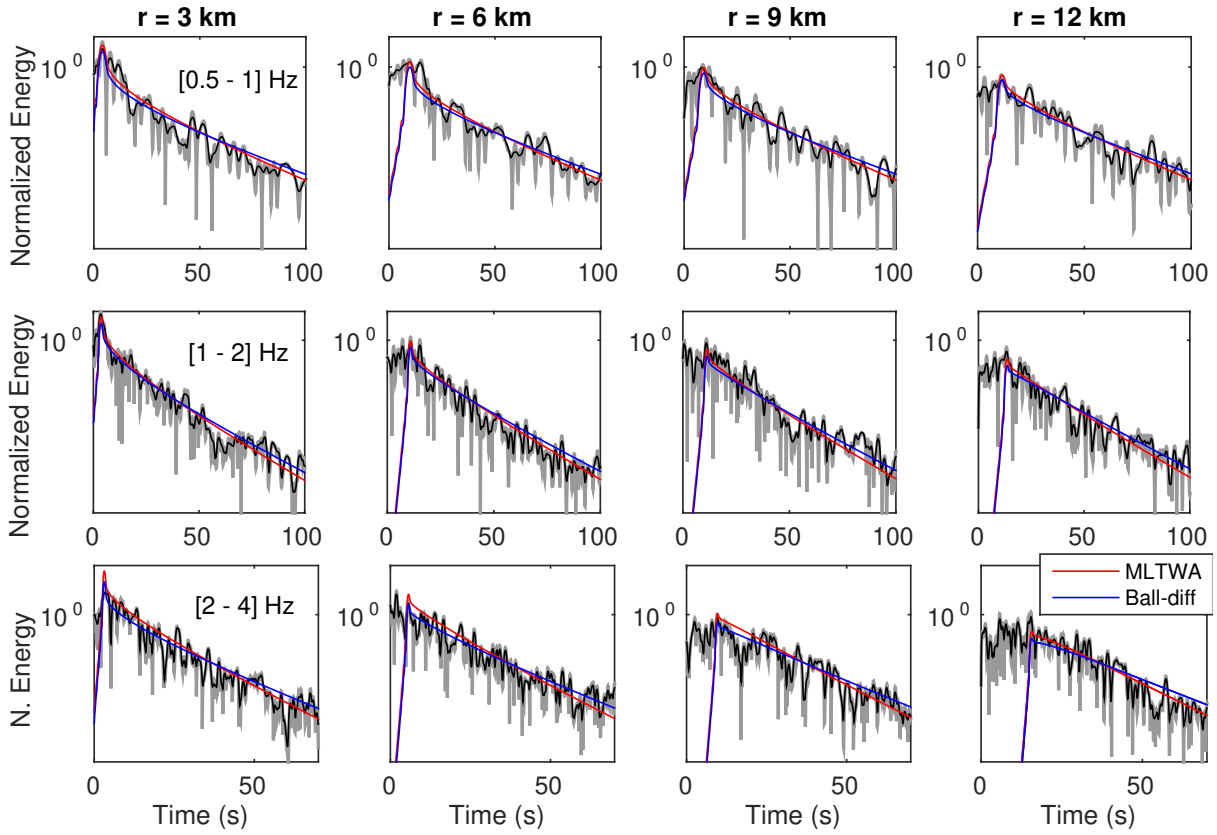

Figure 5.19: Comparing observed (black lines) and best-fit synthetic energy envelopes from both approaches: MLTWA (red) and full-envelope (blue). Results are shown for different propagation distances from 3 to 12 km. The grey lines correspond to the not-smoothed observed envelopes. For comparison purposes envelopes were normalized by the total energy contained in 5-seconds windows at 60, 50 and 50(s), respectively.

only envelopes with SNR higher than 4 were considered. Fig. 5.23 (in supplementary material) shows the ensemble of selected energy envelopes for all the earthquakes. Note that, unlike the CCF envelopes, the coda duration of these earthquake data increases with frequency, which makes difficult the use of [0.5 - 1]Hz envelopes as most of coda lengths tend to be shorter than 15(s). For this reason, we shall perform the b and ℓ measurements only in [1 - 2] and [2 - 4]Hz bands. Following the full-envelope based approach described in section 5.4.2, absorption is estimated from envelopes with short epicentral distances, in this case we use distances shorter than 2 km for both frequency bands. After fixing absorption, scattering is estimated from longer propagation distances ($r > 4$ km).

Examples of individual estimates of absorption and scattering, in the [2 - 4]Hz band, are shown in Fig. 5.21(a) and (b), respectively. Subfgures 5.21(c) and (d) show the global measurements for the same frequency band. Note that, same as in the noise-based estimates, absorption is measured at short distances in order to have a longer coda, but also the misfit distribution is completely parallel to the ℓ axis, which evidences the low sensitivity of short propagation distances to scattering attenuation. On the other hand Fig. 5.21(d) shows a well constrained estimation of ℓ when using larger propagation distances once b is fixed. These estimates are not far from what we obtained in the previous section ($b = 0.11(s^{-1})$ and $\ell = 2.8$ km). To facilitate the discussion we summarize the ensemble of results in Table. 5.3 for the [1 - 2] and [2 - 4]Hz.

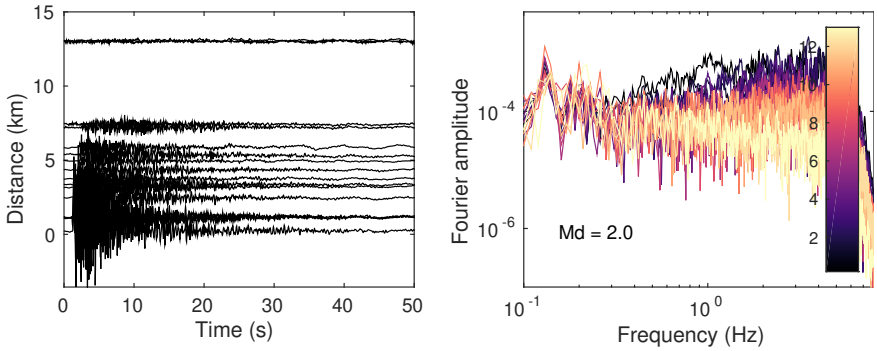

Figure 5.20: (Earthquake data. Example of (left) recorded seismograms at epicentral distances between 0.1 to 14 km for an earthquake with magnitude 2.0 and its (right) Fourier amplitude spectra where the colors denote different epicentral distances.

Frequency band (Hz)	$\ell(km)$		$b(s^{-1})$	
	Earthquake	Noise	Earthquake	Noise
$1-2$	**3.2** [2.8 - 4.0]	**3.8** [3.0 - 5.4]	**0.08** [0.06 - 0.09]	**0.08** [0.07 - 0.09]
$2-4$	**2.6** [2.6 - 3.0]	**2.8** [2.4 - 3.2]	**0.11** [0.10 - 0.12]	**0.11** [0.10 - 0.12]

Table 5.3: Comparisons of global estimates of absorption and scattering from earthquake data and noise correlated signals. Noise-based estimates were obtained from the full-envelope based approach.

Overall, attenuation estimates from earthquake data are in good agreement with those from seismic ambient noise. The agreement of absorption parameters is better than that from scattering estimates. Even though, for both cases, errorbars are relatively small, unsurprisingly the accuracy when using earthquake data is higher. This might be due to the lower uncertainty in the ballistic regime. These similarities demonstrate the feasibility to retrieve attenuation properties from seismic ambient noise similar to those observed with earthquake data.

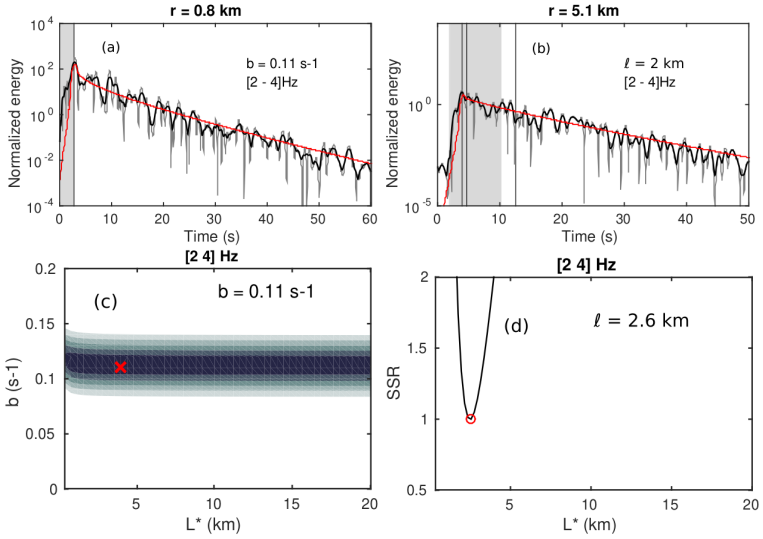

Figure 5.21: Attenuation estimates from earthquake data. Example of individual estimate of (a)absorption with short epicentral distances and (b)scattering at long epicentral distances; global fit of (c)absorption and (d)scattering. Example is shown for the [2-4]Hz frequency band.

5.6 Conclusions

We performed measurements of absorption and scattering properties at Piton de la Fournaise volcano by using energy envelopes of noise correlated signals. These measurements were performed first, by using the so known multiple lapse time window analyses (MLTWA) in which ℓ and b were estimated based on the spatio-temporal evolution of energy in three time windows. As expected for volcanic contexts, results exhibit that scattering attenuation dominates over absorption. The low accuracy of scattering estimates (specially at [0.5 - 1]Hz band), as well as the discrepancies between the causal and acausal parts of the CCFs, evidence the influence of possible effects of noise directivity; In order to better understand the level of accuracy of the attenuation estimates, we introduced a full-envelope based approach that allows to perform measurements at each energy envelope. Our approach takes into account, separately, the distance dependence of absorption and scattering effects on the shape of the energy envelopes. Thus, the estimates were performed in two stages: (i) absorption was measured by using short propagation distances and (ii) scattering was estimated from long propagation distances. In addition to the short propagation distances, we used auto-correlation functions (ACFs) which represent the zero-offeset cases. Obtaining localized absorption measurements enabled us to observe lateral variations of this parameter. The frequency dependence of the mapping exhibit lateral variations that are, in some extent, correlated with some previous geological and geophysical studies on the volcano. At higher frequencies these geological signatures are not so evident possibly due to the sensitivity of coda waves to deeper structures.

Scattering attenuation was measured at long propagation distances. We proposed a technique based on the ratio between the ballistic and early diffuse fields. Our technique shows a significant reduction of the effect of uneven distribution of noise sources on scattering estimates, as well as a higher accuracy on the estimation of this parameter. Results from both approaches (MLTWA and full-envelope) were compared in the three frequency bands and using the causal and acausal parts of the CCFs. We found good agreement specially for for absorption parameter. The comparisons also evidence the higher level of accuracy in scattering when using the ball-diff ratio technique. A potential advantage of our full-envelope based approach is the possibility to perform absorption and scattering tomography since results from individual energy envelopes can be visualized. In contrast, tomography studies based on the MLTWA would require dense and large seismic networks (e.g. Carcole and Sato (2010)) since several sub-regions of constant scattering must be considered to observe lateral variations.

In order to validate our method, we compared the noise-based estimates with those from earthquake data. We found excellent agreement in the [1 - 2] and [2 - 4]Hz frequency bands. Regarding the low frequency range, we were not able to perform attenuation measurements due to the low SNR. This last observation represents an advantage when measuring attenuation properties at a local scale by using seismic noise, since it offers the possibility to work at lower frequencies.

The isotropic scattering assumption in noise-based studies can give reliable estimates on the attenuation of quasi-ballistic waves in highly heterogeneous media. However, in order to obtain a more detailed estimation on the small-scale structures, future noise-based studies of scattering and absorption mapping should be performed under the anisotropic assumption. Such more realistic model might allow to observe more complex propagation characteristics on the ballistic regime as well as the access to other scattering parameters such as the scattering mean free path.

5.7 Supplementary material

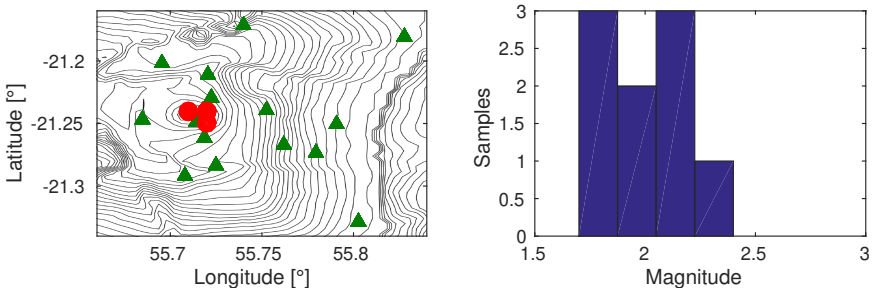

Figure 5.22: (left)Spatial distribution of earthquakes (red circles) and seismic stations (green triangles) in the study area; (right)Histogram of earthquake magnitudes

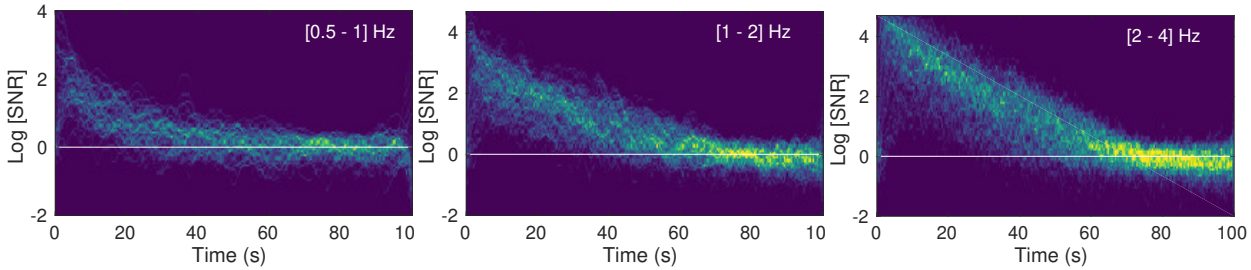

Figure 5.23: Ensemble of envelopes of the earthquake data, for the three frequency bands ([0.5-1], [1-2] and [2-4] Hz). Amplitudes are expressed as the logarithm of the signal-to-noise ratio (SNR). The white horizontal line represents the noise level; the colormap indicates the density of data at given amplitude and time

Chapter 6

Conclusions and perspectives

While the relevancy of seismic attenuation has been widely recognized, either to investigate the inner structure of the earth or to estimate the earthquake ground motions, its characterization and interpretation at small scales still remains ambiguous. In this work we presented a comprehensive study on the attenuation of seismic waves in highly heterogeneous media. We made use of full-wave simulations, phenomenological models and seismic noise data. Thus, our work was globally composed in two phases.

6.1 SH wave attenuation in 2D scattering media

First, we studied the propagation of SH waves in scattering media by using 2D numerical simulations in a range of frequency up to 5 Hz. Several random media with different perturbation levels were considered, each of them with 180 realizations. In order to simplify the interpretations of the amplitude decay, absorption was not included. Additionally the source was given by a Dyrac type incident plane wave so that geometrical spreading was not considered. We studied independently the coherent wave and the energy envelopes, which allowed us to understand the role of the two main length-scales controlling the seismic scattering: the scattering mean free path (ℓ) and the transport mean free path (ℓ^*). By comparing predictions from numerical simulations with those from the meanfield and radiative transfer theories, we verified the accuracy of the modelled wavefield, as well as the potential of these theories to predict the transport and decay of energy in a wide variety of scattering regimes. We paid particular attention on the peak energy evolution with distance, which is a key parameter in the context of seismic hazard assessment. Previous studies had shown that classical distributions, such as log-normal and exponential can properly describe the statistical fluctuations of the mean intensities when the wavefield is dominated by coherent components or by multiply scattered waves, respectively. Our analyses showed that there is a critical distance at which a crossover from log-normal to exponential distribution occurs and it is related to the influence of forward scattered waves in the peak energy. Furthermore, we found that for several cases, there is a coincidence between such critical distance and the scattering mean free path. This last point is one of the most striking results of this work, since it suggests an alternative way to constrain the scattering mean free path based on the statistical fluctuations of the peak energy. An additional implication of this result concerns the context of seismic hazard assessment, since a previous knowledge on the scattering properties (ℓ) might indicate the appropriate distribution for the prediction of peak ground motions.

The use of the statistical analyses demonstrated the incoherent character of the so-called 'ballistic' peak after certain distances. While previous works had already referred to the mixture

of coherent and incoherent components in the early phases of the wavefield, the length scales controlling its attenuation remains under debate. To bring some arguments in this discussion, we measured the peak energy decay with distance. Our results showed that in the forward scattering regime, the attenuation of the peak energy is controlled by the transport mean free path. Despite our results were obtained only for certain type of random media that are very rich in small scales, they suggest that the basic relation $Q_{sc} = \omega\ell/v$ has little relevance for the apparent attenuation observed in real data.

6.1.1 Future work

It is worth mentioning that our analyses were performed by using synthetic data from the 2D numerical simulation of plane waves in random media. In order to reinforce the validity of our observations, further work with real data should be carried out. A first direction of this work concerns the implementation of the statistical analysis on a data set coming from local earthquake or active shots for frequencies up to 10 Hz in a highly scattering medium like volcanoes or very heterogeneous basins. Thus a study on the statistical fluctuations of the peak energy could be performed by assessing the dominance of log-normal and exponential distribution with distance. To do that, it would be necessary to use a dense array of seismic receivers in order to have a high spatial resolution to properly study the transition from log-normal to exponential distribution in distance. A second reason to use a dense array is the need to consider receivers with common distances to the source as several realizations of the random media (see the ergodicity hypothesis in chapter 3). Inter-station distances must be conveniently much shorter than the typical values of mean free paths observed in highly heterogeneous media ($\sim$ 1 km). For example, in highly faulted media, potentially good configurations of dense arrays can be found in Roux et al. (2016), Mordret et al. (2018), Mellors et al. (2018), Gradon et al. (2019), Touma et al. (2022), etc. Mordret et al. (2018) estimated surface wave velocities of the order of 300 m/s in the San Jacinto Fault Zone (SJFZ) from a dense array composed by 650 geophones and interstation distances of the order of 20 m. In the context of sedimentary basins Mellors et al. (2018) used a dense array of 996 geophones with interstation distances between 25 and 100m at frequencies up to 20 Hz, in order to understand the generation of S waves (500m/s) from explosions. It is worth mentioning that in the case of a statistical study of the peak energy fluctuations by using active sources and dense arrays, only propagation distances much larger than the wavelengths of interest would be used. However the huge density of receiver would be profitted in order to have large number of common propagation distances that can be treated as random media realizations.

The objective of this work would be to test the possibility to constrain the scattering mean free path from the critical distance at which the crossover from log-normal to exponential distribution occurs. To validate those potential measurements it would be necessary to compare them with existing approaches based on RTT. This would require the use of an anisotropic scattering assumption in the RTT model, in order to retrieve both, the transport (ℓ^*) and the scattering (ℓ) mean free paths. A possible advantage of estimating ℓ based on the statistical analyses is that it does not require of a strong hypothesis on the propagation regime or wave mode (surface or body). Furthermore, in the context of seismic hazard, performing this type of statistical analyses would help to establish a direct link between the scattering properties of a medium and the level of epistemic uncertainty.

6.2 Attenuation measurements at the Piton de la Fournaise Volcano using seismic noise correlations

The second part of our work consisted in the separation of scattering and absorption mechanisms at a local scale. Previous works had shown the possibility to measure attenuation properties by using earthquake data and active shots. However, attenuation measurements based on the earthquake coda would be limited to regions with high seismicity and dependent to a good characterization of the earthquake source. Furthermore, the sensitivity of the earthquake coda is distributed over areas that exceed the local interest. In order to perform attenuation measurements which are sensitive to more localized structures, we proposed a technique to separate scattering and absorption mechanisms from seismic noise correlation.

It is worth mentioning that the cross-correlation functions, by definition, have two sides which represent the causal and acausal parts of the reconstructed wavefield. These two sides are expected to describe the wave propagation in one direction and in the opposite to it. Under desired conditions such as the uniform distribution of noise sources and the energy equipartion, the causal and acausal parts must be identical. However, in most cases of reality noise sources might have a predominant direction, which can lead to systematic differences between the causal and acausal parts of CCFs. This represents a difficulty in this type of approach because the uneven distribution of noise sources can mask the propagation properties of the study area. Although the presence of such undesired conditions, appropriate pre-processing and post-processing artifacts might help to reduce these effects.

In order to measure attenuation properties from seismic noise correlation, we used 4 years of continuous noise records at 17 broadband stations at the Piton de la Fournaise Volcano. The resulting cross-correlation functions (CCF) were analysed in the $0.5 - 4$Hz frequency band. Attenuation properties were measured by comparing the energy envelopes of CCFs with those from the isotropic solution of the RTT for surface waves. In a first set of measurements we used the so-known multiple lapse time window analysis (MLTWA) to obtain global estimates attenuation properties. These global measurements were performed independently for both sides of the CCFs, the causal and acausal parts. As generally expected for volcanoes, results showed that scattering is the dominant attenuation mechanism in the study zone. Furthermore, some systematic differences between causal and acausal parts of the CCFs were observed, as well as a lower accuracy of scattering estimates with respect to absorption.

In order to better understand these discrepancies we proposed a technique in which measurements were performed by exploiting individually the full energy envelopes. This was based on the distance dependence of scattering and absorption signatures on the modelled energy envelopes. On the one hand, scattering effects become significant as the propagation distance increases. On the other hand, absorption is independent on the distance, but short propagation distances offer a longer coda so that, absorption measurements can be performed more robustly. Thus, attenuation properties were estimated in two stages. We first estimated absorption from short propagation distances, including auto-correlation functions (ACF). And secondly, once absorption was fixed, we estimated scattering at long propagation distances.

The absorption estimates at each station from ACFs, showed some correlation with existing geological and geophysical works in the study region. Such agreement was mainly observed at low frequency ([0.5-1]Hz). At higher frequency bands ([1-2] and [2-4]Hz) there is little correlation with geological structures. This is possibly due to the higher influence of body waves in the coda energy which are sensitive to deeper structures.

Long-distance estimates of scattering attenuation were performed by using the average energies contained in two short windows representing the ballistic and the early diffused waves. In a

first attempt, scattering was constrained by fitting average energies from each individual RTT envelope to those from CCFs. The azimuthal distribution of the retrieved transport mean free paths evidence a significant bias of scattering measurements towards the dominant direction of the noise sources. This behavior also explained the discrepancy between causal and acausal observed in the MLTWA measurements. To reduce this effect we proposed a new fitting procedure which is based on the ratio between the 'ballistic' and early diffused fields (ball-diff). Results from the grid search showed a higher accuracy and a lower azimuthal dependence of scattering attenuation. Additionally, we showed that the ball-diff ratio technique has the potential to lead to lateral variations of scattering, since measurements can be performed for each individual energy envelope.

Our full-envelope based approach was then validated by comparing the noise-based measurements with those from small-magnitude earthquakes at $[1-2]$ and $[2-4]$Hz bands. At the lowest frequency band, we were not able to perform these comparisons due to the low signal-to-noise ratio of the earthquake records. This represents an advantage of our noise-based approach since it allows to measure attenuation properties at a local scale in a frequency range inaccessible for small local earthquakes. The good agreement in terms of absorption estimates between noise and earthquake approaches also evidenced the applicability of ACFs to constrain intrinsic attenuation. Thus, we showed that it is possible to use one single station to obtain localized measurements.

6.2.1 Future work

Monitoring attenuation properties

Note that the measurements that we performed correspond to CCFs of seismic noise stacked over four years. However, tracking the time evolution of attenuation properties could give interesting insights on the time variations of small-scale structures at the volcano. The so-known velocity changes (dv/v) have already been used to understand the dynamics of the PDF volcano. Diverse works have made use either of 'ballistic' (e.g. Takano et al. (2019)) or coda waves (e.g. Sens-Schönfelder et al. (2014)).

A first direction concerning the attenuation properties at Piton de la Fournaise volcano would be their estimation at different time periods with monitoring purposes. This can be done by using CCFs stacked each month and tracking the evolution of scattering and absorption mechanisms within the whole period of four years, in the [0.5-4]Hz band. A first implication would be the understanding of possible seasonal effects associated to temperature changes in the surface. Secondly, since absorption and scattering are generally controlled by the presence of fluids and small-scale structures, monitoring these properties would help to better understand the dynamics of the volcano. It should be noted that exploiting CCFs stacked over one month, might lead to less stable estimates of attenuation properties. This is due to potentially poor SNR at such short periods of time.

Similarly, this potential monitoring technique could be extended to different geological environments. In the recent years the ground water level have been monitored by detecting velocity changes from CCFs (e.g. Lecocq et al. (2017) Voisin et al. (2017); Garambois et al. (2019)). For example, Voisin et al. (2017) found good correlation between the estimated dv/v from CCFs and piezometric data at the Crépieux-Charmy (France) groundwater exploitation field. Even though, the velocity changes have shown to be a relevant indicator on the water level variations, it is also known that seismic wave velocities are affected by diverse physical parameter (e.g. stiffness, density, medium heterogeneity, porosity). This could possibly complicate the geological interpretation on the wave velocity changes. Alternatively, monitoring attenuation properties might lead to more constrained geological implications. Particularly, absorption is

expected to be directly controlled by the presence of fluids and temperature. Thus, another direction of our work would be the estimation of absorption from auto-correlation functions of seismic noise in the same area presented in Voisin et al. (2017) and Garambois et al. (2019). For this end, estimations of absorption could be carried out by using either the radiative transfer theory or the diffusion approximation. Frequency bands would be conveniently selected in the same range as Garambois et al. (2019) (3 - 40 Hz) in order to test some degree of correlation between the potential attenuation measurements and the existing results of velocity variations.

Estimating attenuation properties at sedimentary basins

A further development of this work would concern the application of our technique in sedimentary basins. Characterizing attenuation mechanisms in a basin environment would be relevant first, to better predict the earthquake ground motion in urban contexts, and secondly to better characterize the geotechnical properties of the site. Some previous works (Nakata and Beroza (2015); Nakata et al. (2015)) on the study of small-scale heterogeneities in sedimentary basins were carried out by measuring the travel times of reconstructed direct waves from CCFs of seismic noise. For example Nakata and Beroza (2015) used a large and dense array to measure spatial variations P wave velocities at Long Beach (California). In a later publication, Nakata et al. (2015) developed a von Kármán model for the description of the small-scale heterogeneities constrained in Nakata and Beroza (2015). Even though their results can be helpful for the prediction of high frequency ground motion, this type of technique is limited to very dense receiver networks whose inter-station distances must be smaller than the correlation lengths ($\Delta x << a$). For cases with much shorter correlation lengths (of the order of meters) a travel time-based technique would be impractical. For example, in the case of Grenoble valley, borehole measurements have exhibited vertical and horizontal correlation lengths of about 2m and 20m, with corresponding velocity fluctuations of the order of 30% (see Chaljub et al. (2021)). The short correlation lengths in the vertical direction, and the typical values of shear wave velocity (200 m/s), might indicate a relatively wide range of frequencies in which isotropic scattering would be dominant (Rayleigh regime $ka<1$). To put this idea in context, in Fig. 6.1 we show a theoretical calculation of the scattering attenuation for a 2D von kármán medium with some of the statistical properties found in the Grenoble valley (from borehole measurements), presented in Chaljub et al. (2021). We illustrate the frequency range at which isotropic scattering is expected to be dominant (]0.1 - 6]Hz), and therefore suggesting the validity of the RTT model (isotropic assumption) for the separation of scattering and absorption mechanisms in the Grenoble valley.

It is worth mentioning that previous to the application of such simplified RTT model, an observational work is strongly recommended to identify some major signatures in the energy envelopes of reconstructed surface waves from CCFs. This would allow to empirically select a range of propagation distances and frequencies at which it is possible to measure the attenuation properties.

The use of a more realistic RTT model

A different direction of our work concerns the use of a more realistic RTT model to constrain attenuation properties from seismic ambient noise at a local scale. Our estimations at PDF volcano were performed under the assumption of isotropic scattering and with the dominance surface waves. Indeed, besides the difficulties to reconstruct high quality CCFs above 4 Hz, at such frequencies the RTT model for surface waves might be less valid due to the increasing influence of body waves. Furthermore, higher frequency waves could be dominated by the forward

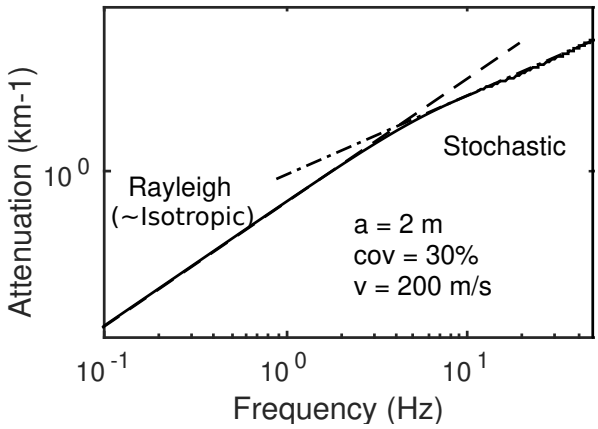

Figure 6.1: Example of calculation of scattering attenuation for a 2D von Kármán medium with statistical properties corresponding to those estimated for the Grenoble valley from borehole measurements ($v = 200$m/s, cov$= 30\%$, $a = 2$m). For this example the hurst exponent is selected to be the corresponding to an exponential ACF (0.5) and the density and velocity are assumed to have the same level of perturbation ($\nu = 1$). The dashed and dash-dotted lines correspond represent the Rayleigh and the stochastic regimes, and the solid line is the exact solution of the Dyson's equation.

scattering regime as the wavelengths become shorter than the characteristic size of the diffractors. These scenarios might indicate the need to use an RTT model that includes the coupling of surface and body waves, and the non-isotropic scattering. This would allow to retrieve both length scales, the transport and the scattering mean free paths, as well as to reproduce more complex behaviors occurring at the early phases of the wavefield.

Bibliography

Aki, K. (1969). Analysis of the seismic coda of local earthquakes as scattered waves. *Journal of Geophysical Research*, 74(2):615–631.

Aki, K. (1980). Attenuation of shear-waves in the lithosphere for frequencies from 0.05 to 25 hz. *Physics of the Earth and Planetary Interiors*, 21(1):50–60.

Aki, K. and Chouet, B. (1975). Origin of coda waves: Source, attenuation, and scattering effects. *Journal of Geophysical Research*, 80(23):3322–3342.

Aki, K., Christoffersson, A., and Husebye, E. S. (1976). Three-dimensional seismic structure of the lithosphere under montana lasa. *Bulletin of the Seismological Society of America*, 66(2):501–524.

Aki, K., Christoffersson, A., and Husebye, E. S. (1977). Determination of the three-dimensional seismic structure of the lithosphere. *Journal of Geophysical Research*, 82(2):277–296.

Anderson, J. G., Bodin, P., Brune, J. N., Prince, J., Singh, S. K., Quaas, R., and Onate, M. (1986). Strong ground motion from the michoacan, mexico, earthquake. *Science*, 233(4768):1043–1049.

Anderson, J. G. and Hough, S. E. (1984). A model for the shape of the fourier amplitude spectrum of acceleration at high frequencies. *Bulletin of the Seismological Society of America*, 74(5):1969–1993.

Bard, P.-Y. and Bouchon, M. (1985). The two-dimensional resonance of sediment-filled valleys. *Bulletin of the Seismological Society of America*, 75(2):519–541.

Birch, F. (1960). The velocity of compressional waves in rocks to 10 kilobars: 1. *Journal of Geophysical Research*, 65(4):1083–1102.

Birch, F. (1961). The velocity of compressional waves in rocks to 10 kilobars: 2. *Journal of Geophysical Research*, 66(7):2199–2224.

Bonilla, L. F., Archuleta, R. J., and Lavallee, D. (2005). Hysteretic and dilatant behavior of cohesionless soils and their effects on nonlinear site response: Field data observations and modeling. *Bulletin of the Seismological Society of America*, 95(6):2373–2395.

Boore, D. M. (1986). Short-period p-and s-wave radiation from large earthquakes: implications for spectral scaling relations. *Bulletin of the Seismological Society of America*, 76(1):43–64.

Boore, D. M. (2003). Simulation of ground motion using the stochastic method. *Pure and applied geophysics*, 160:635–676.

Brenguier, F., Kowalski, P., Ackerley, N., Nakata, N., Boué, P., Campillo, M., Larose, E., Rambaud, S., Pequegnat, C., Lecocq, T., Roux, P., Ferrazzini, V., Villeneuve, N., Shapiro, N. M., and Chaput, J. (2015). Toward 4d noise-based seismic probing of volcanoes: Perspectives from a large-n experiment on piton de la fournaise volcano. *Seismological Research Letters*, 87(1):15–25.

Brenguier, F., Shapiro, N. M., Campillo, M., Ferrazzini, V., Duputel, Z., Coutant, O., and Nercessian, A. (2008). Towards forecasting volcanic eruptions using seismic noise. *Nature Geoscience*, 1(2):126–130.

Cabas, A., Rodriguez-Marek, A., and Bonilla, L. F. (2017). Estimation of site-specific kappa (κ_0)-consistent damping values at kik-net sites to assess the discrepancy between laboratory-based damping models and observed attenuation (of seismic waves) in the field. *Bulletin of the Seismological Society of America*, 107(5):2258–2271.

Calvet, M. and Margerin, L. (2013). Lapse-time dependence of coda q: Anisotropic multiple-scattering models and application to the pyrenees. *Bulletin of the Seismological Society of America*, 103(3):1993–2010.

Calvet, M., Margerin, L., and Hung, S.-H. (2023). Anomalous attenuation of high-frequency seismic waves in taiwan: Observation, model and interpretation. *Journal of Geophysical Research: Solid Earth*, 128(3).

Campillo, M. and Paul, A. (2003). Long-range correlations in the diffuse seismic coda. *Science*, 299(5606):547–549.

Carcole, E. and Sato, H. (2010). Spatial distribution of scattering loss and intrinsic absorption of short-period waves in the lithosphere of japan on the basis of the multiple lapse time window analysis of hi-net data. *Geophysical Journal International*, 180(1):268–290.

Celorio, M., Chaljub, E., Margerin, L., and Stehly, L. (2022). Propagation of 2-d SH waves in random media: Insights from ab initio numerical simulations and transport theory. *Frontiers in Earth Science*, 10.

Cerveny, V. (1987). Ray tracing algorithms in three-dimensional laterally varying layered structures. *Seismic tomography*, 5:99–133.

Chaljub, E., Celorio, M., Cornou, C., De Martin, F., El Haber, E., Margerin, L., Marti, J., and Zentner, I. (2021). Numerical simulation of wave propagation in heterogeneous and random media for site effects assessment in the grenoble valley.

Chaljub, E., Komatitsch, D., Vilotte, J.-P., Capdeville, Y., Valette, B., and Festa, G. (2007). Spectral-element analysis in seismology. In *Advances in Wave Propagation in Heterogenous Earth*, pages 365–419. Elsevier.

Chaljub, E., Moczo, P., Tsuno, S., Bard, P.-Y., Kristek, J., Kaser, M., Stupazzini, M., and Kristekova, M. (2010). Quantitative comparison of four numerical predictions of 3d ground motion in the grenoble valley, france. *Bulletin of the Seismological Society of America*, 100(4):1427–1455.

Chandrasekhar, S. (1960). *Radiative Transfer*. Courier Corporation.

Clarke, D., Brenguier, F., Froger, J.-L., Shapiro, N. M., Peltier, A., and Staudacher, T. (2013). Timing of a large volcanic flank movement at piton de la fournaise volcano using noise-based seismic monitoring and ground deformation measurements. *Geophysical Journal International*, 195(2):1132–1140.

Cornou, C., Bard, P.-Y., and Dietrich, M. (2003). Contribution of dense array analysis to the identification and quantification of basin-edge-induced waves, part ii: Application to grenoble basin (french alps). *Bulletin of the Seismological Society of America*, 93(6):2624–2648.

Cruz-Atienza, V. M., Tago, J., Sanabria-Gómez, J. D., Chaljub, E., Etienne, V., Virieux, J., and Quintanar, L. (2016). Long duration of ground motion in the paradigmatic valley of mexico. *Scientific Reports*, 6(1).

Dainty, A. M., Toksöz, M. N., Anderson, K. R., Pines, P. J., Nakamura, Y., and Latham, G. (1974). Seismic scattering and shallow structure of the moon in oceanus procellarum. *The Moon*, 9(1):11–29.

de Hoop, M. V., Garnier, J., and Sølna, K. (2022). System of radiative transfer equations for coupled surface and body waves. *Zeitschrift für angewandte Mathematik und Physik*, 73(5):1–31.

De Rosny, J. and Roux, P. (2001). Multiple scattering in a reflecting cavity: Application to fish counting in a tank. *The Journal of the Acoustical Society of America*, 109(6):2587–2597.

Del Pezzo, E. (2008). Seismic wave scattering in volcanoes. *Advances in geophysics*, 50:353–371.

Denolle, M., Dunham, E., Prieto, G., and Beroza, G. (2014). Strong ground motion prediction using virtual earthquakes. *Science*, 343(6169):399–403.

Dolan, S. S., Bean, C. J., and Riollet, B. (1998). The broad-band fractal nature of heterogeneity in the upper crust from petrophysical logs. *Geophysical Journal International*, 132(3):489–507.

Duputel, Z., Ferrazzini, V., Brenguier, F., Shapiro, N., Campillo, M., and Nercessian, A. (2009). Real time monitoring of relative velocity changes using ambient seismic noise at the piton de la fournaise volcano (la réunion) from january 2006 to june 2007. *Journal of Volcanology and Geothermal Research*, 184(1-2):164–173.

Duputel, Z., Ferrazzini, V., Lengliné, O., Michon, L., Fontaine, F. R., and Massin, F. (2022). Seismicity of la réunion island. *Comptes Rendus. Géoscience*, 353(S1):237–255.

Elgamal, A., Lai, T., Yang, Z., and He, L. (2001). Dynamic soil properties, seismic downhole arrays and applications in practice.

Emoto, K. and Sato, H. (2018). Statistical characteristics of scattered waves in three-dimensional random media: comparison of the finite difference simulation and statistical methods. *Geophysical Journal International*, 215(1):585–599.

Eulenfeld, T. and Wegler, U. (2016). Measurement of intrinsic and scattering attenuation of shear waves in two sedimentary basins and comparison to crystalline sites in germany. *Geophysical Journal International*, 205(2):744–757.

Eulenfeld, T. and Wegler, U. (2017). Crustal intrinsic and scattering attenuation of high-frequency shear waves in the contiguous united states. *Journal of Geophysical Research: Solid Earth*, 122(6):4676–4690.

Fehler, M. (1991). Numerical basis of the separation of scattering and intrinsic absorption from full seismogram envelope. a monte-carlo simulation of multiple isotropic scattering. *Papers in meteorology and Geophysics*, 42(2):65–91.

Fehler, M., Hoshiba, M., Sato, H., and Obara, K. (1992). Separation of scattering and intrinsic attenuation for the Kanto-Tokai region, Japan, using measurements of S-wave energy versus hypocentral distance. *Geophysical Journal International*, 108(3):787–800.

Fei, T., Fehler, M. C., and Hildebrand, S. T. (1995). Finite-difference solutions of the 3-d eikonal equation. In *SEG Technical Program Expanded Abstracts 1995*, pages 1129–1132. Society of Exploration Geophysicists.

Frankel, A. and Clayton, R. W. (1986). Finite difference simulations of seismic scattering: Implications for the propagation of short-period seismic waves in the crust and models of crustal heterogeneity. *Journal of Geophysical Research*, 91(B6):6465.

Frisch, U. (1968). *Probabilistic Methods in Applied Mathematics*, chapter Wave propagation in random media, pages 75–198. Academic Press, New-York.

Gaebler, P. J., Eulenfeld, T., and Wegler, U. (2015). Seismic scattering and absorption parameters in the W-Bohemia/Vogtland region from elastic and acoustic radiative transfer theory. *Geophysical Supplements to the Monthly Notices of the Royal Astronomical Society*, 203(3):1471–1481.

Garambois, S., Voisin, C., Guzman, M. A. R., Brito, D., Guillier, B., and Réfloch, A. (2019). Analysis of ballistic waves in seismic noise monitoring of water table variations in a water field site: added value from numerical modelling to data understanding. *Geophysical Journal International*, 219(3):1636–1647.

Gélis, C. and Bonilla, L. F. (2012). 2-dp–sv numerical study of soil–source interaction in a non-linear basin. *Geophysical Journal International*, 191(3):1374–1390.

Gillet, K., Margerin, L., Calvet, M., and Monnereau, M. (2017). Scattering attenuation profile of the moon: Implications for shallow moonquakes and the structure of the megaregolith. *Physics of the Earth and Planetary Interiors*, 262:28–40.

Goodman, J. W. (2015). *Statistical optics*. John Wiley & Sons.

Gouédard, P., Stehly, L., Brenguier, F., Campillo, M., de Verdière, Y. C., Larose, E., Margerin, L., Roux, P., Sánchez-Sesma, F. J., Shapiro, N. M., and Weaver, R. L. (2008). Cross-correlation of random fields: mathematical approach and applications. *Geophysical Prospecting*, 56(3):375–393.

Gradon, C., Moreau, L., Roux, P., and Ben-Zion, Y. (2019). Analysis of surface and seismic sources in dense array data with match field processing and markov chain monte carlo sampling. *Geophysical Journal International*, 218(2):1044–1056.

Graves, R. W. and Pitarka, A. (2010). Broadband ground-motion simulation using a hybrid approach. *Bulletin of the Seismological Society of America*, 100(5A):2095–2123.

Gusev, A. and Abubakirov, I. (1987). Monte-carlo simulation of record envelope of a near earthquake. *Physics of the Earth and Planetary Interiors*, 49(1-2):30–36.

Gusev, A. and Abubakirov, I. (1999). Vertical profile of effective turbidity reconstructed from broadening of incoherent body-wave pulses—i. general approach and the inversion procedure. *Geophysical Journal International*, 136(2):295–308.

Haendel, A., Ohrnberger, M., and Krüger, F. (2016). Extracting near-surface q_L between 1-4 hz from higher-order noise correlations in the euroseistest area, greece. *Geophysical Journal International*, 207(2):655–666.

Hartzell, S., Harmsen, S., and Frankel, A. (2010). Effects of 3D random correlated velocity perturbations on predicted ground motions. *Bulletin of the Seismological Society of America*, 100(4):1415–1426.

Heller, G., Margerin, L., Sèbe, O., Mayor, J., and Calvet, M. (2022). Revisiting multiple-scattering principles in a crustal waveguide: Equipartition, depolarization and coda normalization. *Pure and Applied Geophysics*, 179(6-7):2031–2065.

Hennino, R., Trégourès, N., Shapiro, N. M., Margerin, L., Campillo, M., van Tiggelen, B. A., and Weaver, R. L. (2001). Observation of equipartition of seismic waves. *Physical Review Letters*, 86(15):3447–3450.

Hirose, T., Nakahara, H., and Nishimura, T. (2019). A passive estimation method of scattering and intrinsic absorption parameters from envelopes of seismic ambient noise cross-correlation functions. *Geophysical Research Letters*, 46(7):3634–3642.

Hirose, T., Nakahara, H., Nishimura, T., and Campillo, M. (2020). Locating spatial changes of seismic scattering property by sparse modeling of seismic ambient noise cross-correlation functions: Application to the 2008 iwate-miyagi nairiku (m_w 6.9), japan, earthquake. *Journal of Geophysical Research: Solid Earth*, 125(6).

Hirose, T., Ueda, H., and Fujita, E. (2022). Scattering and intrinsic absorption parameters of rayleigh waves at 18 active volcanoes in japan inferred using seismic interferometry. *Bulletin of Volcanology*, 84(3).

Hoshiba, M. (1991). Simulation of multiple-scattered coda wave excitation based on the energy conservation law. *Physics of the Earth and Planetary Interiors*, 67(1-2):123–136.

Hoshiba, M. (1993). Separation of scattering attenuation and intrinsic absorption in japan using the multiple lapse time window analysis of full seismogram envelope. *Journal of Geophysical Research: Solid Earth*, 98(B9):15809–15824.

Hoshiba, M. (2000). Large fluctuation of wave amplitude produced by small fluctuation of velocity structure. *Physics of the earth and planetary interiors*, 120(3):201–217.

Hu, Z., Olsen, K. B., and Day, S. M. (2022). 0–5 Hz deterministic 3-D ground motion simulations for the 2014 La Habra, California, Earthquake. *Geophysical Journal International*, 230(3):2162–2182.

Hudson, J. A. (1990). Attenuation due to second-order scattering in material containing cracks. *Geophysical Journal International*, 102(2):485–490.

Imperatori, W. and Mai, P. M. (2012). Broad-band near-field ground motion simulations in 3-dimensional scattering media. *Geophysical Journal International*, 192(2):725–744.

Imperatori, W. and Mai, P. M. (2015). The role of topography and lateral velocity heterogeneities on near-source scattering and ground-motion variability. *Geophysical Journal International*, 202(3):2163–2181.

Karakostas, F., Schmerr, N., Maguire, R., Huang, Q., Kim, D., Lekic, V., Margerin, L., Nunn, C., Menina, S., Kawamura, T., et al. (2021). Scattering attenuation of the martian interior through coda-wave analysis. *Bulletin of the Seismological Society of America*, 111(6):3035–3054.

Klimeš, L. (2002). Correlation functions of random media. *Pure and applied geophysics*, 159:1811–1831.

Knopoff, L. (1964). Q. *Reviews of Geophysics*, 2(4):625.

Komatitsch, D. and Vilotte, J.-P. (1998). The spectral element method: An efficient tool to simulate the seismic response of 2D and 3D geological structures. *Bulletin of the Seismological Society of America*, 88:368–392.

Kourganoff, V. (1969). *Introduction to the general theory of particle transfer*. CRC Press.

Ktenidou, O.-J., Abrahamson, N. A., Drouet, S., and Cotton, F. (2015). Understanding the physics of kappa (κ): insights from a downhole array. *Geophysical Journal International*, 203(1):678–691.

Ktenidou, O.-J., Cotton, F., Abrahamson, N. A., and Anderson, J. G. (2014). Taxonomy of κ: A review of definitions and estimation approaches targeted to applications. *Seismological Research Letters*, 85(1):135–146.

Larose, E., Derode, A., Campillo, M., and Fink, M. (2004). Imaging from one-bit correlations of wideband diffuse wave fields. *Journal of Applied Physics*, 95(12):8393–8399.

Larose, E., Roux, P., and Campillo, M. (2008). Reconstruction of rayleigh-lamb dispersion spectrum based on noise obtained from an air-jet forcing. *The Journal of the Acoustical Society of America*, 123(5_Supplement):3064–3064.

Lecocq, T., Longuevergne, L., Pedersen, H. A., Brenguier, F., and Stammler, K. (2017). Monitoring ground water storage at mesoscale using seismic noise: 30 years of continuous observation and thermo-elastic and hydrological modeling. *Scientific Reports*, 7(1).

Lénat, J.-F., Bachèlery, P., and Merle, O. (2012). Anatomy of piton de la fournaise volcano (la réunion, indian ocean). *Bulletin of Volcanology*, 74(9):1945–1961.

Liu, X., Ben-Zion, Y., and Zigone, D. (2015). Extracting seismic attenuation coefficients from cross-correlations of ambient noise at linear triplets of stations. *Geophysical Journal International*, 203(2):1149–1163.

Lobkis, O. I. and Weaver, R. L. (2001). On the emergence of the green's function in the correlations of a diffuse field. *The Journal of the Acoustical Society of America*, 110(6):3011–3017.

Magrini, F. and Boschi, L. (2021). Surface-wave attenuation from seismic ambient noise: Numerical validation and application. *Journal of Geophysical Research: Solid Earth*, 126(1).

Margerin, L. (2005). Introduction to radiative transfer of seismic waves. In *Seismic Earth: Array Analysis of Broadband Seismograms*, pages 229–252. American Geophysical Union.

Margerin, L. (2006). Attenuation, transport and diffusion of scalar waves in textured random media. *Tectonophysics*, 416(1-4):229–244.

Margerin, L., Bajaras, A., and Campillo, M. (2019). A scalar radiative transfer model including the coupling between surface and body waves. *Geophysical Journal International*, 219(2):1092–1108.

Margerin, L., Campillo, M., Shapiro, N. M., and van Tiggelen, B. (1999). Residence time of diffuse waves in the crust as a physical interpretation of coda q: application to seismograms recorded in mexico. *Geophysical Journal International*, 138(2):343–352.

Margerin, L., Campillo, M., and Tiggelen, B. (1998). Radiative transfer and diffusion of waves in a layered medium: new insight into coda Q. *Geophysical Journal International*, 134(2):596–612.

Margerin, L., Menina, S., Compaire, N., Celorio, M., Barajas, A., Delsuc, A., Marti, J., Garcia, R., Calvet, M., Chaljub, E., Campillo, M., Kawamura, T., and Lognonné, P. (2022). Transport models for seismic scattering.

Margerin, L. and Nolet, G. (2003). Multiple scattering of high-frequency seismic waves in the deep earth: PKP precursor analysis and inversion for mantle granularity. *Journal of Geophysical Research: Solid Earth*, 108(B11).

Mayor, J., Calvet, M., Margerin, L., Vanderhaeghe, O., and Traversa, P. (2016). Crustal structure of the alps as seen by attenuation tomography. *Earth and Planetary Science Letters*, 439:71–80.

Mayor, J., Margerin, L., and Calvet, M. (2014). Sensitivity of coda waves to spatial variations of absorption and scattering: radiative transfer theory and 2-d examples. *Geophysical Journal International*, 197(2):1117–1137.

Mellors, R. J., Pitarka, A., Matzel, E., Magana-Zook, S., Knapp, D., Walter, W. R., Chen, T., Snelson, C. M., and Abbott, R. E. (2018). The source physics experiments large n array. *Seismological Research Letters*, 89(5):1618–1628.

Mordret, A., Mikesell, T. D., Harig, C., Lipovsky, B. P., and Prieto, G. A. (2016). Monitoring southwest greenland's ice sheet melt with ambient seismic noise. *Science Advances*, 2(5).

Mordret, A., Rivet, D., Landès, M., and Shapiro, N. M. (2015). Three-dimensional shear velocity anisotropic model of piton de la fournaise volcano (la réunion island) from ambient seismic noise. *Journal of Geophysical Research: Solid Earth*, 120(1):406–427.

Mordret, A., Roux, P., Boué, P., and Ben-Zion, Y. (2018). Shallow three-dimensional structure of the san jacinto fault zone revealed from ambient noise imaging with a dense seismic array. *Geophysical Journal International*, 216(2):896–905.

Müller, T. and Shapiro, S. (2003). Amplitude fluctuations due to diffraction and refraction in anisotropic random media: implications for seismic scattering attenuation estimates. *Geophysical Journal International*, 155(1):139–148.

Nakahara, H. and Carcolé, E. (2010). Maximum-likelihood method for estimating coda Q and the Nakagami-m parameter. *Bulletin of the Seismological Society of America*, 100(6):3174–3182.

Nakata, N. and Beroza, G. C. (2015). Stochastic characterization of mesoscale seismic velocity heterogeneity in long beach, california. *Geophysical Journal International*, 203(3):2049–2054.

Nakata, N., Boué, P., Brenguier, F., Roux, P., Ferrazzini, V., and Campillo, M. (2016). Body and surface wave reconstruction from seismic noise correlations between arrays at piton de la fournaise volcano. *Geophysical Research Letters*, 43(3):1047–1054.

Nakata, N., Chang, J. P., Lawrence, J. F., and Boué, P. (2015). Body wave extraction and tomography at long beach, california, with ambient-noise interferometry. *Journal of Geophysical Research: Solid Earth*, 120(2):1159–1173.

Obermann, A., Planès, T., Larose, E., and Campillo, M. (2013). Imaging preeruptive and coeruptive structural and mechanical changes of a volcano with ambient seismic noise. *Journal of Geophysical Research: Solid Earth*, 118(12):6285–6294.

OVPF and IPGP (2008). Seismic, tiltmeter, extensometer, magnetic and weather permanent networks on piton de la fournaise volcano and la réunion.

Paasschens, J. C. J. (1997). Solution of the time-dependent boltzmann equation. *Physical Review E*, 56(1):1135–1141.

Parolai, S., Bindi, D., and Pilz, M. (2015). κ_0: The role of intrinsic and scattering attenuation. *Bulletin of the Seismological Society of America*, 105(2A):1049–1052.

Peltier, A., Bachèlery, P., and Staudacher, T. (2009). Magma transport and storage at piton de la fournaise (la réunion) between 1972 and 2007: A review of geophysical and geochemical data. *Journal of Volcanology and Geothermal Research*, 184(1-2):93–108.

Prieto, G. A. and Beroza, G. C. (2008). Earthquake ground motion prediction using the ambient seismic field. *Geophysical Research Letters*, 35(14).

Prieto, G. A., Lawrence, J. F., and Beroza, G. C. (2009). Anelastic earth structure from the coherency of the ambient seismic field. *Journal of Geophysical Research*, 114(B7).

Prôno, E., Battaglia, J., Monteiller, V., Got, J.-L., and Ferrazzini, V. (2009). P-wave velocity structure of piton de la fournaise volcano deduced from seismic data recorded between 1996 and 1999. *Journal of Volcanology and Geothermal Research*, 184(1-2):49–62.

Prudencio, J., Pezzo, E. D., Garcia-Yeguas, A., and Ibanez, J. M. (2013). Spatial distribution of intrinsic and scattering seismic attenuation in active volcanic islands - i: model and the case of tenerife island. *Geophysical Journal International*, 195(3):1942–1956.

Prudencio, J., Pezzo, E. D., Ibáñez, J. M., Giampiccolo, E., and Patané, D. (2015). Two-dimensional seismic attenuation images of stromboli island using active data. *Geophysical Research Letters*, 42(6):1717–1724.

Przybilla, J. and Korn, M. (2008). Monte Carlo simulation of radiative energy transfer in continuous elastic random media—three-component envelopes and numerical validation. *Geophysical Journal International*, 173(2):566–576.

Przybilla, J., Korn, M., and Wegler, U. (2006). Radiative transfer of elastic waves versus finite difference simulations in two-dimensional random media. *Journal of Geophysical Research*, 111(B4).

Ranjan, P. and Konstantinou, K. I. (2020). Mapping intrinsic and scattering attenuation in the southern aegean crust using wave envelope inversion and sensitivity kernels derived from perturbation theory. *Journal of Geophysical Research: Solid Earth*, 125(10).

Rivet, D., Brenguier, F., Clarke, D., Shapiro, N. M., and Peltier, A. (2014). Long-term dynamics of piton de la fournaise volcano from 13 years of seismic velocity change measurements and GPS observations. *Journal of Geophysical Research: Solid Earth*, 119(10):7654–7666.

Roux, P., Moreau, L., Lecointre, A., Hillers, G., Campillo, M., Ben-Zion, Y., Zigone, D., and Vernon, F. (2016). A methodological approach towards high-resolution surface wave imaging of the san jacinto fault zone using ambient-noise recordings at a spatially dense array. *Geophysical Journal International*, 206(2):980–992.

Roux, P., Sabra, K. G., Kuperman, W. A., and Roux, A. (2005). Ambient noise cross correlation in free space: Theoretical approach. *The Journal of the Acoustical Society of America*, 117(1):79–84.

Rytov, S. M., Kravcov, Y. A., and Tatarskij, V. I. (1989). *Wave propagation through random media*. Springer.

Ryzhik, L., Papanicolaou, G., and Keller, J. B. (1996). Transport equations for elastic and other waves in random media. *Wave motion*, 24(4):327–370.

Sánchez-Sesma, F. J. and Campillo, M. (2006). Retrieval of the green's function from cross correlation: the canonical elastic problem. *Bulletin of the Seismological Society of America*, 96(3):1182–1191.

Sánchez-Sesma, F. J., Pérez-Ruiz, J. A., Campillo, M., and Luzón, F. (2006). Elastodynamic 2d green function retrieval from cross-correlation: Canonical inclusion problem. *Geophysical Research Letters*, 33(13).

Sato, H. (1982). Amplitude attenuation of impulsive waves in random media based on travel time corrected mean wave formalism. *The Journal of the Acoustical Society of America*, 71(3):559–564.

Sato, H. (1984). Attenuation and envelope formation of three-component seismograms of small local earthquakes in randomly inhomogeneous lithosphere. *Journal of Geophysical Research: Solid Earth*, 89(B2):1221–1241.

Sato, H. (1989). Broadening of seismogram envelopes in the randomly inhomogeneous lithosphere based on the parabolic approximation: southeastern honshu, japan. *Journal of Geophysical Research*, 94(B12):17735.

Sato, H. (1993). Energy transportation in one- and two-dimensional scattering media: Analytic solutions of the multiple isotropic scattering model. *Geophysical Journal International*, 112(1):141–146.

Sato, H. (1994). Formulation of the multiple non-isotropic scattering process in 2-D space on the basis of energy-transport theory. *Geophysical Journal International*, 117(3):727–732.

Sato, H. (2019). Power spectra of random heterogeneities in the solid earth. *Solid Earth*, 10(1):275–292.

Sato, H., Fehler, M. C., and Maeda, T. (2012). *Seismic wave propagation and scattering in the heterogeneous earth*. Springer Science & Business Media.

Savran, W. and Olsen, K. (2019). Ground motion simulation and validation of the 2008 Chino Hills earthquake in scattering media. *Geophysical Journal International*, 219(3):1836–1850.

Scalise, M., Pitarka, A., Louie, J. N., and Smith, K. D. (2021). Effect of random 3D correlated velocity perturbations on numerical modeling of ground motion from the Source Physics Experiment. *Bulletin of the Seismological Society of America*, 111(1):139–156.

Sens-Schönfelder, C., Margerin, L., and Campillo, M. (2009). Laterally heterogeneous scattering explains lg blockage in the pyrenees. *Journal of Geophysical Research*, 114(B7).

Sens-Schönfelder, C., Pomponi, E., and Peltier, A. (2014). Dynamics of piton de la fournaise volcano observed by passive image interferometry with multiple references. *Journal of Volcanology and Geothermal Research*, 276:32–45.

Sens-Schönfelder, C. and Wegler, U. (2006a). Passive image interferometry and seasonal variations of seismic velocities at merapi volcano, indonesia. *Geophysical Research Letters*, 33(21).

Sens-Schönfelder, C. and Wegler, U. (2006b). Radiative transfer theory for estimation of the seismic moment. *Geophysical Journal International*, 167(3):1363–1372.

Shapiro, N. M. and Campillo, M. (2004). Emergence of broadband rayleigh waves from correlations of the ambient seismic noise. *Geophysical Research Letters*, 31(7):n/a–n/a.

Shapiro, N. M., Campillo, M., Stehly, L., and Ritzwoller, M. H. (2005). High-resolution surface-wave tomography from ambient seismic noise. *Science*, 307(5715):1615–1618.

Shapiro, S., Schwarz, R., and Gold, N. (1996). The effect of random isotropic inhomogeneities on the phase velocity of seismic waves. *Geophysical Journal International*, 127(3):783–794.

Shapiro, S. A. and Kneib, G. (1993). Seismic attenuation by scattering: Theory and numerical results. *Geophysical Journal International*, 114(2):373–391.

Shiomi, K., Sato, H., and Ohtake, M. (1997). Broad-band power-law spectra of well-log data in Japan. *Geophysical Journal International*, 130(1):57–64.

Soergel, D., Pedersen, H. A., Stehly, L., Margerin, L., and and, A. P. (2019). Coda-q in the 2.5–20 s period band from seismic noise: application to the greater alpine area. *Geophysical Journal International*, 220(1):202–217.

Stacey, R. (1988). Improved transparent boundary formulations for the elastic-wave equation. *Bulletin of the Seismological Society of America*, 78(6):2089–2097.

Stehly, L. and Boué, P. (2017). On the interpretation of the amplitude decay of noise correlations computed along a line of receivers. *Geophysical Journal International*, page ggx021.

Stehly, L., Campillo, M., Froment, B., and Weaver, R. L. (2008). Reconstructing green's function by correlation of the coda of the correlation of ambient seismic noise. *Journal of Geophysical Research*, 113(B11).

Stehly, L., Campillo, M., and Shapiro, N. M. (2006). A study of the seismic noise from its long-range correlation properties. *Journal of Geophysical Research*, 111(B10).

Takano, T., Brenguier, F., Campillo, M., Peltier, A., and Nishimura, T. (2019). Noise-based passive ballistic wave seismic monitoring on an active volcano. *Geophysical Journal International*, 220(1):501–507.

Takemura, S., Furumura, T., and Maeda, T. (2015). Scattering of high-frequency seismic waves caused by irregular surface topography and small-scale velocity inhomogeneity. *Geophysical Journal International*, 201(1):459–474.

Tchawe, F. N., Gelis, C., Bonilla, L. F., and Lopez-Caballero, F. (2021). Effects of 2-D random velocity perturbations on 2-D SH short-period ground motion simulations in the basin of Nice, France. *Geophysical Journal International*, 226(2):847–861.

Touma, R., Aubry, A., Ben-Zion, Y., and Campillo, M. (2022). Distribution of seismic scatterers in the san jacinto fault zone, southeast of anza, california, based on passive matrix imaging. *Earth and Planetary Science Letters*, 578:117304.

Tregoures, N. P. and Van Tiggelen, B. A. (2002). Quasi-two-dimensional transfer of elastic waves. *Physical Review E*, 66(3):036601.

Ugalde, A. (2002). Seismic coda attenuation after the $m_w = 6.2$ armenia (colombia) earthquake of 25 january 1999. *Journal of Geophysical Research*, 107(B6).

Ugalde, A., Carcolé, E., and Vargas, C. A. (2010). S-wave attenuation characteristics in the galeras volcanic complex (south western colombia). *Physics of the Earth and Planetary Interiors*, 181(3-4):73–81.

van Dinther, C., Margerin, L., and Campillo, M. (2020). Laterally varying scattering properties in the north anatolian fault zone from ambient noise cross-correlations. *Geophysical Journal International*, 225(1):589–607.

van Driel, M., Ceylan, S., Clinton, J. F., Giardini, D., Horleston, A., Margerin, L., Stähler, S. C., Böse, M., Charalambous, C., Kawamura, T., et al. (2021). High-frequency seismic events on Mars observed by InSight. *Journal of Geophysical Research: Planets*, 126(2):e2020JE006670.

van Laaten, M., Eulenfeld, T., and Wegler, U. (2021). Comparison of multiple lapse time window analysis and qopen to determine intrinsic and scattering attenuation. *Geophysical Journal International*, 228(2):913–926.

Voisin, C., Guzmán, M. A. R., Réfloch, A., Taruselli, M., and Garambois, S. (2017). Groundwater monitoring with passive seismic interferometry. *Journal of Water Resource and Protection*, 09(12):1414–1427.

Wapenaar, K. (2004). Retrieving the elastodynamic green's function of an arbitrary inhomogeneous medium by cross correlation. *Physical Review Letters*, 93(25):254301.

Weaver, R. L. (1990). Diffusivity of ultrasound in polycrystals. *Journal of the Mechanics and Physics of Solids*, 38(1):55–86.

Weaver, R. L. and Lobkis, O. I. (2001). Ultrasonics without a source: Thermal fluctuation correlations at mhz frequencies. *Physical Review Letters*, 87(13):134301.

Wegler, U. (2003). Analysis of multiple scattering at Vesuvius volcano, Italy, using data of the TomoVes active seismic experiment. *Journal of volcanology and geothermal research*, 128(1-3):45–63.

Wegler, U. (2004). Diffusion of seismic waves in a thick layer: Theory and application to vesuvius volcano. *Journal of Geophysical Research: Solid Earth*, 109(B7).

Wegler, U., Korn, M., and Przybilla, J. (2006). Modeling full seismogram envelopes using radiative transfer theory with born scattering coefficients. *Pure and Applied Geophysics*, 163(2-3):503–531.

Wegler, U. and Lühr, B. G. (2001). Scattering behaviour at merapi volcano (java) revealed from an active seismic experiment. *Geophysical Journal International*, 145(3):579–592.

Wu, R.-S. (1982). Mean field attenuation and amplitude attenuation due to wave scattering. *Wave motion*, 4(3):305–316.

Wu, R.-S. (1985). Multiple scattering and energy transfer of seismic waves – separation of scattering effect from intrinsic attenuation – i. theoretical modelling. *Geophysical Journal International*, 82(1):57–80.

Wu, R.-S. and Aki, K. (1988). Multiple scattering and energy transfer of seismic waves—separation of scattering effect from intrinsic attenuation ii. application of the theory to hindu kush region. *Scattering and Attenuations of Seismic Waves, Part I*, pages 49–80.

Xu, Z., Margerin, L., and Mikesell, T. D. (2022). Monte Carlo simulations of coupled body- and Rayleigh-wave multiple scattering in elastic media. *Geophysical Journal International*, 228(2):1213–1236.

Yang, L., Lobkis, O., and Rokhlin, S. (2011). Shape effect of elongated grains on ultrasonic attenuation in polycrystalline materials. *Ultrasonics*, 51(6):697–708.

Yee, E., Stewart, J. P., and Tokimatsu, K. (2013). Elastic and large-strain nonlinear seismic site response from analysis of vertical array recordings. *Journal of Geotechnical and Geoenvironmental Engineering*, 139(10):1789–1801.

Yoshimoto, K., Takemura, S., and Kobayashi, M. (2015). Application of scattering theory to p-wave amplitude fluctuations in the crust. *Earth, Planets and Space*, 67(1).

Zalachoris, G. and Rathje, E. M. (2015). Evaluation of one-dimensional site response techniques using borehole arrays. *Journal of Geotechnical and Geoenvironmental Engineering*, 141(12):04015053.

Zhang, Z. Q., Jones, I. P., Schriemer, H. P., Page, J. H., Weitz, D. A., and Sheng, P. (1999). Wave transport in random media: the ballistic to diffusive transition. *Physical Review E*, 60(4):4843–4850.